Characteristics of Shear-Driven Micro Flow between Stationary and Rotating Disks

（静止－回転円板間のせん断駆動マイクロ流れの特性）

A Dissertation

by

Ho-Joon Lee

Advisor : Prof. Koichi Nishino

Submitted to Graduate School of Engineering
of Yokohama National University
in partial fulfillment of the requirements for the degree of

DOCTOR OF PHILOSOPHY

DIVISION OF SYSTEMS INTEGRATION
GRADUATE SCHOOL OF ENGINEERING
YOKOHAMA NATIONAL UNIVERSITY

December 2011

ABSTRACT

Characteristics of Shear-Driven Micro Flow between Stationary and Rotating Disks

Ho-Joon Lee

Yokohama National University

Chair of Advisory Committee : Professor Koichi Nishino

Recently, quantitative flow visualization has become an important tool to investigate three-dimensional complex flow structures in microfluidic. The development of laser, computer and digital image processing techniques made it possible to extract velocity field information from visualized flow images of tracer particles. Particle image velocimetry (PIV) / particle tracking velocimetry (PTV) method has become one of the most useful flow diagnostic technologies in the modern history of fluid mechanics. The particle based velocimetry techniques measure the whole velocity field information in a plane by dividing that is placements Δx and Δy of tracer particles with the time interval Δt during which the particles were displaced. Since the flow velocity is inferred from the particle displacement, it is also important to select proper tracer particles that follow the flow motion accurately without changing the flow properties.

These methods have been accepted as a reliable and powerful velocity field measurement technique. The PIV method in a strict sense provides the representative velocity vector averaged over each interrogation window. As the PTV method can identify individual particles and track them from image to image, the PTV method has higher spatial resolution than the PIV method for low-particle-density flows such as micro-scale flows in microfluidics. We develop two/three dimensional micro-PIV/PTV that can be applied to micro-scale passage.

In chapter 1, the detailed understanding of the flow inside the micro-scale passage is very important for their optimum design and active/passive control of flow due to rapid development in MEMS technology. In order to observe the flow phenomena in micro-fluidics, a suitable experimental technique that can resolve the temporal and spatial resolutions of the given micro-scale flow is definitely needed so that two/three dimensional PIV techniques are introduced.

In chapter 2, since the first micro-PIV experiment was carried out by Santiago et al (1998), micro-PIV measurement technique has been developed rapidly. This chapter is to provide the theoretical and technical methods to understand a micro-PIV system and technical technique.

In chapter 3, the numerical simulation is carried out by using the commercial fluid analysis software STAR-CD. It solves the three-dimensional, incompressible, laminar Navier-Stokes equations by finite volume method. The SIMPLE method is chosen for the pressure-velocity coupling and the algebraic multi-grid solver is used for the velocity and pressure corrections. These results for flow field are shown by the purpose of comparing with two/three-velocity components of micro-PIV and stereoscopic micro-PTV.

In chapter 4, digital image filtering is introduced in order to improve measure accuracy of near-wall flow from the present micro-PIV technique. Frequency sampling method is used to design a simple, digital, high-pass filter.

In chapter 5, the micro rotating flow between a pair of rotating and stationary disks, whose separation is 500μm, was studied experimentally and numerically with an objective to clarify the characteristics of the basic flow found in rotation-shearing chemical reactors. The micro-PIV technique was used to measure two-component velocities in the liquid layer. The commercial CFD software was used to provide data to compare and validate the micro-PIV results. As for the overall velocity profiles in the liquid layer, the micro-PIV and the CFD results are in fair agreement; both are showing (1) the linear increase of tangential and radial velocities with radial position, and (2) the

presence of a secondary flow that consists of an outward flow near the rotating disk and an inward flow near the stationary disk. This secondary flow is strengthened with the rotational speed and is responsible for the deviation of tangential velocity component from its linear profile in the direction of the thickness.

Measurement of near-wall from the present micro-PIV technique is appreciably improved by the use of a simple, digital, high-pass filtering technique that is applied to the acquired particle images. It is shown that the cut-off frequency of 0.1~0.15 pixel^{-1} (or cut-off wavelength of 6.7~10.0 pixels) works well with this technique. This cutoff wavelength is two to three times larger than the typical diameters of the in-focus particle images that are acquired in this study. It is demonstrated that the micro-PIV measurement with the high-pass filtering technique can provide detailed information about the flow field in the thin liquid layer between the rotating and stationary disks.

In chapter 6, a stereoscopic micro-PTV technique was shown using a single camera with a stereo optical attachment. The attachment developed here was shown to have a higher capability of fine optical adjustment than the previous one proposed by the authors. This stereoscopic micro-PTV technique was validated through a three-dimensional measurement of a rotating flow in a thin liquid layer between a rotating disk and a stationary disk. This rotating liquid layer is 10mm in diameter and the gap between the disks is 500μm. The rotational speed examined is 500rpm. It is shown that the effective depth-of-field of the present technique is 300μm for the imaging optics using a 5× objective (NA=0.14). The measured velocities compare reasonably well with the previous results obtained with a conventional 2D-2C PIV technique.

In chapter 7, in these rotating systems, the problem of friction torque by shear stress, power loss, and of heat transfer is strongly related to inside flowing induced by the rotating disk such as the circulation and secondary flows. These induced flows depend on the geometries of the stationary and rotating disks, for example, gap between stationary and rotating disk as well as radius and angle of rotation disk and so on. The approximate analytical equation was inferred as the function of z/H, r/R, and ω.

ACKNOWLEDGMENTS

I would like to express my deepest gratitude to my supervisor Prof. Koichi Nishino for being guided and mentored in the Ph.D. degree program. He has always open-mind with a smile on his face for discussions and is helpful to find the right way. Although he always does not give the accurate answers, he lets me find them by myself. I will never be able to forget what I have been learned from him while completing my Ph.D. degree program at Mechanical Engineering in Yokohama National University.

I also would like to thank for advisory committee members, Prof. Y. Utaka, Prof. J. Matsui, Prof. K. Ishii and Prof. S. Sakai. They suggested numerous improvements to be able to achieve the incorporate in the final manuscript.

I would like to share appreciation with the members of Nishino's laboratory - in particular H. Toma, A. Ishida, T. Matsunaga, R. Egashira, M. Yonezawa in the members of the present micro team and T. Kwai, K. Shinya, S. Takada in the members of the previous micro team, and H.D Song. I would like to give special thanks to CEO Baek at Taibaek precision Co, Dr. Lee at Hyundai Rotem, and Mr. Choi at Flowtech Research Inc who help my future bright. Also, I would like to give my thanks to the secretarial staff at the Nishino's Lab – Mrs. Abe and Mr. Terao.

Finally, I would like to share my pleasure with my parents living in Korea, for their support and encouragement with endless love. I owe my deepest gratitude to my wife, Mi-Hyun and to my two children, Seung-Gun and Yeo-Eun, who now stay in Korea. Without their dedicated support, I could never have finished this work. I dedicate this to them and to everybody who helped me.

Yokohama, December 2011

Ho-Joon Lee

[Prof. Koichi Nishino]

[Ho-Joon Lee]

TABLE OF CONTENTS

Page

LIST OF FIGURES

Page

LIST OF TABLES

Page

Chapter 1. Introduction

1.1 Rotating-disk system

Rotating-disk systems have been widely seen in industrial applications such as gas turbine, aircraft engines, hard-disk drives, automobile breaks systems, rotational air cleaners, extractors, atomizers, evaporators, microclimate systems, micro reactor etc.

They have various shapes that are designed to achieve each purpose. For example,

(1) Rotating disk in an infinite resting fluid or fluid rotating with another angular velocity (Fig. 1-1(a)),

(2) Rotating disk for impinging jet-cooling (Fig. 1-1(b)),

(3) Co-rotating or contra-rotating parallel disks with and without forced radial through flow in a gap between them (Fig. 1-1(c)),

(4) Stationary and rotating disks to generate a strongly-sheared flow between them (Fig. 1-1(d)),

(5) Two disks and two cylindrical surfaces for the closed non-ventilated cavities of gas turbines (Fig. 1-1(e)),

(6) Rotating disk shroud for air cooling system with inlet flow pre-swirl (Fig. 1-1(f)) ,and

(7) Rotating disk for the formation of thin liquid film.

As shown in Fig.1-1, rotating disk flows illustrate constant/varying angular rotation velocities which induce complicated flows with additional influencing factors. Based on these previous studies, a series of problems should be considered to encompass fluid

flow such as heat and mass transfer over disks rotating in a resting, rotating or radially accelerating fluid; unsteady conjugate heat transfer of a rotating disk (Fig. 1-1(a)); disk cooling by means of an impinging jet (Fig. 1-1(b)); forced radial flow in the cavities between co-rotating parallel disks (Fig. 1-1(c)); air cooling systems with inlet flow pre-swirl (Fig. 1-1(f), left).

1.1.1 Acting forces

Two types of forces act on fluid in rotating disk system: mass forces (or body forces) and surface forces. Mass forces acting on each fluid include the gravity, inertia forces, electrostatic forces, magnetic or electrical fields, etc.

Surface forces acting on elementary parts of a surface include pressure, internal friction (viscosity), forces acting on a surface from the side of flow, and forces of reaction from the body onto the flow. Mass forces are caused by force fields, such as gravitational, inertial and electromagnetic fields. The gravitational force is the result of the global gravity of the Earth. Inertial forces emerge at accelerating or decelerating translation motion of a system, in which fluid flow takes place. Inertial force can also be the result of rotation of a system as a whole or of a fluid only. Electromagnetic fields emerging in flow of an electrically conducting fluid in a magnetic field are not considered in the present study.

In rotating systems, inertial forces are external with respect to fluid flow, and their strength is determined by conditions of motion both of the system and of fluid flow itself. When inertial forces emerge as a result of streamline curvature in fluid flow in a stationary geometry (curvilinear or swirl flows), their value and direction depend on the velocity distribution in the flow and are ultimately determined by pressure and viscous forces. Gravitational and inertial mass forces can be expressed by the following relation

$$\vec{F} = \rho\vec{g}\,, \tag{1.1}$$

where $\vec{g}$ is the acceleration that determines a mass force. Mass forces are considered per unit volume.

Centrifugal forces are directed outwards from a rotation axis and orthogonal to it. They

can be caused by streamline curvature and expressed by the following relation:

$$\vec{F}_c = \rho\vec{\omega}\times(\vec{\omega}\times\vec{r}) = -\rho\vec{\omega}\cdot(\vec{r}\cdot\vec{\omega}) + \rho\vec{r}(\vec{\omega}\cdot\vec{\omega}) \tag{1.2}$$

The parameter $\vec{r}$ included in $\vec{F}_c$ is the position vector of a fluid particle relative to the rotation axis. The inner product $\vec{r}\cdot\vec{\omega}$ is equal to zero because $\vec{r}$ and $\vec{\omega}$ are orthogonal to each other. In curvilinear flow, where the system rotation is absent, a conventional local velocity of rotation at each specific point can be defined as $\vec{\omega} = \vec{V}/\vec{r}$, which results in the relation

$$\vec{F}_c = \rho R(\vec{V}/\vec{r})^2 = \rho\vec{V}^2/\vec{r} \tag{1.3}$$

where $\vec{V}$ is fluid flow velocity relative to the system (i.e. relative velocity).

Coriolis forces emerge in systems rotating as a whole, if the vectors of angular velocity of rotation $\vec{\omega}$ and the relative velocity $\vec{V}$ do not coincide. Coriolis force in a rotating coordinate system is determined by the following relation:

$$\vec{F}_{Cor} = 2\rho\vec{\omega}\times\vec{V} \tag{1.4}$$

Coriolis force is directed perpendicular to the conventional surface, formed by vectors $\vec{\omega}$ and $\vec{V}$, in that direction from which, after matching the origins of the vectors $\vec{F}_{Cor}$, $\vec{\omega}$ and $\vec{V}$, the shortest turn from $\vec{\omega}$ to $\vec{V}$ would appear to be going counter-clockwise.

Mass forces (a) can serve as a main source of fluid flow, (b) result in secondary flows (e.g. recirculation) or (c) cause a stabilizing effect onto a fluid.

However, these effects can take place only in a non-uniform field of mass forces, i.e. under condition of their spatial variation in the system. Difference of mass forces between particular locations in the system is called an excessive mass force:

$$\Delta\vec{F} = \vec{F}_2 - \vec{F}_1 \tag{1.5}$$

The excessive mass force emerges due to non-uniformity of density distribution in a fluid and/or non-uniformity in the acceleration causing the mass force. Simultaneous influence of the above factors is also possible. Shchukin (1980) showed that the characteristics of fluid flow can be affected only by the mass forces, whose value is different from the pressure gradient caused by these mass forces and counteracting with them. This means that the difference between the mass force and the counteracting pressure gradient is equal to the difference between the mass forces in two different locations of the system and is in fact the aforementioned excessive mass force. The field of mass forces can be simple or complex; in the latter case, mass forces of different nature act simultaneously in the system. On the Earth, all phenomena take place in the gravitational field, which is therefore considered to be a simple field, while any other field of mass forces will be always complemented with gravitational forces. However, gravitational force is very often insignificant in comparison with inertial mass forces, and therefore gravitational forces are quite often neglected in physical models. The vector of a mass force can make different angles with the surface counteracting with fluid flow. If the mass force vector makes an angle of 90 degree with a surface, the mass force field is called transverse. When the mass force vector is directed along the surface, the field is called longitudinal. One should also discern steady and unsteady fields of mass forces. Excessive mass forces can cause active influence on fluid flow (disturbing the flow, causing secondary flows and increasing turbulence level in turbulent flow regime) or conservative influence (stabilizing the flow, suppressing different occasional perturbations and turbulent pulsations). If mass forces comply with the inequality $\left|\Delta\vec{F}\right| > 0$, this is an evidence of conservative effect of the mass forces on fluid flow. For $\left|\Delta\vec{F}\right| < 0$, mass forces cause active effect on fluid flow (Shevchuk. 2009).

1.1.2 Consideration to rotation-shearing active micro reactor

One of the main objectives of this study is to investigate flow characteristics in a rotating-disk system with a view to develop a rotation-shearing active micro-reactor. A rotation-shearing active micro reactor under development in Nishino's laboratory is represented in Fig. 1-2. It is designed to realize extremely high-rate of mixing of two fluids as a next generation chemical reactor. Its characteristics are summarized as follows:

(1) To utilize a strong shearing motion in a sub millimeter liquid layer between the disks for remarkable enhancement of mixing of two fluids in the layer,

(2) To apply a wide range of mixing speed from laminar to turbulent fluidic dynamics,

(3) To enhance the chemical operation by two dimensionally extended channel design, which can effectively expand the chemical operational field and time.

1.2 Measurement of micro flow

With rapid development in micro-electromechanical systems (MEMS) technology, this microfluidic technology has been applied widely to various microfluidic devices such as μ-TAS (total analysis system), Lab-on-a-chip (LOC), fluidic logic devices (Gravesen et al. 1993; Stone et al. 2004), micro reactor etc. The detailed understanding of the flow inside the micro-scale passage is very important for their optimum design and active/passive control of flow. In order to observe the flow phenomena in microfluidics, a suitable experimental technique that can resolve the temporal and spatial resolutions of the given micro-scale flow is definitely needed.

Recently, quantitative flow visualization has become an important tool to investigate three-dimensional complex flow structures. The development of laser, computer and digital image processing techniques made it possible to extract velocity field information from visualized flow images of tracer particles (Adrian 1991). Particle image velocimetry (PIV)/particle tracking velocimetry (PTV) method has become one

of the most useful flow diagnostic technologies in the modern history of fluid mechanics. The particle based velocimetry techniques measure the whole velocity field information in a plane by dividing that is placements Δx and Δy of tracer particles with the time interval Δt during which the particles were displaced. Since the flow velocity is inferred from the particle displacement, it is also important to select proper tracer particles that follow the flow motion accurately without changing the flow properties.

The PIV/PTV technique is a very powerful tool for obtaining velocity field information of various flows compared with point-wise velocity measurement instruments such as hot-wire or LDV. Furthermore, other physical properties such as vorticity, deformation tensor and forces can be derived easily from the PIV data.

These methods have been accepted as a reliable and powerful velocity field measurement technique (Raffel et al. 2007). The PIV method in a strict sense provides the representative velocity vector averaged over each interrogation window. Therefore, when a flow has a velocity gradient inside the interrogation window, the PIV method cannot resolve it. On the other hand, as the PTV method can identify individual particles and track them from image to image, the PTV method has higher spatial resolution than the PIV method for low-particle-density flows such as micro-scale flows in microfluidics. We will examine two/three component micro-PIV/PTV in next section.

1.3 Two-component micro-PIV technique

In conventional two-dimensional (2D) PIV experiments, tracer particles in a measurement plane are illuminated with a thin laser light sheet. In this case, the depth of focus over which particle images are captured is defined as the thickness of the laser light sheet. However, the conventional PIV technique cannot be employed for measuring micro-scale flows to be investigated, because it is nearly impossible to make a laser light sheet with thickness in the order of 1~10μm. In micro-PIV measurements, the micro-scale flow is usually volume illuminated. Santiago et al. (1998) first used a micro-PIV system to investigate a micro-scale flow. The micro-PIV technique has advanced greatly in the last decade (Meinhart et al. 1999, 2000a, b; Olsen and Adrian

2000a, b; Wereley et al. 2002; Olsen and Bourdon. 2003; Meinhart and Wereley. 2003). Recently, a time-resolved micro-PIV technique was developed to measure the temporal evolution of micro-scale flows inside microfluidic devices. During the last decade, the micro-PIV technique has been applied to various micro-scale flows such as a pressure driven flow inside a microfabricated inkjet head (Meinhart and Zhang. 2000), electrokinetic flow (Cummings. 2000), electro-osmosis-driven microchannel flows (Kim et al. 2002), flows with apparent slip velocity (Tretheway and Meinhart. 2002, 2004), two-fluid flow with different refractive indices (Kim et al. 2004), and transient flow in microfluidic devices (Shinohara et al. 2004). In addition, the micro-PIV technique has been applied to measure biological flows such as blood flows. For example, velocity field information of blood flows in various bio-samples such as zebra fish, rat, and chicken embryos were measured in vivo using the micro-PIV technique (Hove et al. 2003; Sugii et al. 2002; Lee et al. 2007). A detailed technical explanation for the micro-PIV is described in chapter 2.

1.4 Three-components micro-PIV technique

1.4.1 Stereoscopic micro-PIV/PTV

A micro-PIV system measures 2-D velocity field information in the depth-of-field region under the volume illumination. However, it cannot resolve the out-of-plane velocity component of a 3-D flow. The stereoscopic micro-PIV (SMPIV) and PTV (SMPTV) are microscopic version of the stereoscopic PIV/PTV system which has been used for measuring the out-of-plane motion (Lindken et al. 2005, 2006; Bown et al. 2005, 2006; Giardino et al. 2008, Yu et al. 2009).

The general feature of the SMPIV/SMPTV method is similar to that of the conventional stereoscopic PIV/PTV method. It is a 2D-3C measurement method rather than 3-D volume measurement methods such as holographic and defocusing micro-PTV methods. Compared to the conventional microscope of micro-PIV system, the SMPIV/SMPTV uses a stereoscopic microscope. However, the stereoscopic microscope has a small *NA* value and low magnification power. Therefore, the stereoscopic microscope requires strong light to illuminate seeding particles and the velocity gradient

along the depth direction can cause some measurement errors due to the large depth-of-field. The newest stereoscopic microscope (e.g., Leica Planapo 2×) has a 20× magnification with *NA* value of 0.35. This *NA* value is much smaller than that of a conventional microscope of 40× with *NA*=0.65 (e.g., Zeiss A-pan 40×/0.65). The magnification power of the stereoscopic microscope can be improved by using relay optics (Giardino et al. 2008). However, since the low *NA* value is an intrinsic feature of the stereoscopic microscope, the spatial resolution of the SMPIV/SMPTV is lower than that of the conventional 2-D micro-PIV/PTV methods.

The SMPIV/SMPTV method can be configured into two different stereoscopic configurations; a Greenough type and a common main objective (CMO) type (Danuser and Kübler 1995). The two schematic configurations are illustrated in Fig. 1-3 (Yu et al. 2009). The CMO-type microscope has the translational configuration in the stereoscopic imaging and the Greenough-type microscope provides the angular displacement type stereoscopic configuration. In the translation configuration method, the optical axis of the first camera is parallel to that of the second one. These optical axes are aligned to be perpendicular to the illuminated plane. However, the two optical axes of the angular configuration are neither parallel nor perpendicular to the measurement plane, because the image planes are tilted to focus the whole measurement volume. The tilting of image planes and camera lenses can cause image distortion and magnification variation, requiring an elaborate calibration process to obtain accurate experimental data (Yoon and Lee. 2002). The Greenough type consists of two separate compound microscopes, whereas the CMO type uses a common main objective lens. The CMO-type microscope has good sharpness throughout the entire field-of-view (FOV) and provides good image quality due to its relatively high value of *NA*. The microscope is easily fitted with a polarizing attachment. The Greenough type has a very limited observation area where the 3D sample appears sharply due to the tilted beam paths. The correction for optical aberrations caused by this Greenough-type microscope is easier than for the CMO type, since the two objective lenses are smaller, axially symmetrical, and do not rely heavily on the light rays passing through periphery of the objective lens. Due to the tilted beam path, the Greenough-type microscope has larger depth of focus, compared to the CMO-type microscope. Yu et al. (2009) found that the CMO-type optical configuration has smaller bias and rms errors than those of Greenough-type configuration.

The SMPIV and SMPTV methods can be categorized by the method of extracting the out-of plane velocity component. The SMPIV method proposed by Lindken et al. (2005, 2006), and Giardino et al. (2008) is just a microscopic version of the conventional stereoscopic PIV method. The velocity vector calculated using the cross-correlation algorithm provides the representative velocity vector averaged over each interrogation volume. That is, all the three velocity components are Eulerian. The spatial resolution was about 44×44×15μm. To improve the spatial resolution, Bown et al. (2005, 2006) applied a PTV algorithm using the super-resolution method (Keane et al. 1995) to develop a SMPTV method. They used the preliminary PIV results to track the tracer particles, which could provide three-dimensional Lagrangian velocity components. The spatial resolution was about 10×10×10μm, higher than that of the SMPIV method. As they employed a constant illumination method with long exposure time, the dynamic range was restricted to 10μm/s. Yu et al. (2009) developed a SMPTV method by employing a two-frame PTV algorithm (Baek and Lee 1996) into a stereoscopic micro-PIV technique. Different from the SMPTV of Bown et al. (2005, 2006), this method does not use the PIV results in the particle tracking process. They used the PTV algorithm for measuring in-plane velocity components and applied the stereoscopic approach to calculate the out-of-plane velocity component. Therefore, the velocity vectors consist of two Lagrangian (in-plane motion) and one Eulerian (out-of-plane motion) components. The particle density in a micro-scale flow is generally low and the PIV algorithm is usually useful for high-particle-density flows. To increase the particle density in the interrogation window, Bown et al. (2006) adopted the ensemble averaging technique which uses numerous particle images. However, this ensemble averaging method can be used only for steady flows. As a shortcoming, the measurement volume of the SMPIV/SMPTV method is restricted to a relatively small depth-of-focus region which is determined by the objective lens. Therefore, if the depth of the measurement volume is larger than the depth of focus, the SMPIV/SMPTV method requires a scanning process to get the whole velocity field information inside the measurement volume. To conclude, the SMPIV/SMPTV method can easily measure the out-of-plane motion of a micro-scale flow. However, the depth of the measurement volume is relatively small. When the true Lagrangian three-component velocity field information

in a 3-D volume of large depth is needed to be measured, it would be better to choose the option of other 3-D micro-PIV/PTV methods such as holographic PTV and defocusing PTV.

1.4.2 De-focusing micro-PTV

Yoon and Kim (2006) developed a defocusing micro-PTV (DMPTV) method to detect 3-D particle positions in a 3-D volume of micro-scale flows using the calibration-based defocusing concept. The DMPTV method developed by them was found to be accurate and convenient in the estimation of 3-D particle locations in a measurement volume.

The basic concept of defocusing of DMPTV is the same as that used for macro-scale 3-D flow measurements. A mask with three pinholes arranged at the vertices of an equilateral triangle is positioned on the objective lens as shown in Fig. 1-4. The light passing through these three pinholes reaches three different positions on the image plane. The side distance between the triangular vertices in the image plane increases as the particle position moves away from the focusing plane (reference plane). Hence, the particle positions in the depth direction can be estimated from the size of the defocused triangular pattern formed on the image plane. Using modern microscopic lenses, it is possible to adopt multi-lenses in a complex configuration. In addition, the distance from the lens vertex to the representative lens plane is relatively large. In practice, the distance is much larger than the working distance of a microscope. The errors caused in the alignment procedure can be exacerbated due to high magnification. Previous studies (Kajitani and Dabiri. 2005; Pereira and Gharib. 2002) assumed that the lens plane was positioned at the same plane as the pinhole mask and that the pinholes were equidistant from the optical axis. These assumptions should be carefully checked in the experiments using a DMPTV system.

Figure 1-5 shows a typical defocused particle image of water flow in a microchannel having a backward-facing step (Yoon and Kim. 2006). This image was captured by a DMPTV system with inverted light intensities. The DMPTV system consists of a CCD camera, an argon-ion laser, and a microscope equipped with a long-pass filter cube. A 12 bit cooled CCD camera with 1K × 1K pixels resolution was used to investigate the effects of pinhole mask on the micro-PIV measurement. By using a 20× objective lens, the field of view was 768μm wide × 388μm high. A mask with three pinholes was

attached just behind the objective lens. To remove scattering noises, fluorescent particles 3μm in diameter were seeded into the working fluid. A long-pass filter with a 560nm cutoff was attached in front of the camera. An image intensifier can be employed to resolve the low-light-intensity problem caused by the small pinholes.

The light intensities of particle images in the dashed square region of Fig. 1-5 show peak values. Each particle image was processed using a Gaussian spatial filter to reduce noise, and then the intensity peaks were traced through the whole image plane with a sub-pixel resolution. The large-scale triangular patterns shown downstream of the back-ward facing step indicate that those particles are positioned at a great depth from the free surface. Velocity vectors were calculated from the 3-D position information of the tracer particles. The mean velocity field was obtained by ensemble-averaging 2,000 instantaneous velocity fields in the measurement volume. The spatial resolution was 5 μm in x and y axes and 1μm in z axis. The defocused micro-PTV method can be used to measure 3-D velocity field of various micro-scale flows. It provides a convenient and simple means of estimating 3-D particle locations in a micro-scale volume with a sub-micron resolution. However, the loss of light intensity caused by the small pinholes and the relatively small number of extracted vectors are drawbacks of the DMPTV method.

1.4.3 Digital holographic micro-PTV

Digital holography is an optical method to record 3D volumetric field information on a digital hologram utilizing a digital imaging device. The digital hologram can be numerically reconstructed and processed for extracting 3D information (Schnars and Jüptner. 1994). This holography technique does not need the complex physical and chemical processing routines essential for the film-based holography.

The simple and convenient data acquisition processing promotes the application of this digital holography technique in various research fields, including metrology, deformation measurement, vibration analysis and biological microscopy. It provides not only quantitative phase information but also high-fidelity images with a good precision.

With recent advances in the in-line digital holography technique, it is now possible to get 3-D velocity field information of 3-D flows by using a procedure with simple hardware system (Meng et al. 2004). By adopting a high-speed digital camera, the time-

resolved holography of particle fields can be employed to measure the temporal evolution of 3D velocity field of a flow with the help of a 3-D particle tracking algorithm. However, the spatial resolution of digital image sensors currently available is about 100 *lp*/mm, which is several orders lower than that of holographic films. As a result, the angular aperture of digital hologram is much smaller than that of the film-based holograms. This results in the axial elongation of reconstructed particles, causing measurement errors in the determination of their axial position. To resolve this problem, Sheng et al. (2006) introduced a digital holographic microscope technique which utilizes a microscope objective to magnify the hologram image. This method greatly increases the spatial resolution of digital holography; however, the acquirable field of view is reduced as the compensation. For example, the digital hologram obtained by a 209 objective lens covers about several hundred micrometers cubic. Recently, this technique was successfully applied to measure the near-wall velocity and wall shear stress in a turbulent boundary layer (Sheng et al. 2008).

1.5 The objective of the present study

In these rotating systems, the main design parameters such as friction torque by shear stress, power loss, and heat transfer are strongly related to the flow induced by the rotating disk such as the circulation and secondary flows. These induced flows also depend on the geometries of the stationary and rotating disks, such as the gap between stationary and rotating disk, the radius and the angle of rotation disk and so on.

In the present study, the shear-driven micro flow in a rotating disk system is investigated experimentally and computationally.

The objectives of the present study are

(1) To develop compact integrated two/three dimensional micro-PIV/PTV systems and to investigate the characteristics of shear-driven micro flow between stationary and rotating disks,

(2) To develop a digital image filtering technique which is implemented for a conventional micro-PIV technique, in order to resolve a steep velocity gradient in shear-driven micro flow, particularly in the region adjacent to the rotating wall,

(3) To develop a new measuring method in three-dimensional micro-PTV with stereo viewing attachment, and

(4) To propose analytical equations to predict shear-driven micro flow between stationary and rotating disks and to compared with CFD results.

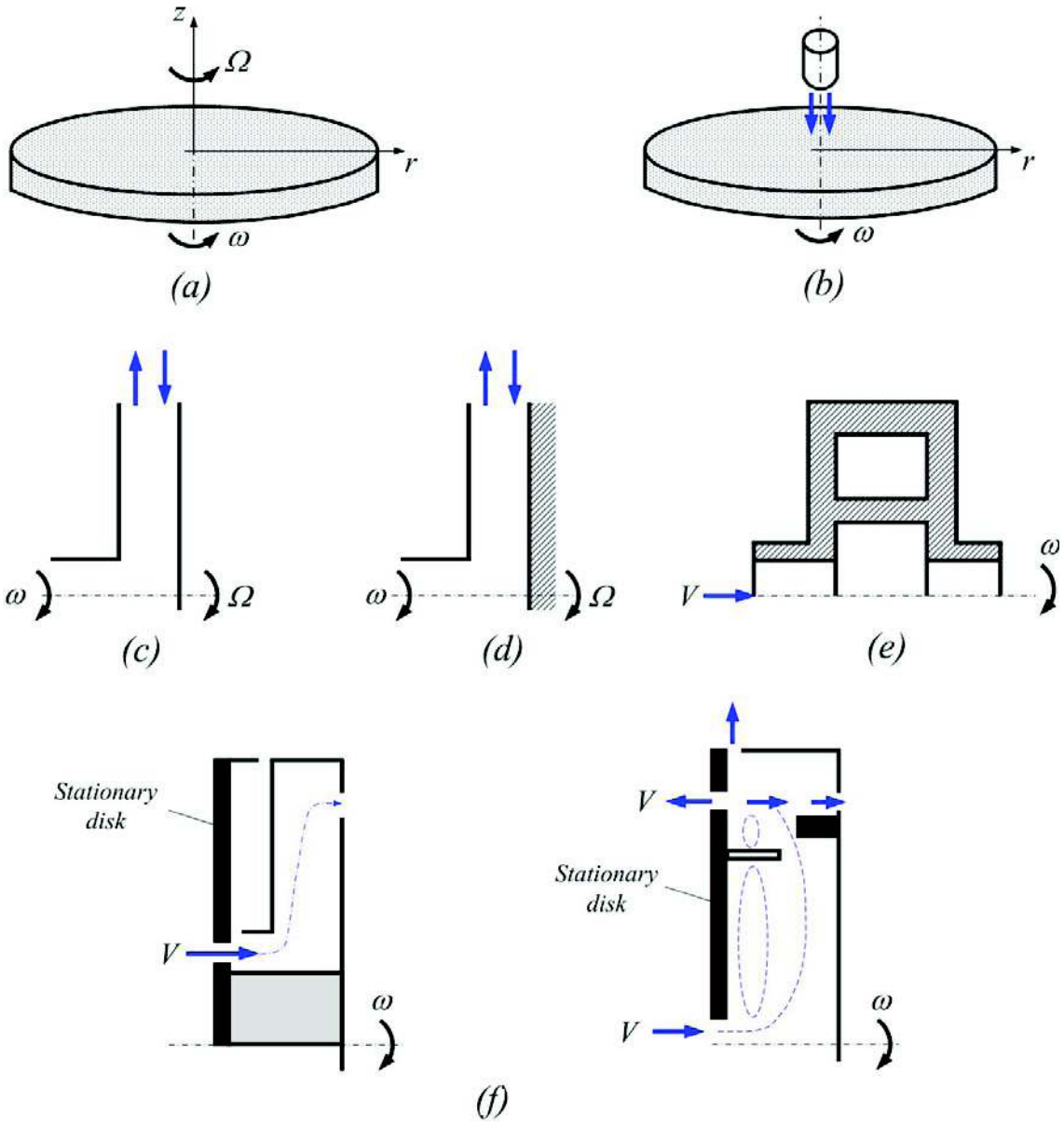

Figure 1-1 Rotating-disk systems: (a) rotating disk in an infinite resting fluid, (b) rotating disk for impinging jet-cooling, (c) co-rotating disks parallel disks with and without forced radial through flow, (d) stationary and rotating disks to generate a strongly-sheared flow, (e) two disks and two cylindrical surfaces for the closed non-ventilated cavities of gas turbines, (f) rotating disk shroud for air cooling systems with inlet flow pre-swirl.

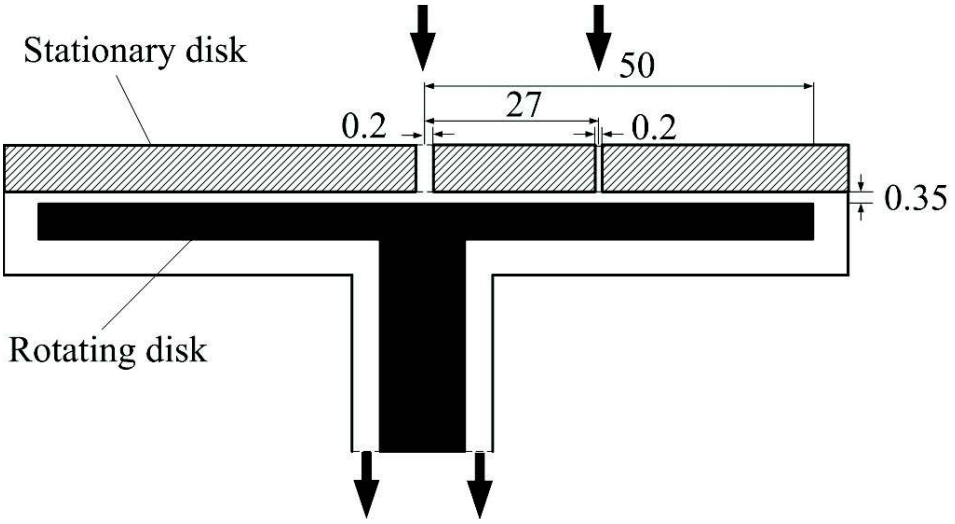

(a)

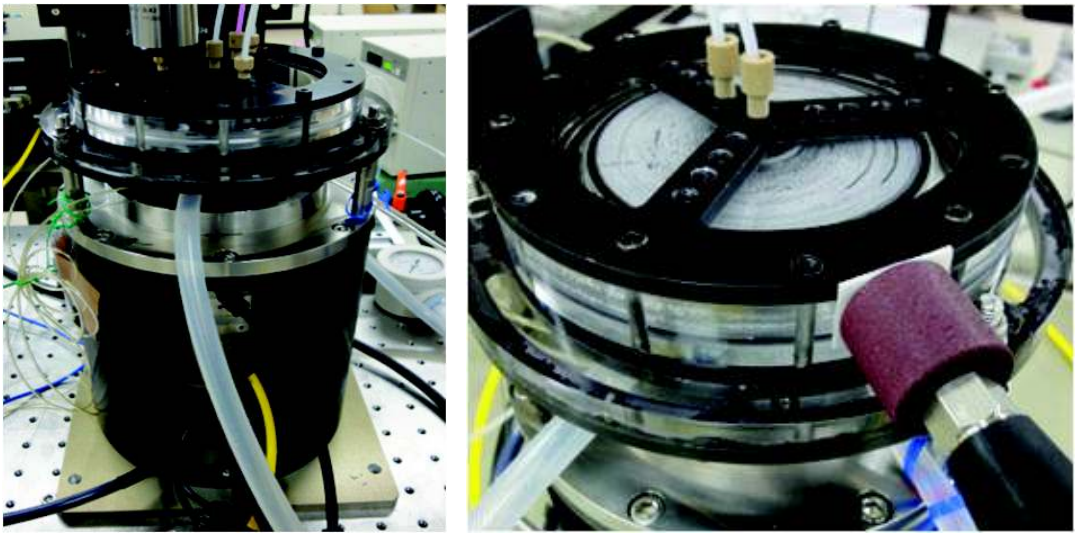

(b)

Figure 1-2 Schematics (a) and pictures (b) of rotation-shearing active micro reactor.

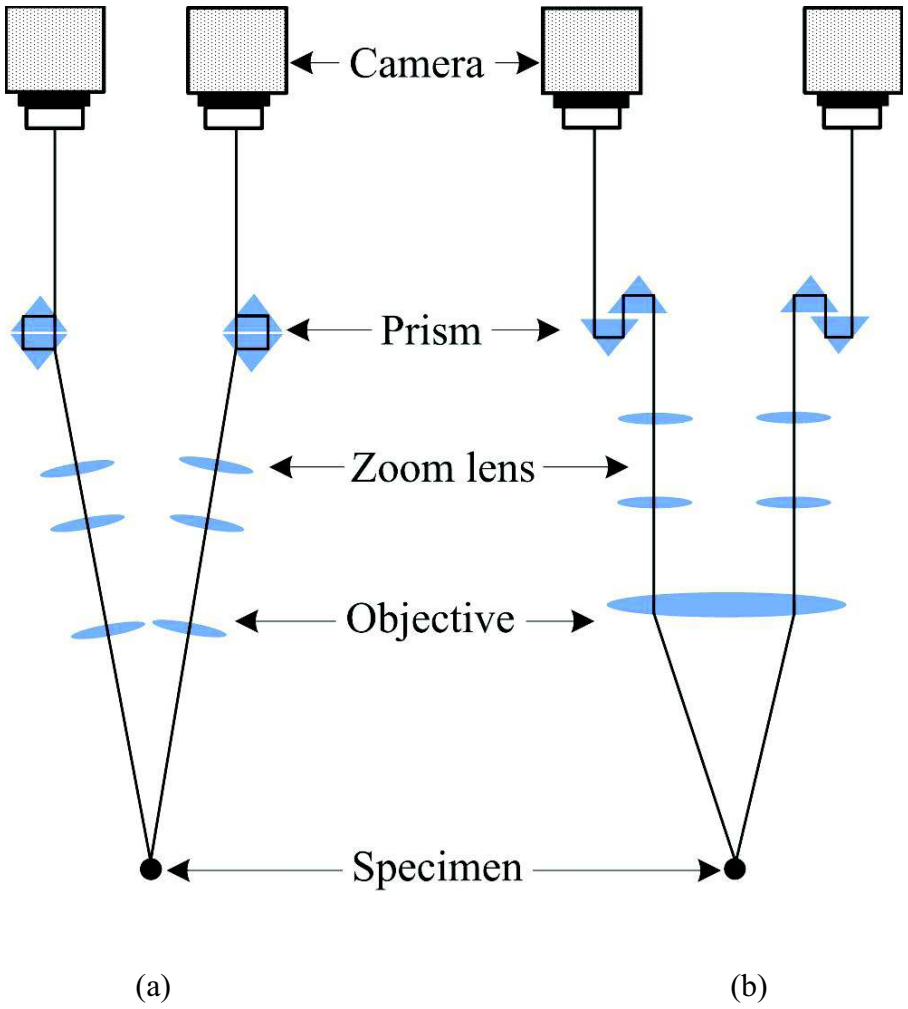

Figure 1-3 Two different configurations of stereoscopic micro-PIV system (a) angular configuration with Greenough type (b) translation configuration with CMO type.

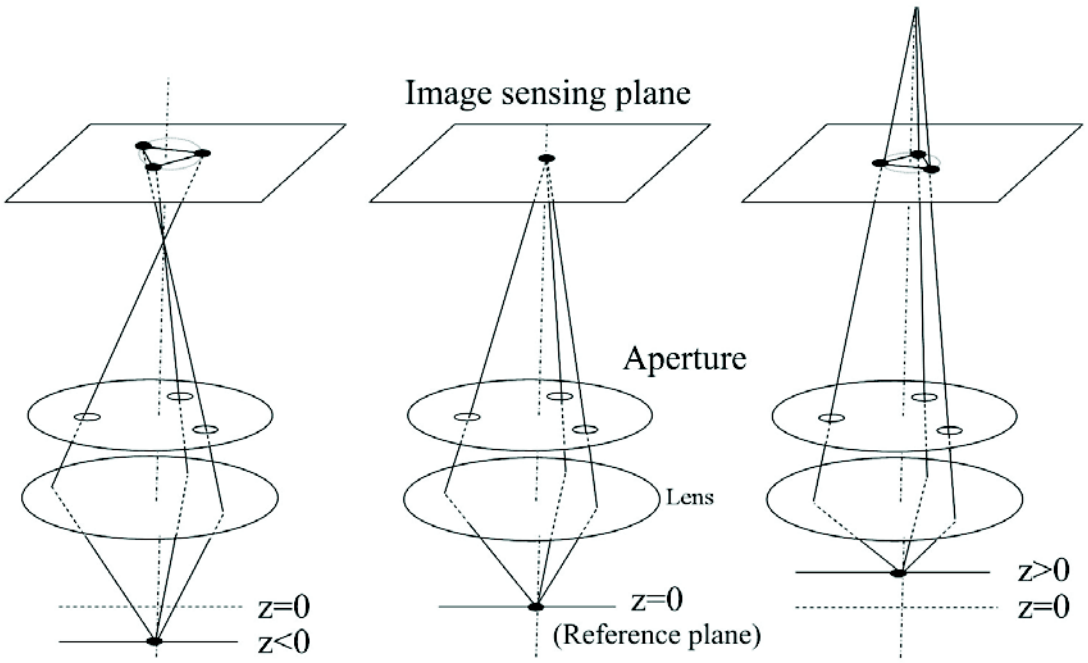

Figure 1-4 Basic concept of the de-focusing micro-PTV technique.

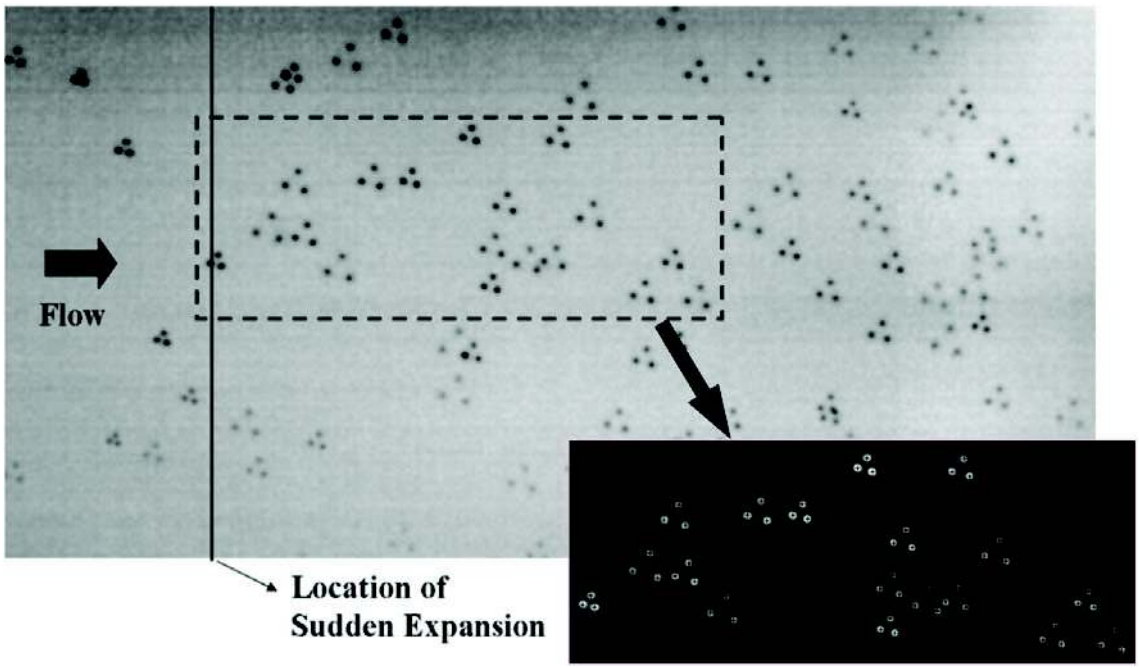

Figure 1-5 A typical de-focusing particle image of a micro-scale backward-facing step flow.

Chapter 2. Micro Particle Image Velocimetry

Particle Image Velocimetry (PIV) is a well-established measurement technique for macro-scale flows, and it is extensively described in the various literatures (Raffel et al. 1998, Adrian. 1991). Micro-PIV (Micro Particle Image Velocimetry) is a modification of PIV to measure the small scales having micro-sized passage.

The first micro-PIV experiment was carried out by Santiago et al. (1998), where the velocity field in a Hele-Shaw flow around a 30μm elliptical cylinder was measured. The system used a CCD (Charge Coupled Device) camera, a microscope with fluorescence unit, fluorescent tracing particles, and an Hg-arc lamp for continuous illumination.

Meinhart et al. (1999) demonstrated a micro-PIV system consisting of the same general components with the exception that the continuous light source was replaced by two pulsed Nd:YAG lasers. The technique was applied to a microchannel flow, and results with high spatial resolution and accuracy were reported.

The main objective of chapter 2 is to provide the theoretical and technical methods to understand a micro-PIV system and technical technique.

2.1 Basic theory of micro-PIV

Micro-PIV is a whole-field, non-intrusive measurement technique, where the fluid velocity is measured by recording the displacement of fluorescent tracing particles seeded into the fluid. A single PIV measurement produces a velocity vector field of high spatial resolution. The technique is based on the following simple principle.

When a single fluorescent tracing particle in a fluid flow exists, it is assumed to have the same density as the surrounding fluid and enough small size to follow flow without influencing the flow itself. Figure 2-1 shows records of the position of the particle in two time instants separated by a short time interval Δt. If Δt is sufficiently short, the displacement of the particle, Δs, is also small enough so that the direction and magnitude of the particle velocity during Δt can be assumed constant and the acceleration is negligible. Then, the local fluid velocity can be calculated as:

$$u \approx \frac{x_{t+\Delta t} - x_t}{\Delta t} = \frac{\Delta s}{\Delta t} \tag{2.1}$$

The simple idea described above can be extended to an entire flow field. In PIV, the working fluid is seeded with small tracer particles, and the flow-field of interest is illuminated by a powerful light source. The light emitted from the particles (particle images) is recorded on CCD array at two different time instants separated by Δt. As a single image pair contains hundreds or thousands of particles, the images are divided into small sub-areas, so-called interrogation window. Each window is analyzed by some correlation method to find the local displacement vector Δs, and the velocity magnitude and vector field is calculated.

2.2 Volume illumination

In general macro-PIV, a thin sheet of laser light is generated to illuminate a single plane within the fluid flow. The laser sheet, which is usually thinner than the focal depth of the camera lens, defines the measurement plane of the PIV system, as only particles within the laser sheet scatter light and are recorded by the CCD camera.

However, in micro-PIV, illumination of a single plane within micro-scale passage is not easy task. The main reasons for this are as follows:

(1) Many micro-scale devices are manufactured by some and sealed by bonding a glass cover on top of the device. Hence, optical access is limited of illuminating laser sheet to one direction.

(2) The dimensions in devices measured are typically in the range of tens or few hundreds of microns and the measurement plane thickness is required only a few micrometers. Obtaining such a thin light sheet is not simple, while its alignment with the imaging optics' focal plane is nearly impossible for practical purposes (Meinhart et al. 2000a). Therefore, in micro-PIV, the entire flow-field is illuminated, and the measurement plane is determined by the characteristics of the microscope objective.

2.3 Basic components of Micro-PIV system

A typical micro-PIV system consists of a CCD camera, a microscope equipped with fluorescent filter/cube, a light source for flow illumination, usually a laser, and appropriate optics. A schematic illustration of a micro-PIV system employing a microscope is shown in Fig. 2-2. The laser beam is expanded in an appropriate manner by means of a beam expander and/or other equivalent optics (using expanded optical fiber in the present study) before entering the microscope.

The beam then enters the microscope through an aperture and is reflected 90° upwards by a dichromatic mirror. The dichromatic mirror is chosen such that it functions as a long-pass filter, reflecting wavelengths below a certain pass wavelength λ_{pass}, and transmitting all higher wavelengths. In this case, λ_{pass} must be higher than the wavelength of the laser light (λ_{laser}). Finally, the light is transmitted through the microscope objective, and the flow field of interest in the micro-scale passage is illuminated. The fluorescence signal emitting from tracer particles, along with reflections from surfaces of the micro-scale passage, is collected by the microscope objective and travel back to the dichroic. The fluorescent dye for the particles is chosen such that its peak excitation wavelength λ_{abs} closely matches λ_{laser}, and its emission peak wavelength λ_{emit} is longer than λ_{pass} of the dichromatic mirror.

In this manner, the dichromatic mirror filters out all reflected light (noise), only transmitting the fluorescence signal from the particles. In most cases, another long-pass filter is applied immediately downstream the dichroic mirror (with a slightly higher λ_{pass}) to ensure satisfactory filtration.

Finally, the signal from tracer particles is recorded onto a CCD array, the latter greatly simplifying post-processing and image analysis. In addition to the components shown in Fig. 2-2, a complete micro-PIV system consists of a PC for image acquisition and analysis, and some systems for synchronization and control of lasers, etc.

2.4 Fluorescence

Due to the mode of illumination and accompanying noise issues, elastic scattering (i.e. light scattering by pure reflection) is not suitable for micro-PIV. Instead, the seeding particles must emit light at a wavelength λ_{emit} different from the wavelength of the

illumination source λ_{laser}. This is accomplished by means of fluorescence imaging. A brief description of fluorescence and its underlying phenomena is given in the following.

2.4.1 Physical background

Fluorescence is the emission of photons by an atom or molecule following a temporary excited electronic state caused by absorption of photons of a certain wavelength from an external radiation source (Murphy. 2001). A molecule capable of fluorescence is called fluorochrome or fluorescent dye. When a fluorochrome absorbs a photon with energy E_1, an electron is excited from its ground state E_0 to a higher energy state (excited state 1) corresponding to the energy of the absorbed photon as shown in Fig. 2-3.

Due to the fluorochrome's interactions with its molecular environment during the excited state, there is some loss of energy resulting in a relaxed excited state with energy E2 (excited state 2) from which fluorescence emission originates; after a short time period (typically $10^{-9} \sim 10^{-12}$ seconds) the excited electron collapses back to its ground state, emitting a photon with energy corresponding to the difference between the electron's excited and ground states, i.e. $E_2 - E_0$. The energy of a photon is given by:

$$E = \frac{hc}{\lambda} \tag{2.2}$$

,where h is Planck's constant, c is the speed of light, and λ is the wavelength. As the energy of the emitted photon is lower than that of the absorbed photon, i.e. $E_2 < E_1$ as discussed above, the wavelength of the fluorescent emission λ_{emit} is longer than that of the absorbed radiation λ_{abs}.

2.4.2 Spectral characteristics

A fluorochrome can absorb photons over a spectrum of wavelengths, so-called excitation spectrum. The excitation spectrum may be of various shapes and contain one or more excitation maxima depending on the nature of the fluorochrome.

Due to variations in electrons' residence time in the excited state, and hence variations

in energy loss prior to fluorescent emission, fluorochromes also emit photons over a continuous spectrum of wavelengths, even when excitation is performed by a monochromatic light source such as a laser (emission spectrum). The excitation and emission spectra are distinct, although they often overlap, sometimes to the extent that they are indistinguishable. The difference between a fluorochrome's peak excitation and emission wavelengths is termed Stokes' shift (Murphy. 2001). A general illustration of excitation and emission spectra with corresponding Stokes' shift is shown in Fig. 2-4.

2.5 Imaging using microscope

2.5.1 Flow illumination through microscope objective

An important consequence of the application of infinity-corrected objectives in micro-PIV is that a collimated light beam cannot be used for illumination, as the beam is then focused to a single point instead of illuminating the entire field of view of the microscope (see Fig. 2-5a). Due to the high laser power, the focused beam may damage the micro-scale passage. In order to achieve volume illumination, a lens with a negative focal length (concave lens) must be introduced in the light path up-stream the dichromatic mirror. In this way, the focal spot of the illuminating light created by the objective is shifted to a plane further away from the front lens, and does not coincide with the microscope's objective focal plane. Instead, the cone of laser light emerging from the objective's front lens is 'sliced' by the objective focal plane, thereby illuminating a portion of the microscope field of view (see Fig. 2-5b). The extent of the illuminated field depends on the the half-cone angle α of the beam entering the rear iris of the objective lens. The maximum achievable angle is in turn governed by the rear iris diameter and the distance between the concave lens and the objective. In order to achieve a sufficiently large illuminated field, the concave lens should be placed immediately upstream the dichromatic mirror.

2.5.2 Numerical aperture

The Numerical Aperture (NA) gives a measure of two important objective characteristics, namely its light-gathering ability and its ability to resolve fine detail in a specimen. The numerical aperture is defined as:

$$NA = n\sin\theta, \tag{2.3}$$

where n is the refractive index of the objective's working medium, and θ is the half-angle of the light collecting cone in represented in Fig. 2-6.

Equation (2.3) means that the NA number is increased with increasing the angle of the light collecting cone θ, which corresponds to increasing the aperture diameter and/or decreasing the working distance (see Fig. 2-6), or by applying a working medium with high index of refraction, n. As the working distance generally decreases with increasing magnification, high magnification objectives have the highest NA numbers.

For example, the refractive index of air is $n_{air} = 1.0$, and hence NA above 1 is impossible to obtain when air is the working medium. In practice, the highest obtainable NA for air immersion objectives is 0.95, and only for high magnifications. Increasing the NA above 1.0 requires a working medium with refractive index n above 1.0. Oil ($n_{oil} = 1.515$) is the most common immersion medium for this purpose.

2.5.3 Image brightness

The visual field brightness, or image brightness (B), of a microscope image is determined by the square of the ratio between the numerical aperture of the objective and its magnification factor M:

$$B_{trans} \propto \left(\frac{NA}{M}\right)^2, \tag{2.4}$$

which implies that image brightness may be increased by applying an objective of high NA, while keeping magnification at the lowest level compatible with desired resolution.

The ratio given by equation (2.4) applies for trans-illumination. For epi-illumination, however, the objective also functions as a condenser for the illuminating light, introducing another factor of NA^2 in the numerator of equation (2.4), which yields:

$$B_{epi} \propto \left(\frac{NA^2}{M} \right)^2 \tag{2.5}$$

Hence, in epi-illumination, the image brightness B_{epi} varies proportionally to the fourth power of NA, while its dependence on magnification remains the same as for trans-illumination. The change in image brightness with increasing NA is significant. Given an air-immersion objective with numerical aperture of 0.8, the image brightness for an oil-immersion objective with $NA = 1.4$ (with the same magnification) is approximately an order of magnitude higher. In micro-PIV, where the fluorescent signal from tracer particles is weak, the importance of selecting a high NA objective is apparent. In practice, the image brightness numbers also vary somewhat due to differences in the objective rear aperture diameter. Some values of image brightness B_{epi}, magnification M and NA corrected for objective geometry are listed in Table. 2-1.

2.6 Seeding particles

The choice of seeding particles for a micro-PIV experiment requires careful considerations, as the particle properties are of major importance with regard to the accuracy and spatial resolution of the measured data. The most important factors of influence are described in the following sections.

2.6.1 Fluid mechanical properties

One of the inherent assumptions of PIV is that the tracer particles faithfully follow the flow without exerting any influence on the flow itself. Thus, the particle density ρ_p should closely match the density of the fluid ρ_f in order for the particle, at zero-velocity conditions, to stay suspended in the fluid without sinking nor floating up due to

gravitational effects and buoyancy.

For gas flows, this requirement may be difficult to satisfy. For liquid flows, however, particles meeting this condition are readily available. For water flows, for instance, a great variety of polystyrene particles with density of 1.05g/cm^3 are available from a number of manufacturers.

In an accelerating flow, a particle has a tendency to "hang" behind due to inertia effects. This phenomenon is called as velocity lag, and its extent depends on the particle diameter d_p in addition to the density ρ_p.

Applying Stokes' drag law, the following estimate of the particle velocity may be derived (Raffel et al. 1998):

$$u_p(t) = u\left[1 - \exp(-\frac{t}{\tau_s})\right] \tag{2.6}$$

In equation (2.6), a spherical particle in a viscous, low *Re* flow with continuous acceleration is assumed. $u_p(t)$ is the velocity of the particle, u is the fluid velocity, and τ_s is the relaxation time given by:

$$\tau_s = d_p^2 \frac{\rho_p}{18\mu} \tag{2.7}$$

Despite the restricted validity of equation (2.6) and (2.7), τ_s is a good indicator of the ability of a particle of certain size and density to respond to fluid acceleration.

Equation (2.6) is plotted for three different particle diameters in Fig. 2-7. It is clearly seen that the particle response time decreases considerably with particle diameter. In micro-PIV, d_p is typically in the range between 0.2 ~ 5.0μm.

For a 3μm polystyrene particle in water, the response time calculated using equation (2.6) is ~5μs ($u_p(t)/u = 1$). The errors due to velocity lag should be negligible in micro-PIV applications.

2.6.2 Fluorescence properties

An important consequence of volume illumination is that light is not only scattered by particles within the fluid, but reflections also occur on the walls of the micro-scale passage, creating a strong background noise. This problem is overcome by using fluorescent particles and an appropriate filter cube/plate to separate the fluorescent signal from the reflected laser light. The fluorescence properties of seeding particles are thus important with respect to the quality of particle images.

In micro-PIV, a large Stokes' shift is desirable in order to enable effective filtration of the illumination source wavelength by optical filters and dichromatic beam splitters. Tracer particles dyed by fluorochromes with Stokes' shifts around 30nm are readily available from various manufacturers. Higher Stokes' shifts can be obtained with special dyes or by fluorescence resonance energy transfer (FRET) (Haugland. 2001). FRET is an interaction between two fluorochromes, where the emission of one is coupled with the excitation of the other. If properly designed, the energy transfer between fluorochromes is highly effective resulting in virtually nonexistent stray emission of the interaction wavelength and very bright fluorescence emission at the longest emission peak wavelength. Stokes' shifts of 70nm and above can be obtained using this technique. Tracer particles can be labeled or tagged by a fluorescent dye either by surface attachment or by dye entrapment (Bangs Laboratories. 2001).

In surface attachment, the fluorochromes are bound to the surface of the particle. In dye entrapment, the fluorophores are diffused into the polymer matrix of the particle by application of a solvent followed by evaporation. The latter technique is only applicable to particles made of certain materials, but it allows higher load of fluorescent dye, thereby resulting in particles with brighter emission properties.

In micro-PIV, the fluorescence properties of tracer particles are very important for successful particle imaging. First, the excitation wavelength λ_{abs} of the fluorescent dye bound or entrapped within the particles should closely match the wavelength of the laser (or other light source) used for flow illumination in order to ensure high fluorescence intensity. Second, the Stokes' shift of the dye should be fairly large, so that effective filtration of the illumination wavelength by optical filters and dichromatic beam splitters may be performed without loss of the emitted fluorescence signal. Third,

the particles should be heavily loaded with dye in order to produce visible images, implying that they should be labeled by dye entrapment.

2.7 Depth of field

Meinhart et al. (2000) defined the measurement depth as twice the distance from the center of the object plane to a location such that the imaged particle is sufficiently unfocused, and thus has low enough intensity, so that it does not significantly contribute to the velocity measurement. They reported that this occurs when the intensity of the imaged particle drops below 10% of the maximum intensity of a focused particle, and is derived for the measurement depth by considering the contributions of diffraction, geometrical optics and the finite size of the particle. The derived theoretical estimation was demonstrated experimentally and showed good agreement with the experimental data. In the following section, the theoretical background of this estimation and its derivation are presented.

2.7.1 The effect of diffraction

The intensity distribution of the three-dimensional diffraction pattern of a point source imaged through a circular aperture of radius a can be written in teams of the dimensionless diffraction variables (u, v) : (Born & Wolf. 1999)

$$I(u,v) = \left(\frac{2}{u}\right)^2 \left[U_1^2(u,v) + U_2^2(u,v)\right] I_0 \tag{2.8}$$

and

$$\begin{aligned} I(u,v) = \left(\frac{2}{u}\right)^2 \Bigg\{ & 1 + V_0^2(u,v) + V_1^2(u,v) \\ & - 2V_0(u,v)\cos\left[\frac{1}{2}\left(u + \frac{v^2}{u}\right)\right] \\ & - 2V_1(u,v)\cos\left[\frac{1}{2}\left(u + \frac{v^2}{u}\right)\right]\Bigg\} \end{aligned} \tag{2.9}$$

where $U_n(u,v)$ and $V_n(u,v)$ are the so-called Lommel functions, which may be expressed as an infinite series of Bessel functions of the first kind:

$$U_n(u,v) = \sum_{s=0}^{\infty}(-1)^s\left(\frac{u}{v}\right)^{n+2s} J_{n+2s}(v)$$

$$V_n(u,v) = \sum_{s=0}^{\infty}(-1)^s\left(\frac{v}{u}\right)^{n+2s} J_{n+2s}(v) \tag{2.10}$$

and

$$I_0 = \left(\frac{\pi a^2|A|}{\lambda f^2}\right)^2 \tag{2.11}$$

is the intensity at the geometrical focus $u = v = 0$. The dimensionless variables u and v are defined as:

$$u = 2\pi\frac{z}{\lambda}\left(\frac{a}{f}\right)^2 \quad , \qquad v = 2\pi\frac{r}{\lambda}\left(\frac{a}{f}\right)^2 \tag{2.12}$$

where z is the out-of-plane coordinate and r is the in-plane radius, λ is the wavelength of light and f is the radius of the spherical wave approaching the aperture.

f may be approximated as the focal length of the lens. The main concern of the current analysis is the out-of-plane intensity distribution, i.e. the intensity along the optical axis where $r = v = 0$. By inspecting equations (2.8) and (2.9) together with the Lommel functions given in equation (2.11), it is clear that an expression for $I(u,0)$ must be derived from equation (2.9), as setting $v = 0$ in equation (2.8) yields division by zero in evaluation of the accompanying Lommel functions U_1 and U_2.

Equation (2.9) involves the functions V_0 and V_1, which must be evaluated for $v = 0$. The results are:

$$V_0(u,0) = J_0(0) = 1 \quad , \qquad V_1(u,0) = 0 \tag{2.13}$$

where $J_0(x)$ is the 0th order Bessel function of the first kind, which has the value of 1 when evaluated at $x = 0$ (see e.g. Kreyszig. 1993).

Inserting these values into equation (2.9), the result becomes:

$$I(u,0) = \left(\frac{2}{u}\right)^2 \left[2 - 2\cos\left(\frac{u}{2}\right)\right] I_0 = \left(\frac{\sin\left(\frac{u}{4}\right)}{\frac{u}{4}}\right)^2 I_0 \quad , \tag{2.14}$$

where the relation $\sin^2(a) = (1/2)(1-\cos(2a))$ has been employed to achieve the final form on the right hand side. Equation (2.15) represents the intensity distribution along the optical axis of an imaging system. Dividing both sides of equation (2.14) by the maximum intensity I_0, and applying the condition of 10% fractional intensity as a limit for contribution to the velocity measurement, yields:

$$\left(\frac{\sin\left(\frac{u}{4}\right)}{\frac{u}{4}}\right)^2 = \frac{I(u,0)}{I_0} = 0.1 \tag{2.15}$$

Simplifying and solving (implicitly) for u:

$$u = \pm 12.65 \sin\left(\frac{u}{4}\right) \quad \Rightarrow \quad u \approx 3\pi \tag{2.16}$$

Substituting this value of u into its definition given in equation (2.12), and solving for $2z$ gives:

$$2z = 3\lambda\left(\frac{f}{a}\right)^2 \tag{2.17}$$

Using the definition of numerical aperture $NA = n\sin\theta \approx n\frac{a}{f}$ and rewriting $\lambda_0 = n\lambda$, the measurement depth due to diffraction $\delta z_d (= 2z)$ may be estimated as:

$$\delta z_d = \frac{3n\lambda_0}{NA^2} \tag{2.18}$$

2.7.2 Geometrical effects

Consider a particle with diameter d_p located on the optical axis of an imaging lens at a distance *z* away from the focal plane, as illustrated in Fig. 2-8. Following the notation of Fig. 2-8, the radius of the geometrical shadow r_{gs} cast by the particle onto the focal plane can be written as:

$$r_{gs} = \frac{d_p}{2} + z\tan\theta \tag{2.19}$$

Assuming that the out-of-focus distance z is small compared to the focal length of the imaging lens, the angle θ may be approximated as the half-angle of the collecting cone of light appearing in the definition of the numerical aperture *NA*.

The measurement depth is estimated by considering a distance z such that the intensity along the optical axis is reduced to 10% due to the spread of the geometrical shadow, i.e. the collection cone of the lens. Assuming uniform intensity within the geometrical shadow, this occurs when the area of the geometrical shadow cast onto the focal plane by the out-of-focus particle is 10 times larger than that of an in-focus particle, i.e.

$$\pi r_{gs}^2 = 10\pi\left(\frac{d_p}{2}\right)^2 \tag{2.20}$$

Substituting for r_{gs} from equation (2.19) yields:

$$0.1\left(\frac{d_p}{2}+z\tan\theta\right)^2=\left(\frac{d_p}{2}\right)^2 \tag{2.21}$$

Solving for $2z=\delta z_g$, i.e. the measurement depth due to geometrical effects, yields:

$$\delta z_g=\frac{2.16d_p}{\tan\theta} \tag{2.22}$$

The above analysis assumes that the geometrical particle image is sufficiently resolved by the CCD array. In situations where the pixel size is much larger than the particle diameter d_p, a different expression for δz_g is achieved (Meinhart et al. 2000a). In most micro-PIV experiments, however, d_p is chosen such that the particles are sufficiently resolved by the CCD pixels. Therefore, the analysis of geometrical effects occurring when the particle size is smaller than the pixel size is not pursued here.

2.7.3 Total measurement depth

An estimate for the total measurement depth of a micro-PIV system is achieved by adding the effects of diffraction and those of geometrical optics. Furthermore, the finite size of the particles must be taken into consideration. The total measurement depth δz_m is thus:

$$\delta z_m=\delta z_d+\delta z_g+d_p \tag{2.23}$$

Substituting for δz_m and δz_g from equations (2.18) and (2.22), respectively, results in the following estimate for the measurement depth (Meinhart et al. 2000):

$$\delta z_m=\frac{3n\lambda}{NA^2}+\frac{2.16d_p}{\tan\theta}+d_p \tag{2.24}$$

2.8 Data interrogation in micro-PIV

In standard PIV, the particle images are subdivided into a fine mesh (interrogation windows), where each individual region is analyzed by means of correlation schemes, and a velocity vector field is calculated from a single image pair (or double-exposed image). In micro-PIV, however, the relatively low particle concentration necessary in order to overcome issues connected to background noise, the amount of particles in a single image pair is often very low (low image density).

This requires the use of either:

1) Large interrogation windows enclosing enough particles to obtain good correlation using standard cross-correlation schemes, thus seriously limiting the spatial (in-plane) resolution of the system, or

2) Interrogation windows of size such that acceptable level of spatial (in-plane) resolution is maintained, at the cost of the number of particles in each individual window. The latter approach does generally generate an erroneous vector field due to lack of correlation and high noise levels in the images (Wereley et al., 2002). In order to overcome this limitation, special interrogation techniques, or image processing before performing interrogation, are commonly applied in micro-PIV.

2.8.1 Average correlation

The cross-correlation function at a certain interrogation window of size of $p \times q$ pixels may be represented as (Wereley et al. 2002):

$$\Phi(x,y) = \sum_{j=1}^{q}\sum_{i=1}^{p} f(i,j) \cdot g(i+x, j+y) \quad , \tag{2.25}$$

where $f(i,j)$ and $g(i,j)$ are the grey-level distributions of the first and second exposures, respectively, and $\Phi(x,y)$ is the value of the correlation function for a displacement vector of $\delta s = (x,y)$ (Fig. 2-9). For a single, well seeded image pair without exceeding noise levels, the correlation function Φ has a distinct maximum peak corresponding to the particle displacement of (x,y) in the interrogation window.

Also, a number of substantially lower sub peaks, resulting from noise and mismatch of

the particle images, exist randomly scattered in the correlation plane.

In micro-PIV, however, when the number of particles contained within the interrogation window is insufficient, or the noise levels become too high, the peak representing the true particle displacement may become smaller than some of the sub peaks. This results in the generation of an erroneous velocity vector. For laminar, stationary flows, the velocity field is independent of time, so that the position of the correlation peak corresponding to the true particle displacement does not change for PIV recordings sampled at different times. The random sub peaks appear at varying positions and intensities in the different image pairs. By acquiring a large number of image pairs, calculating their individual correlation functions, and then ensemble averaging the correlation functions for corresponding interrogation windows in the individual PIV recordings, the true displacement peak remains in the same position, while the randomly scattered sub peaks average to zero. The average (or ensemble) correlation function may be written as (Meinhart et al. 2000b):

$$\Phi_{average}(x,y) = \frac{1}{N}\sum_{k=1}^{N}\Phi_k(x,y) \quad , \tag{2.26}$$

where $\Phi_k(x,y)$ is the k^{th} PIV recording pair, and N is the total number of recordings.

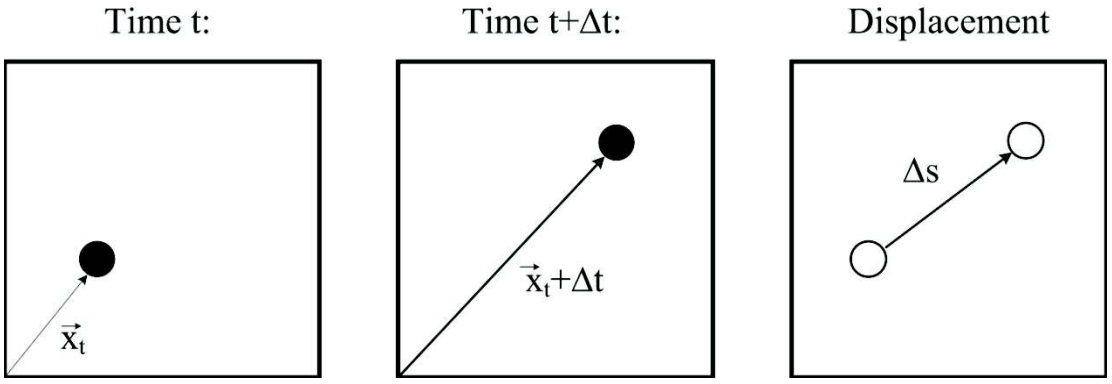

Figure 2-1 Left frame (particle position at time *t*); Center frame (particle position at time *t* + *Δt*); Right frame (displacement vector *Δs*).

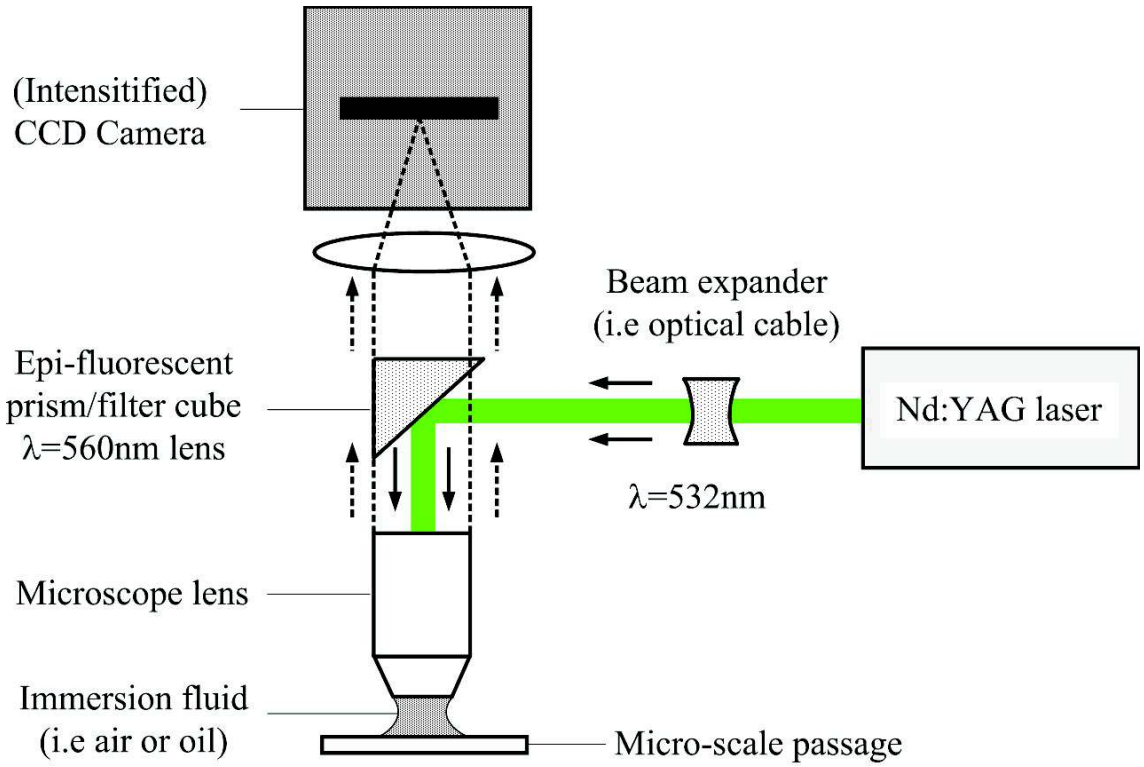

Figure 2-2 Schematics of a typical micro-PIV system. A pulsed Nd:YAG laser is used and a cooled CCD camera is used to record the particle images.

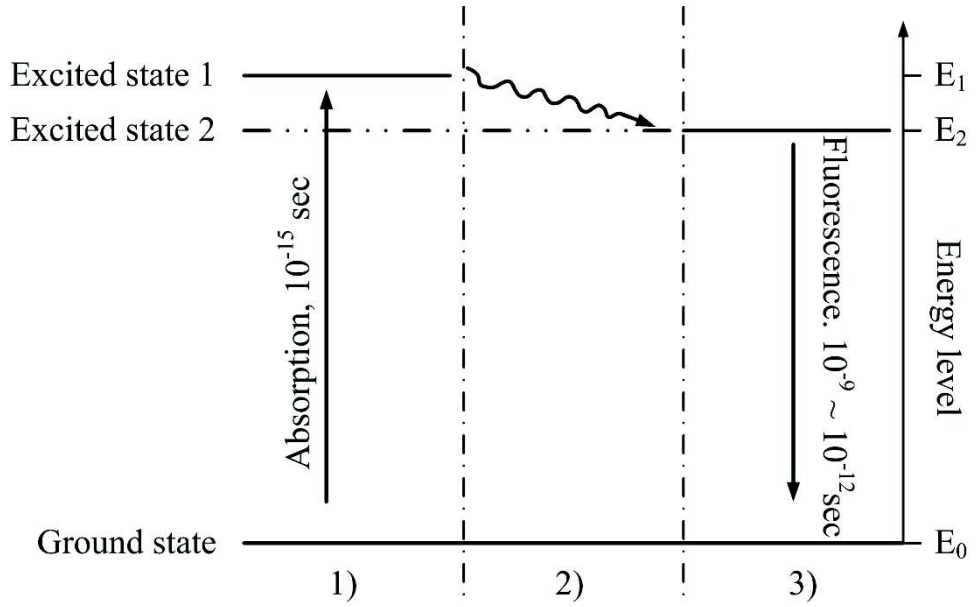

Figure 2-3 Principle of fluorescence. (1) A fluorochrome is excited by a photon to an energy level higher than the ground state (Excited state 1). (2) The excited electron loses energy due to interactions with the environment, thereby falling to a relaxed excited state (Excited state 2). (3) The electron collapses back to its ground state emitting a photon with energy corresponding to the difference between excited state 2 and ground state.

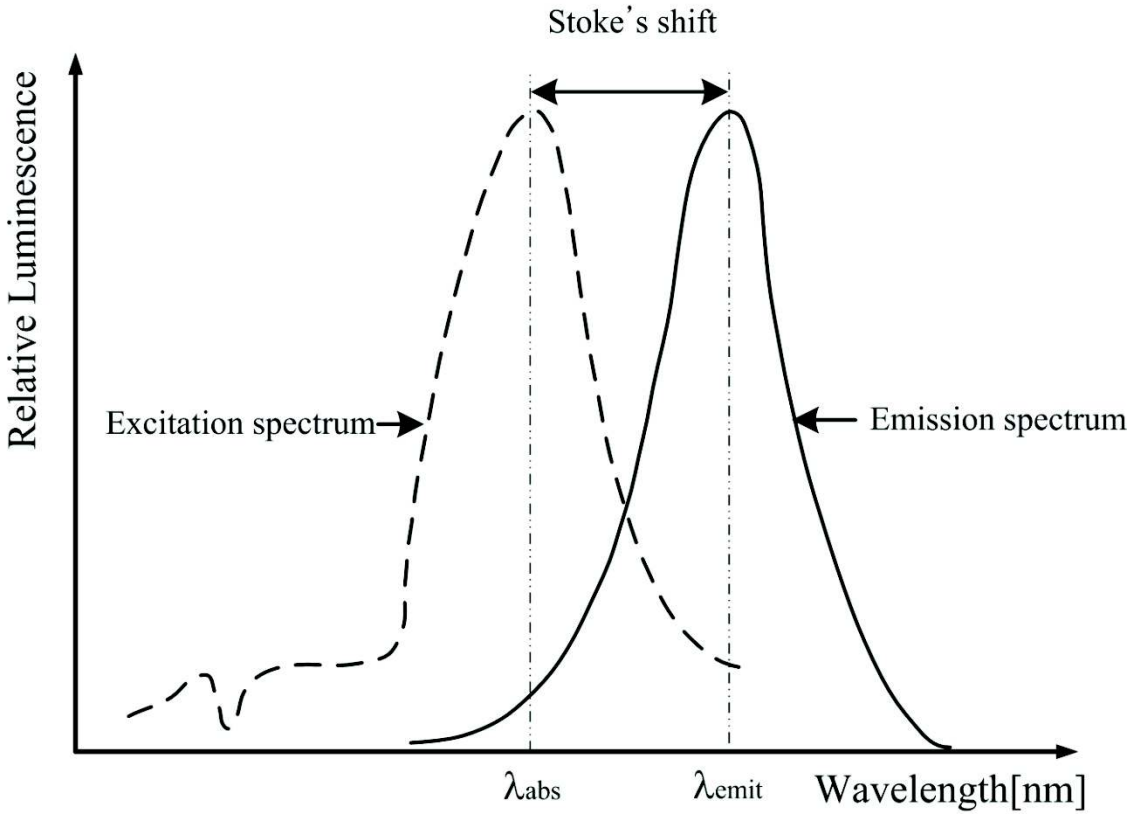

Figure 2-4 Illustration of excitation and emission spectra of a fluorochrome with corresponding Stokes' shift. Generally, several excitation and emission peaks may exist.

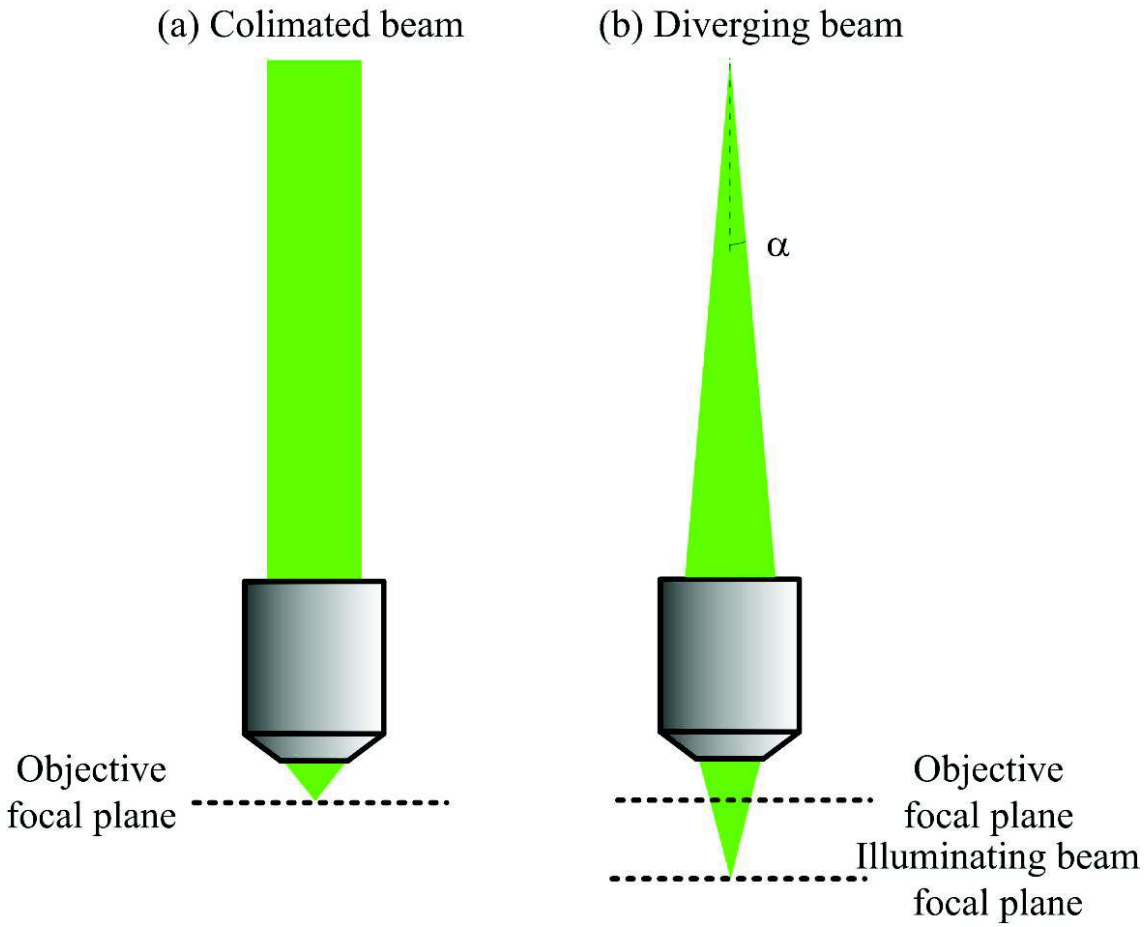

Figure 2-5 (a) Illumination by a collimated beam of light. The objective focal plane and beam focal plane overlap. No field illumination achieved. (b) Illumination by a diverging beam of light. The focal plane of the illuminating beam is shifted to a plane further away from the objective, resulting in field illumination of the objective's focal plane.

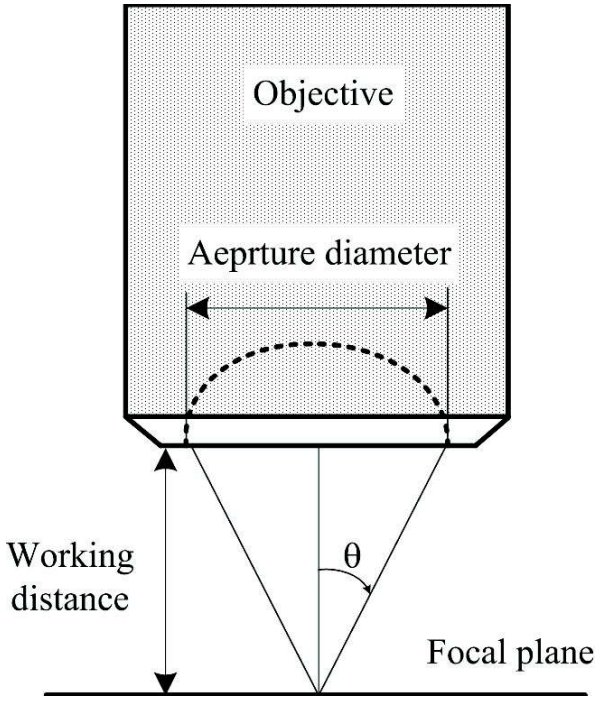

Figure 2-6 Light collecting cone half-angle θ, aperture diameter and working distance of a microscope objective.

Table. 2-1 Image brightness B_{epi} for objectives of different magnification and NA (Mitutoyo's objective lens)

Objective	Magnification	NA	B_{epi}
M Plan Apo	5×	0.14	0.15
M Plan Apo	10×	0.28	0.61
M Plan Apo	20×	0.42	0.78
M Plan Apo HR	10×	0.42	3.11
M Plan Apo HR	50×	0.75	1.27

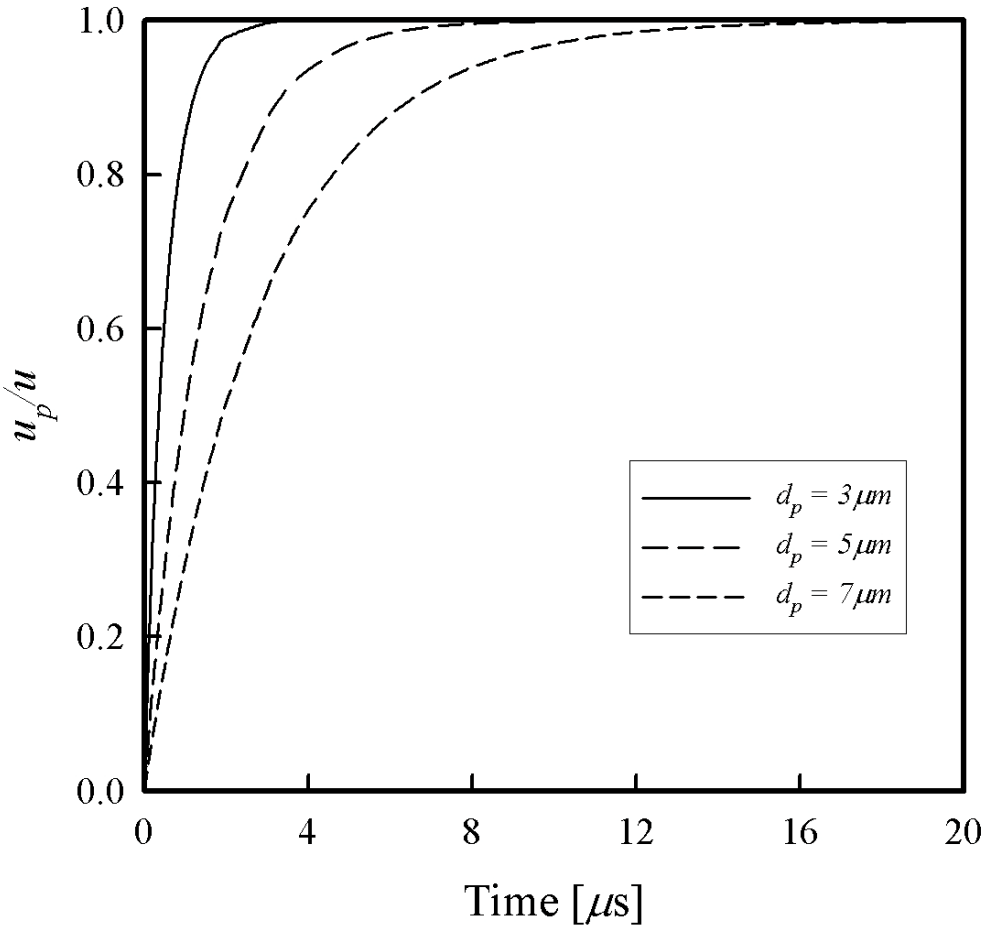

Figure 2-7 Particle response time to fluid acceleration for three different particle diameter; d_p=3μm, 5μm, and 7μm.

.

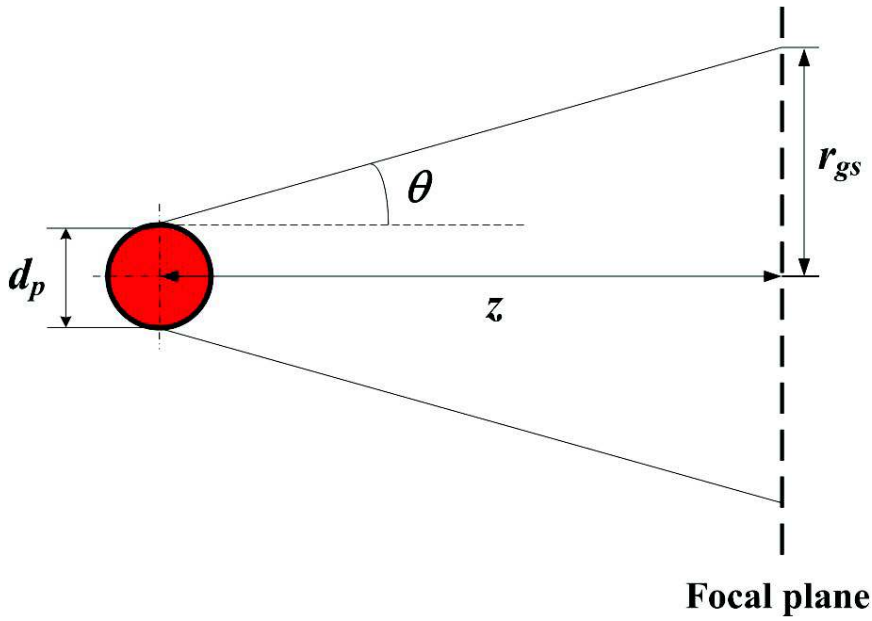

Figure 2-8 Geometrical shadow cast by an out-of-focus particle onto the focal plane. d_p is the particle diameter, z is the distance between the particle and the focal plane, θ is the collection angle of the imaging lens, and r_{gs} is the radius of the geometrical shadow.

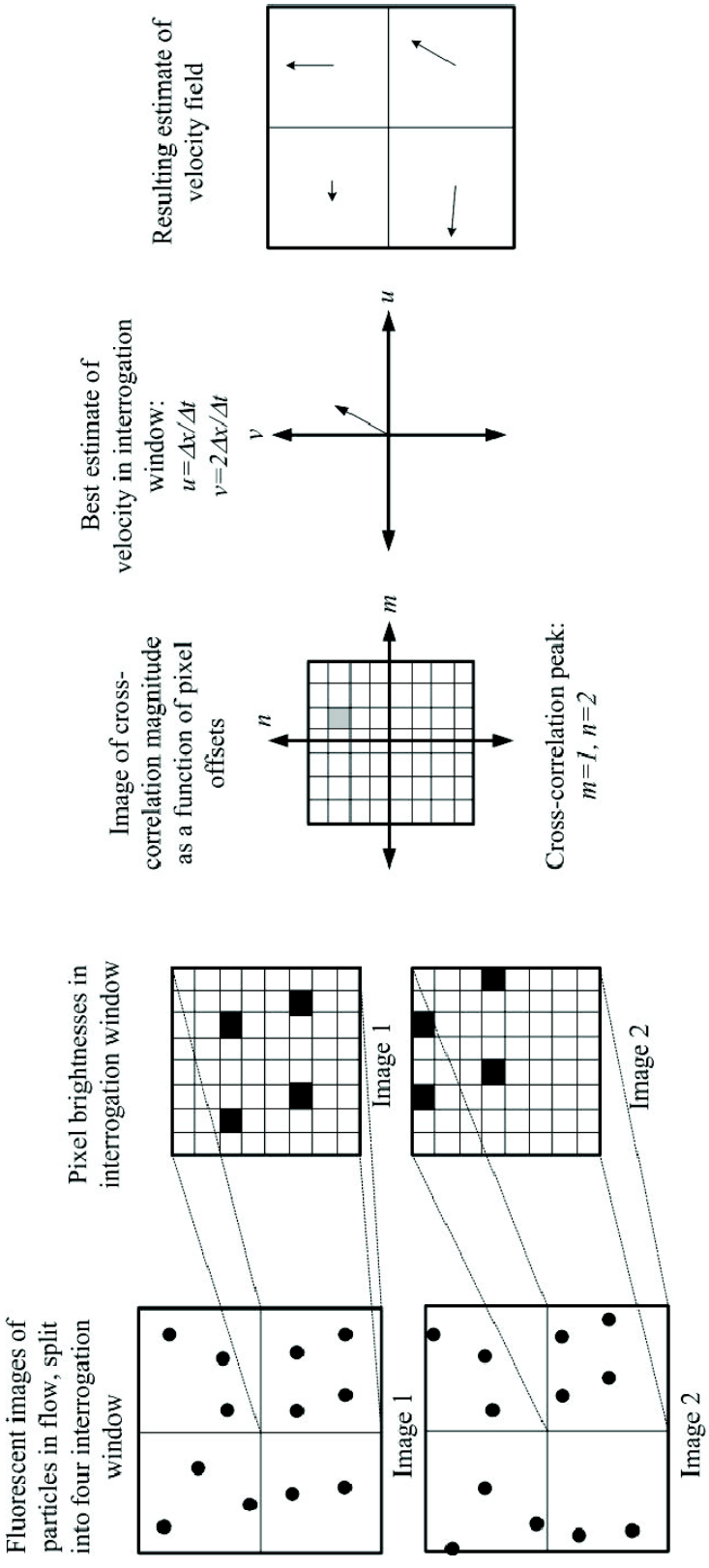

Figure 2-9 A cross-correlation algorithm for micro-PIV.

Chapter 3. Numerical analysis

3.1 The continuum hypothesis

In the macroscopic perspective of fluid mechanics, the flow can be assumed to satisfy the continuum hypothesis, that is, the flowing medium can be treated as continuous and indefinitely divisible, and the molecular structure of the fluid is not taken into account. This approach is valid for fluids where the local properties such as density and velocity can be described as average quantities over elements that are large compared to the molecular structure of the fluid, yet small enough compared to the macroscopic phenomena to permit the use of differential calculus to describe them.

For gases, the conditions for the continuum hypothesis may be investigated by considering the Knudsen number, which relates the mean free path λ of the gas molecules to the characteristic flow dimension L:

$$Kn = \frac{\lambda}{L} \tag{3.1}$$

Various flow regimes may be identified regarding the magnitude of Kn, where the continuum hypothesis with no-slip conditions is valid for $Kn < 10^{-3}$. Above this limit, non-equilibrium effects may begin to occur, but the continuum model modified by slip boundary conditions may be used in the range of $10^{-3} < Kn < 10^{-1}$. For increasing Kn, the continuum model is no longer valid, and a molecular approach is needed.

In liquids, where the molecules are not unbound and the concept of mean free path is not defined, the lattice spacing δ may be used as a similar measure.

$$\delta \sim \left(\frac{\bar{V}}{N_A} \right)^{1/3} \tag{3.2}$$

Where $\bar{V}$ is the molar volume (i.e. ratio of the volume of the substance to the number

of molecules (in moles) contained within that volume) and N_A is Avogadro's number ($N_A = 6.022 \times 10^{23} mol^{-1}$). This expression assumes a cubic lattice with touching molecules. For water, with a molecular mass of $M = 18.02 \times 10^{-3} kg \cdot mol^{-1}$ and a density of approximately $\rho = 10^3 kg \cdot m^{-3}$, the molar volume is $\bar{V} \approx 2 \times 10^{-5} m^3 \cdot mol^{-1}$, resulting in a lattice spacing of $\delta \approx 0.3 nm$.

Substituting λ by δ in equation (3.1), and solving for the characteristic length,

$$L = \frac{\delta}{Kn} \tag{3.3}$$

Requiring $Kn < 10^{-1}$, the continuum hypothesis is valid for channels with diameter in the range of $L > 3 nm$, and for the no-slip boundary condition to be valid, $L > 300\ nm$. Hence, the continuum model should yield valid description of liquid flow in geometries with dimensions even below $1 \mu m$, and thus be applicable to flows encountered in typical micro-scale passage.

3.2 Numerical analysis

3.2.1 Governing equation

The mass conservation equation of steady state in cylindrical coordinate is given by equation (3.4):

$$\frac{1}{r}\frac{\partial}{\partial r}(r v_r) + \frac{1}{r}\frac{\partial v_\theta}{\partial \theta} + \frac{\partial v_z}{\partial z} = 0 \tag{3.4}$$

The momentum conservation equations of steady state in cylindrical coordinate are expressed by equation (3.5) to (3.7);

(1) r component

$$\begin{aligned} & v_r \frac{\partial v_r}{\partial r} + \frac{v_\theta}{r}\frac{\partial v_\theta}{\partial \theta} - \frac{v_\theta^2}{r} + v_z \frac{\partial v_r}{\partial z} \\ & = g_r - \frac{1}{\rho}\frac{\partial p}{\partial r} + \nu\left\{\frac{\partial}{\partial r}\left(\frac{1}{r}\frac{\partial (r v_r)}{\partial r}\right) + \frac{1}{r^2}\frac{\partial^2 v_r}{\partial \theta^2} - \frac{2}{r^2}\frac{\partial v_\theta}{\partial \theta} + \frac{\partial^2 v_r}{\partial r^2}\right\} \end{aligned} \tag{3.5}$$

(2) θ component

$$\begin{aligned} & v_r \frac{\partial v_\theta}{\partial r} + \frac{v_\theta}{r}\frac{\partial v_\theta}{\partial \theta} + \frac{v_r v_\theta}{r} + v_z \frac{\partial v_\theta}{\partial z} \\ & = g_\theta - \frac{1}{r\rho}\frac{\partial p}{\partial \theta} + \nu\left\{\frac{\partial}{\partial r}\left(\frac{1}{r}\frac{\partial (r v_\theta)}{\partial r}\right) + \frac{1}{r^2}\frac{\partial^2 v_\theta}{\partial \theta^2} + \frac{2}{r^2}\frac{\partial v_r}{\partial \theta} + \frac{\partial^2 v_\theta}{\partial z^2}\right\} \end{aligned} \tag{3.6}$$

(3) z component

$$\begin{aligned} & v_r \frac{\partial v_\theta}{\partial r} + \frac{v_\theta}{r}\frac{\partial v_\theta}{\partial \theta} + \frac{v_r v_\theta}{r} + v_z \frac{\partial v_\theta}{\partial z} \\ & = g_\theta - \frac{1}{r\rho}\frac{\partial p}{\partial \theta} + \nu\left\{\frac{\partial}{\partial r}\left(\frac{1}{r}\frac{\partial (r v_\theta)}{\partial r}\right) + \frac{1}{r^2}\frac{\partial^2 v_\theta}{\partial \theta^2} + \frac{2}{r^2}\frac{\partial v_r}{\partial \theta} + \frac{\partial^2 v_\theta}{\partial z^2}\right\} \end{aligned} \tag{3.7}$$

3.2.2 Numerical scheme

Overview process of the computational solution procedure is generally shown in Fig. 3-1. With followed by this procedure, the equations (3.5) to (3.7) are discretized and solve solves the three-dimensional, incompressible, laminar Navier-Stokes equations with based on a finite volume method using a commercial CFD software STAR-CD. The SIMPLE method is chosen for the pressure-velocity coupling and the algebraic multi-grid solver is used for the velocity and pressure corrections.

3.2.3 Steady-state flow calculation with SIMPLE

The control parameters available for SIMPLE are followed as below. A single corrector stage is always used and pressure is under-relaxed. The standard (default) settings in STAR-CD are given in Table 3-1 (STAR-CD user manual. 2009). These settings should result in near-monotonic decrease in the global residuals during the course of the calculations, depending on mesh density and other factors. If, thereafter, one or more of the global residuals do not fall, then remedial measures are necessary.

3.2.4 Computational domain, boundary condition, and grid system

All spatial discretizations are carried out by using the standard, second-order, central-difference scheme. The entire flow domain, shown in Fig. 3-2, which consists of the gap (H) between the disks and the annular region between the rotating disk and the housing, is discretized into a grid system having 3 million O-type hexahedral cells (see Fig. 3-3).

The calculations are done on a Pentium 2.4GHz, single processor machine. It took around 10 hours to complete the calculation for one rotational speed case.

As for the boundary conditions, all the solid surfaces, including that of the rotating disk, are assumed to have no-slip condition, especially the rotating disk includes also the rotational condition. Herein, the gap between stationary and rotating disks is changed in range from 100μm to 500μm. The convergence of the calculation is checked by monitoring if the residual error during the calculation has reached below 10^{-4}.

3.3 Results and discussion

3.3.1 Velocity magnitude contours

Figures 3-4, 3-5, and 3-6 show velocity magnitude contour at 300rpm, 500rpm, an 700rpm and at 100μm, 250μm, and 500μm. In Fig. 3-4 and 3-5, the velocity magnitude increases linearly with r. Near the disk edge, outward-vortical motion appears from the disk edge toward the side wall of the casing. In Fig. 3-6, Vortical motion is changed with increasing rotational speed near the disk edge compared with Fig. 3-4 and 3-5. It is due to flow separation near the rotating disk edge of the bottom of rotating disk.

After increasing the rotational speed more and more and if decreasing, such vortical motion is similar to Fig. 3-4 and Fig. 3-5. It can be seen that hysteresis phenomenon occurs as shown in Fig. 3-7.

3.3.2 Radial and tangential velocity profiles

Figures 3-8 to 3-10 represent the radial and tangential velocities (V_r and V_θ) for the rotational speeds of 100, 300, 500, 700rpm and H=100μm, 250μm, 500μm, respectively. The CFD results are plotted for z/H=0.2, 0.4, 0.6, and 0.8 where the velocities are non-dimensionalized by the tangential velocity of the disk edge, $R\omega$.

For all the rotational speeds and H, the tangential velocities increase almost linearly

with *r*, Near the disk edge, however, they start to either decrease or increase non-linearly, depending on the rotational speed.

The radial velocities are positive for *z/H*=0.2 and 0.4, while they become negative for *z/H*=0.6 and 0.8. The negative value indicates the presence of a secondary flow, consisting of an outward flow near the rotating disk and an inward flow near the stationary disk. These radial velocities increase with increasing *H* from 100μm to 500μm.

The secondary flow is presented in more detail in Fig. 3-11a-d, where the radial velocities are plotted as a function of *z/H* at *r/R*=0.20, 0.40, 0.60, and 0.88. The non-dimensionalized magnitude of the secondary flow increases with rotational speed and *H*, with a zero-crossing point at around z/H=0.48. The inward flow near the stationary disk is not desirable for the development of rotation-shearing chemical reactors, because it would hinder the reactant from flowing smoothly out of the reaction zone. The secondary flow affects the profile of the tangential velocities as shown in Fig. 3-12a-d where the tangential velocities are plotted as a function of *z/H*. While the profile is almost linear for H=100μm and all rotational number as in a laminar Couette flow, it starts to become non-linear for the 500rpm and 700rpm at *H*=500μm. The flow fields for these rotational speeds remain laminar.

Table 3-1 Standard control parameter settings for steady SIMPLE

Parameter	Variable				
	Velocity	Pressure	Turbulence	Enthalpy	Mass fraction
Solver tolerance	0.1	0.05	0.1	0.1	0.1
Sweep limit	100	1000	100	100	100
Relaxation	0.7	0.3	0.7	0.95	1.0

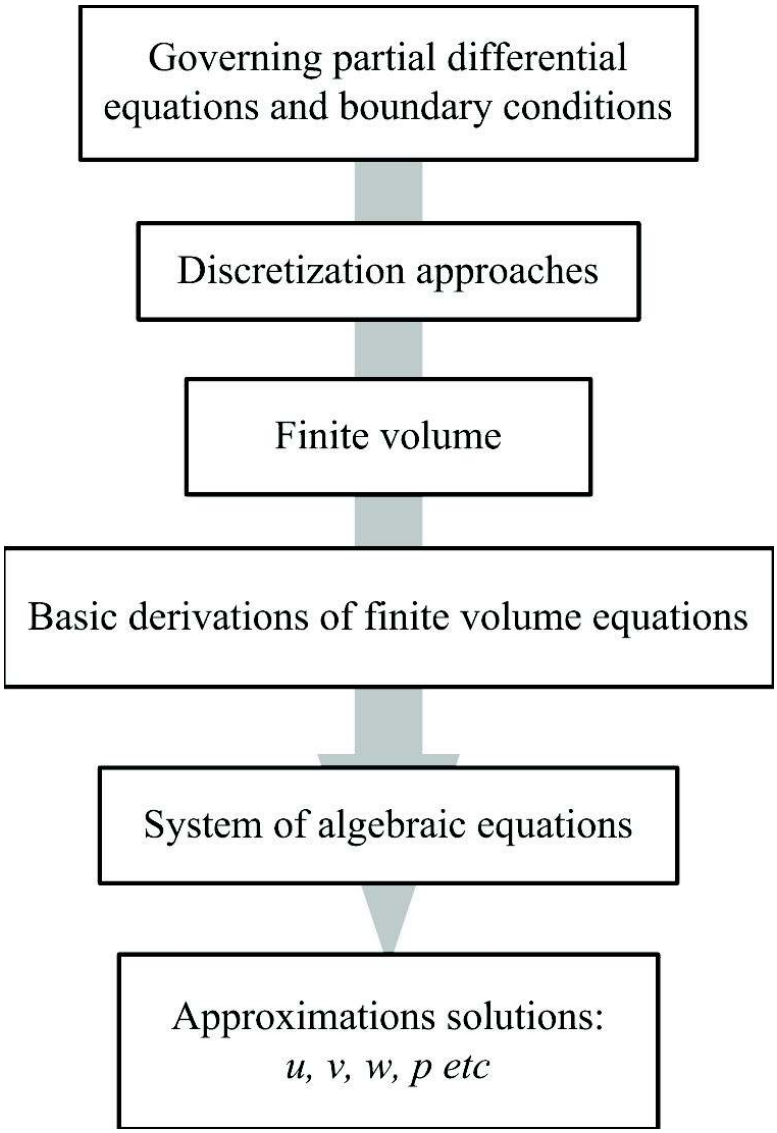

Figure 3-1 Overview process of the computational solution procedure.

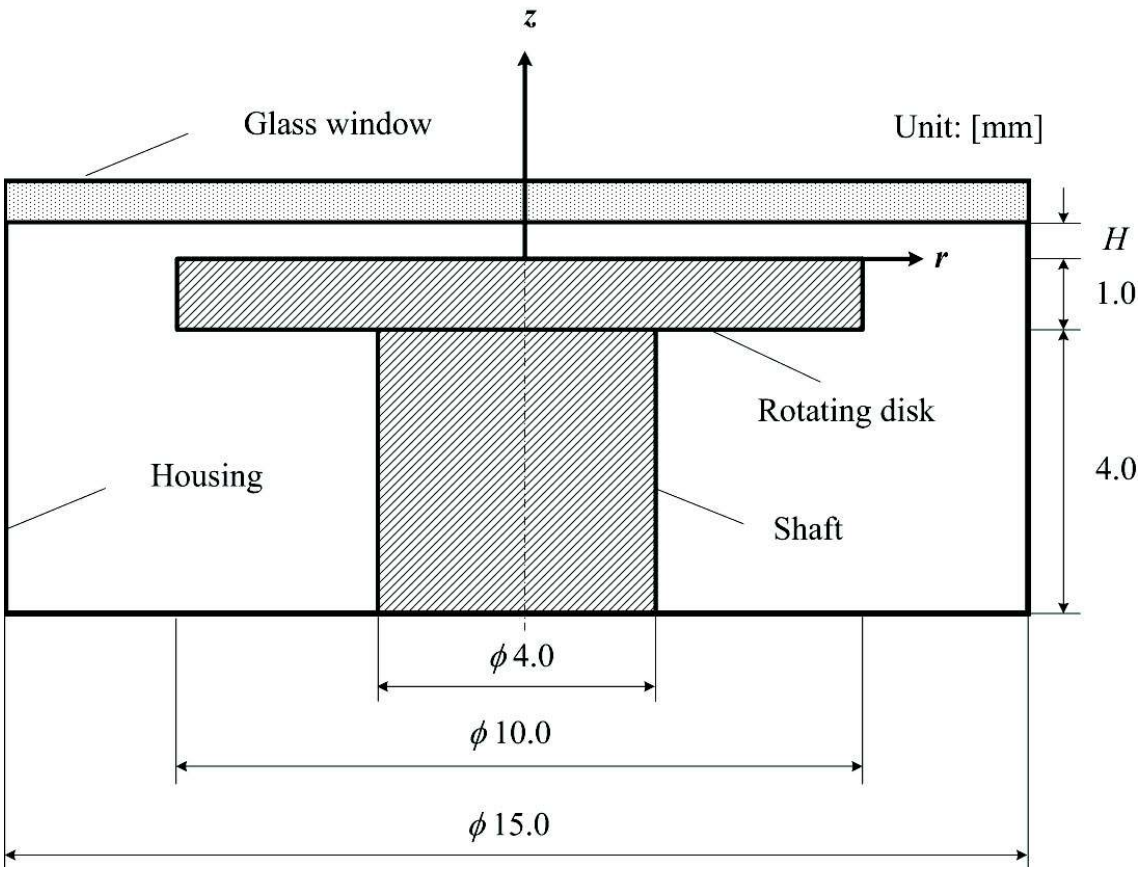

Figure 3-2 Computational domain.

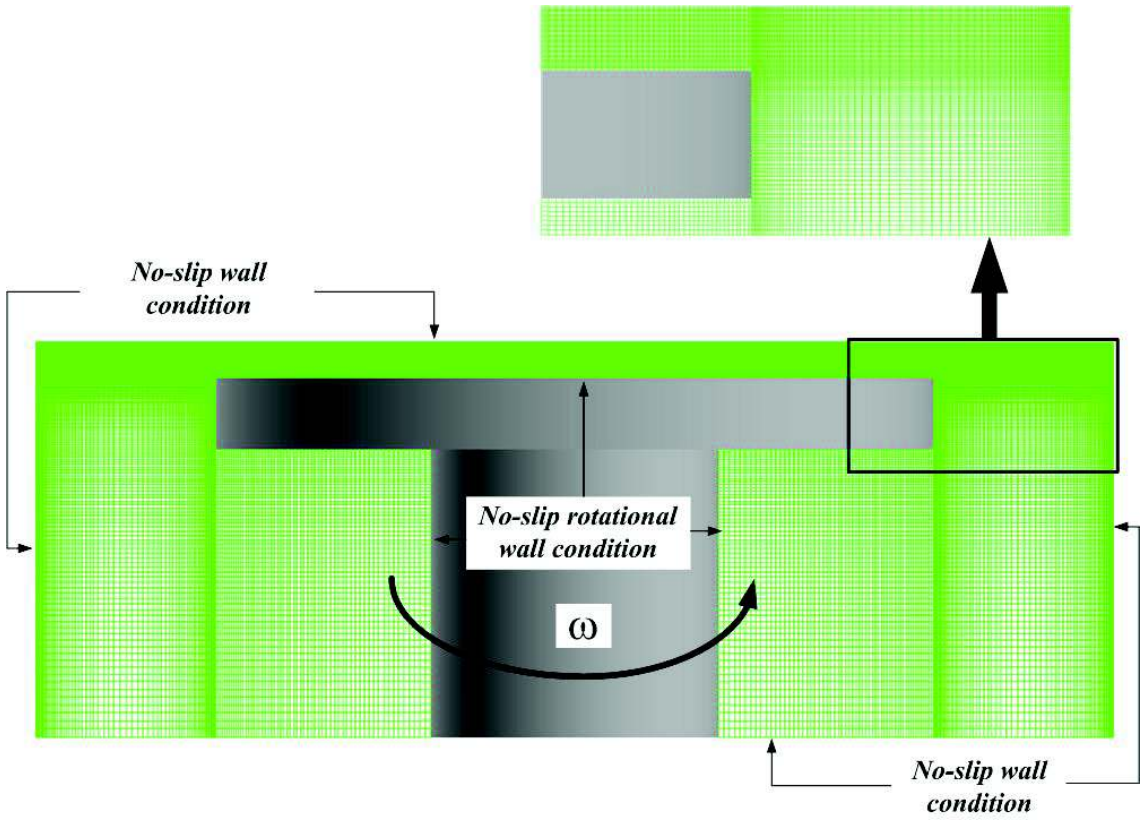

Figure 3-3 Computational grid and boundary conditions.

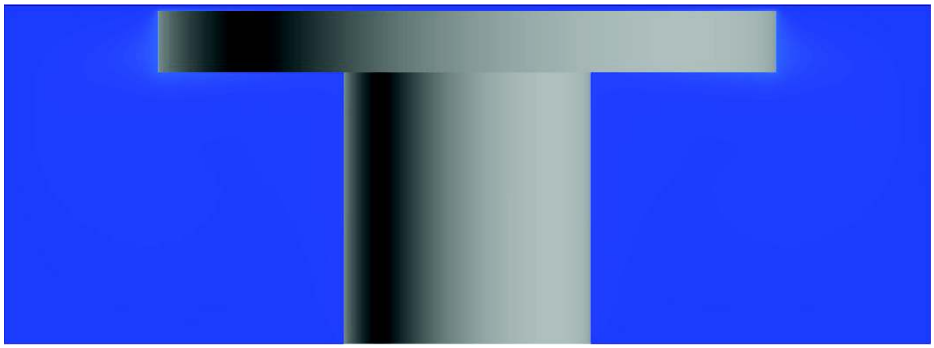

(a) 100rpm

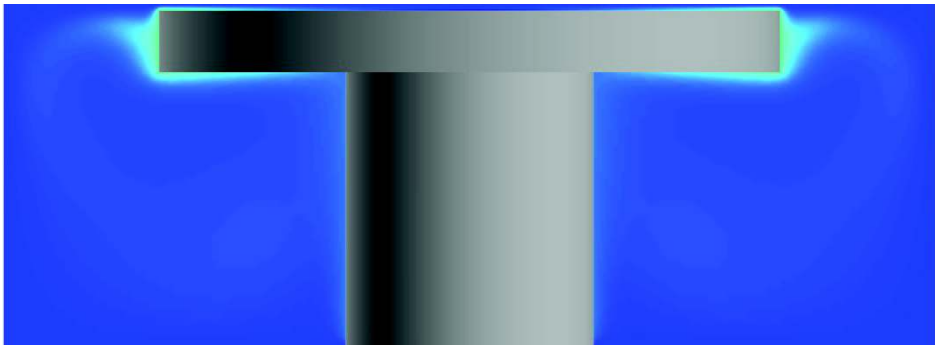

(b) 300rpm

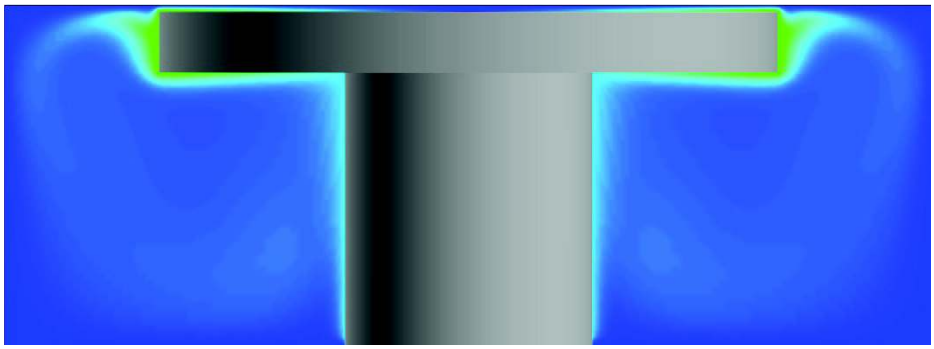

(c) 500rpm

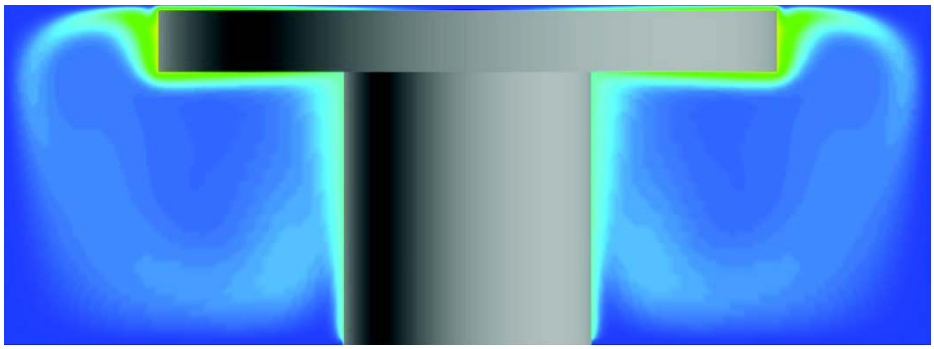

(d) 700rpm

Figure 3-4 Velocity magnitude contour for various rotational speed (H=100μm).

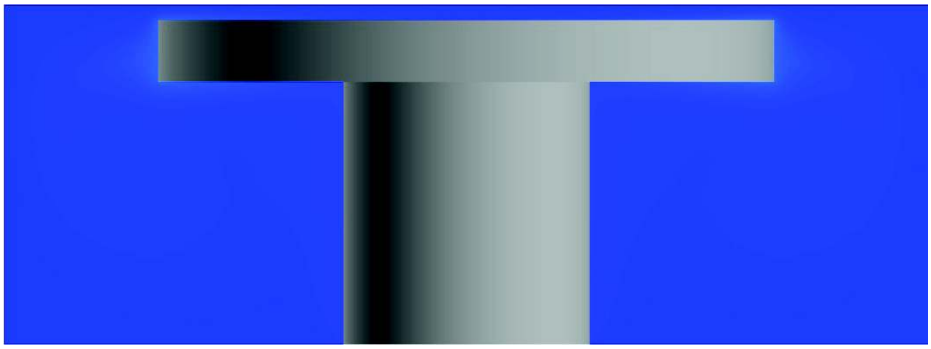

(a) 100rpm

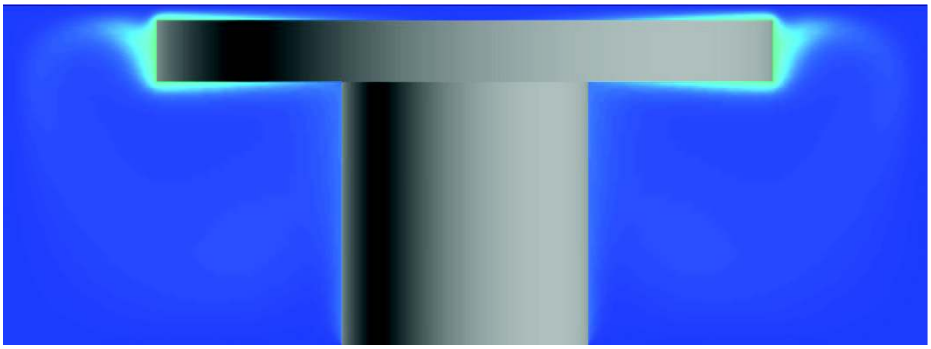

(b) 300rpm

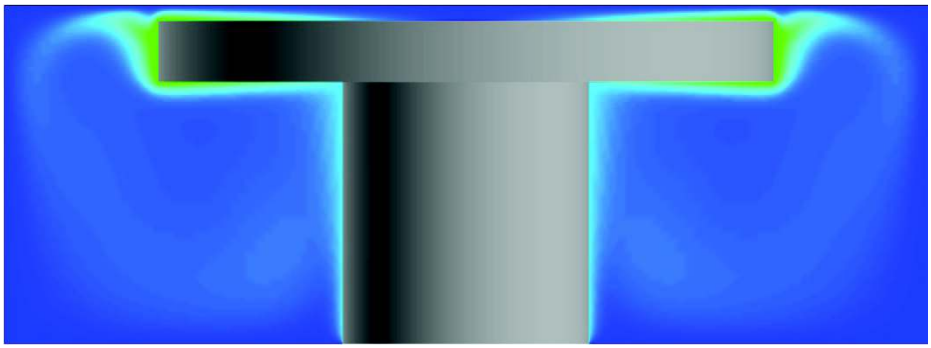

(c) 500rpm

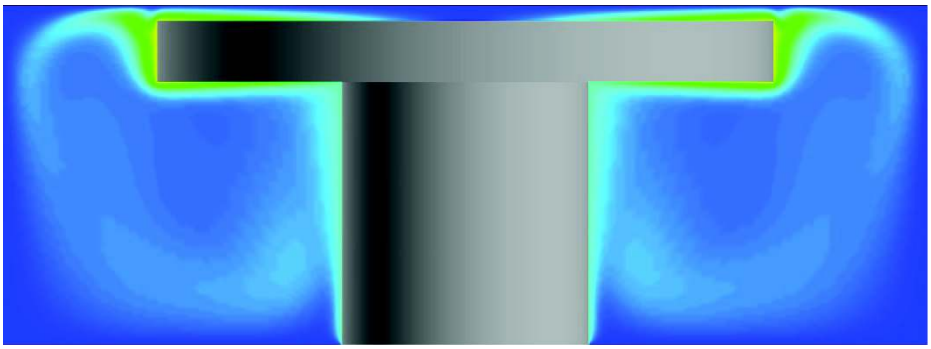

(d) 700rpm

Figure 3-5 Velocity magnitude contour for various rotational speed (H=250μm).

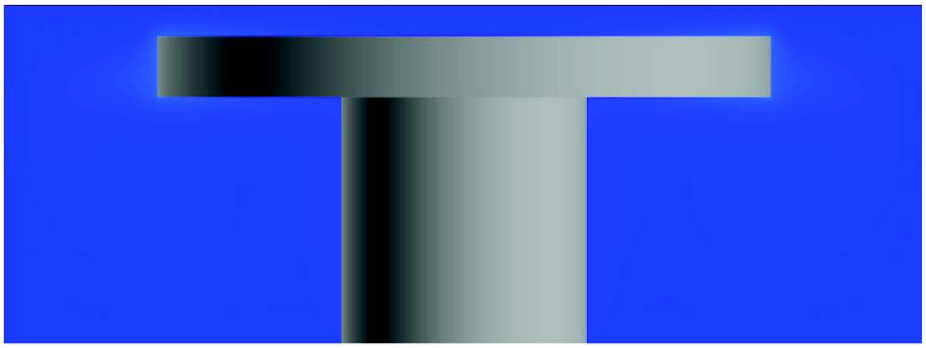

(a) 100rpm

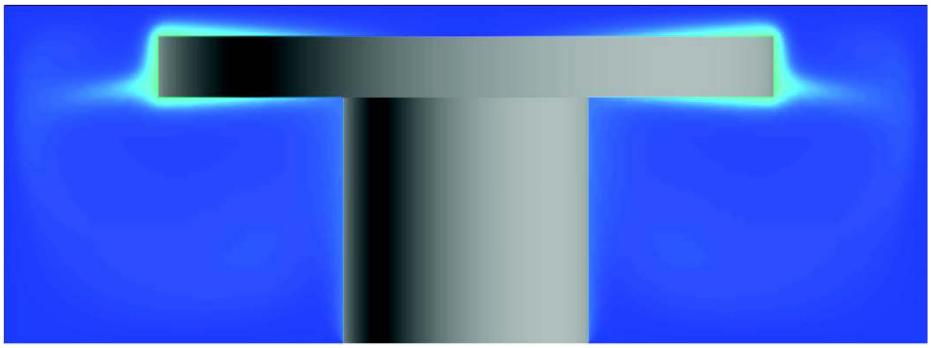

(b) 300rpm

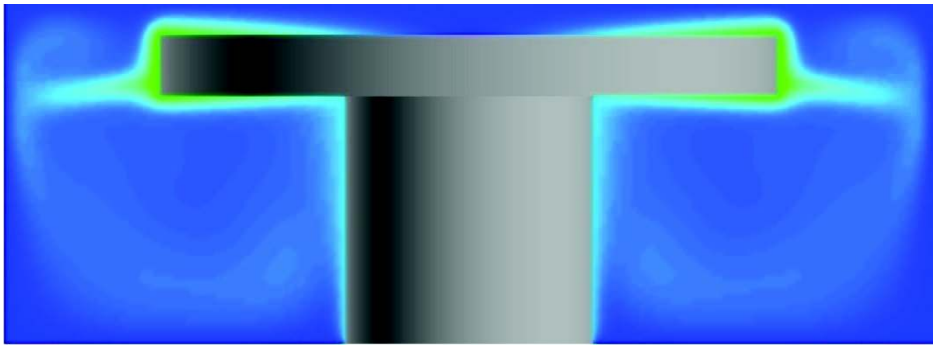

(c) 500rpm

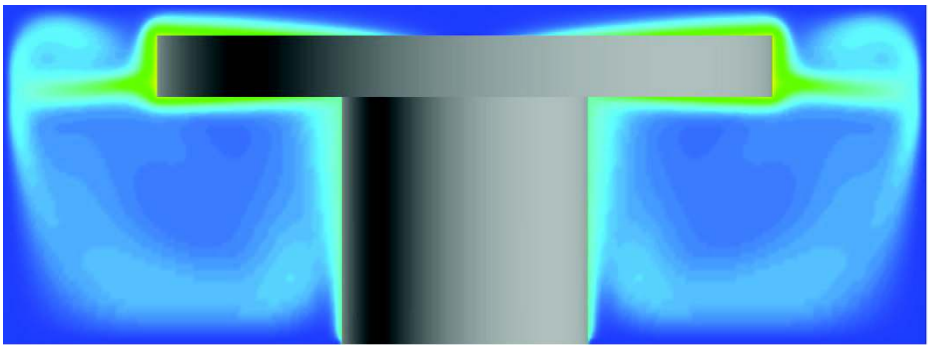

(d) 700rpm

Figure 3-6 Velocity magnitude contour for various rotational speed (H=500μm).

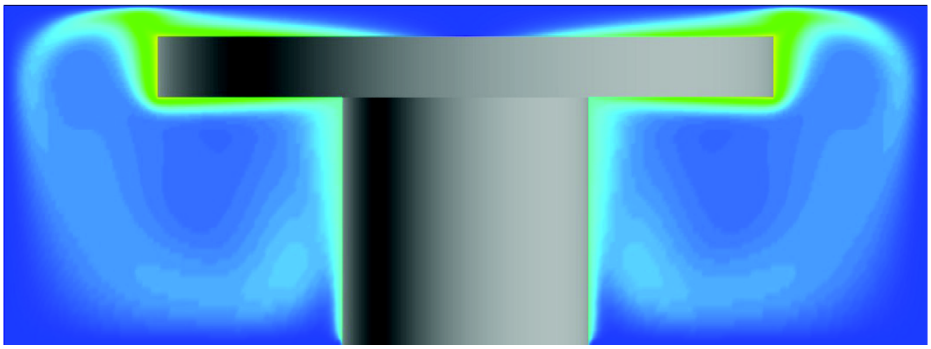

(a) 700rpm

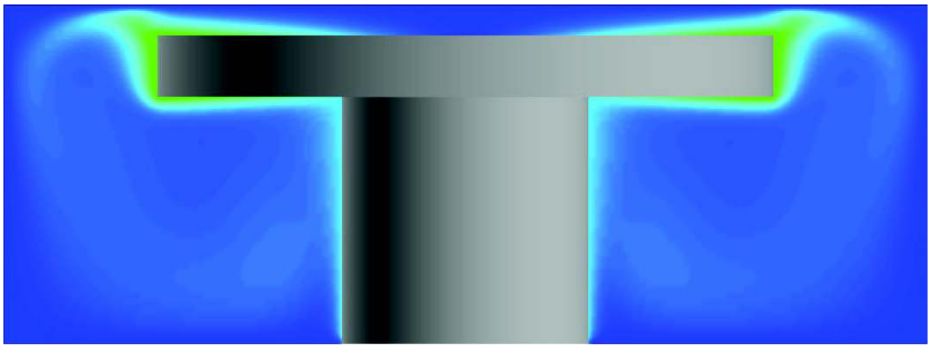

(b) 500rpm

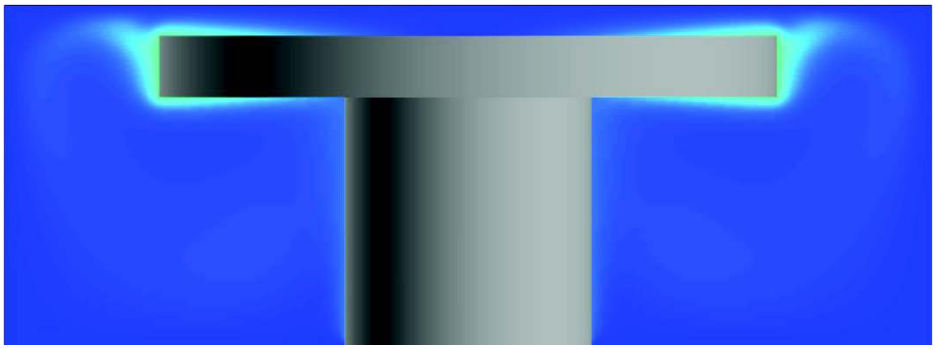

(c) 300rpm

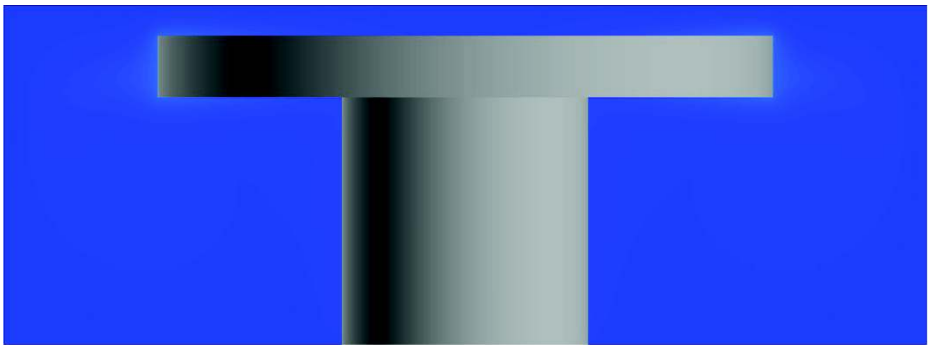

(d) 100rpm

Figure 3-7 Hysteresis phenomenon of edge vortex of rotating disk (H=500μm).

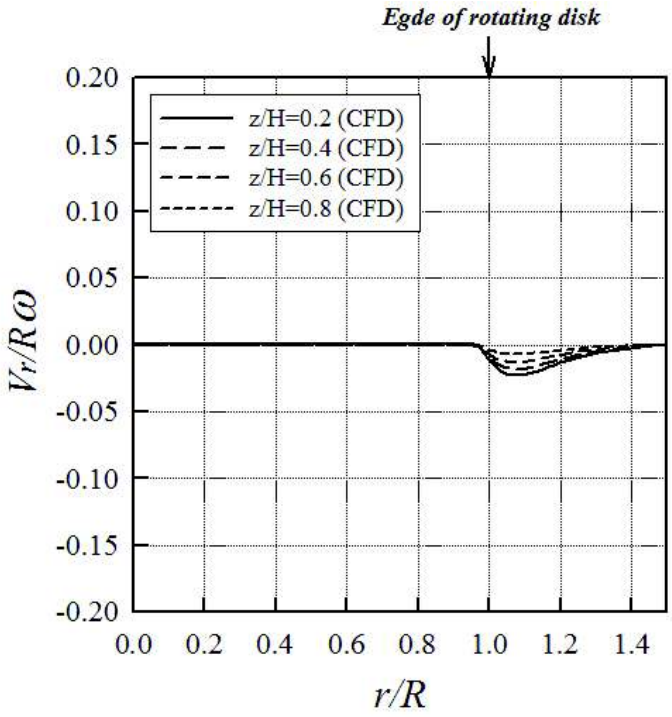

(a) Radial velocity

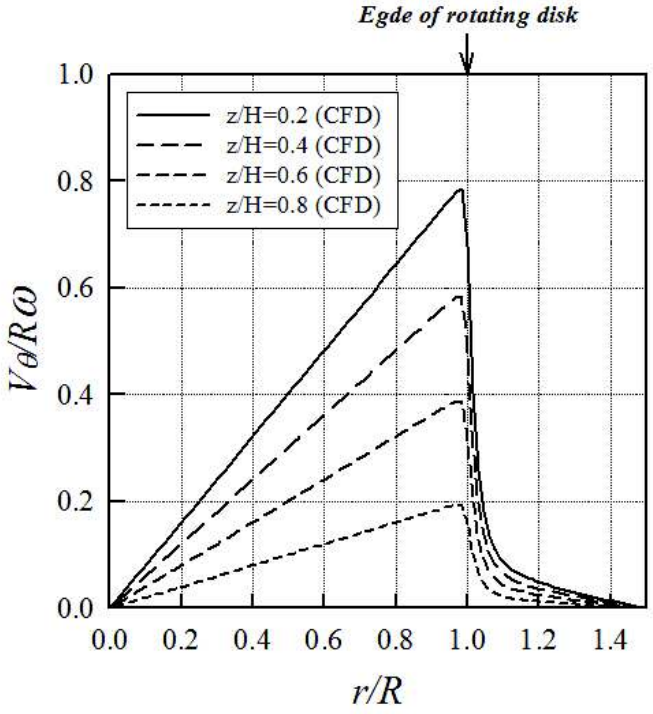

(b) Tangential velocity

Figure 3-8a Radial and tangential velocity profiles plotted as a function of r/R for rotational speeds of 100rpm (H=100μm).

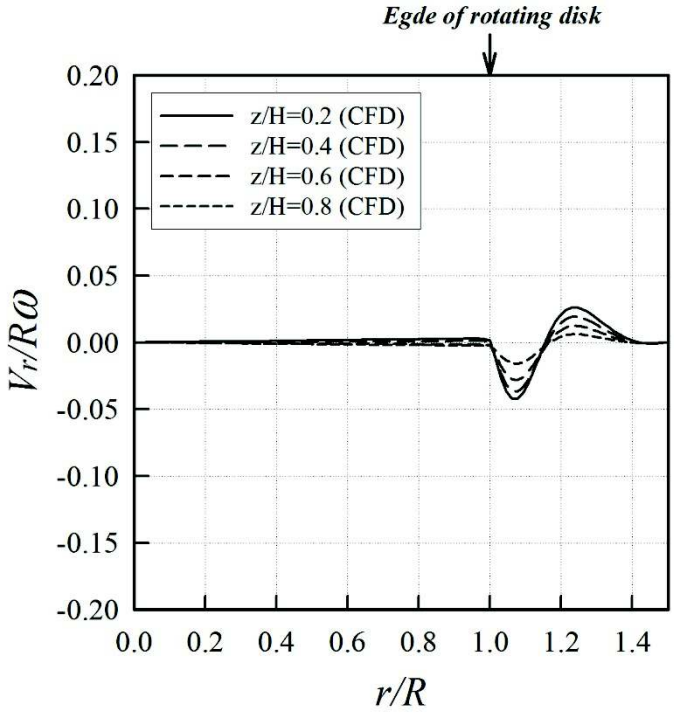

(a) Radial velocity

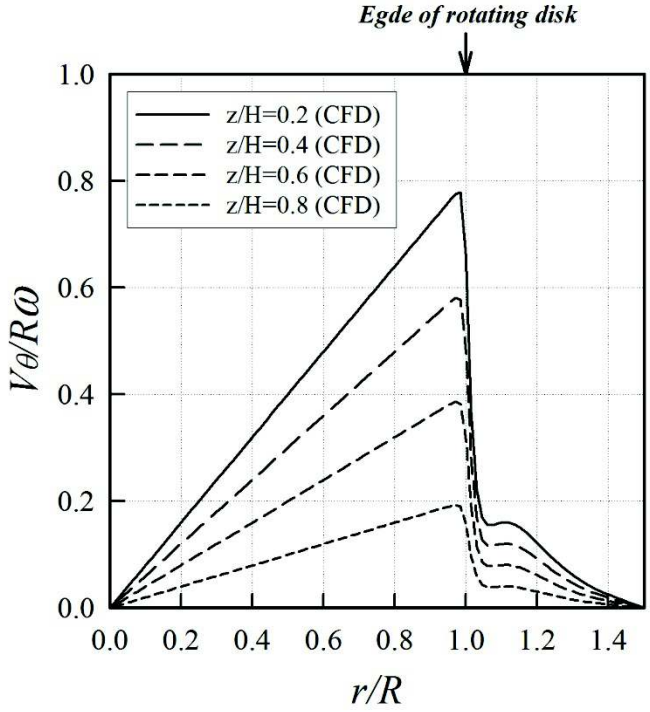

(b) Tangential velocity

Figure 3-8b Radial and tangential velocity profiles plotted as a function of r/R for rotational speeds of 300rpm (H=100μm).

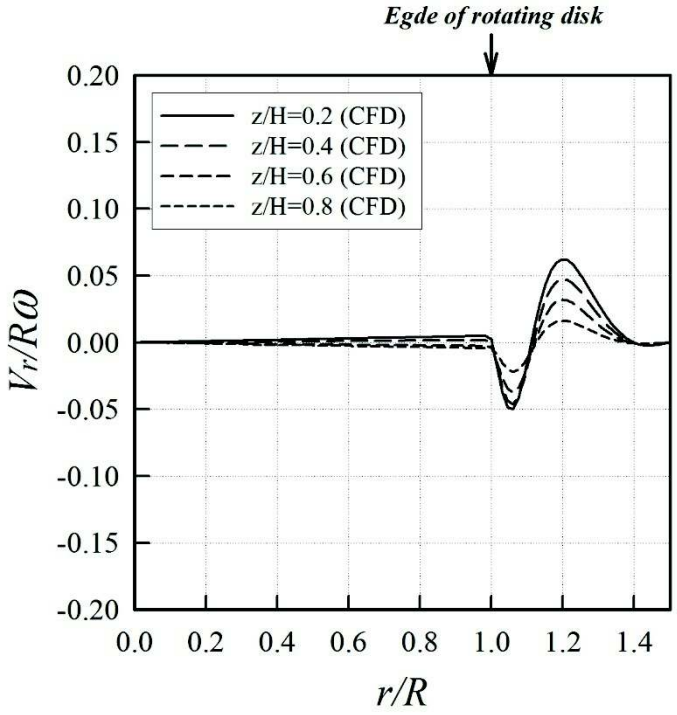

(a) Radial velocity

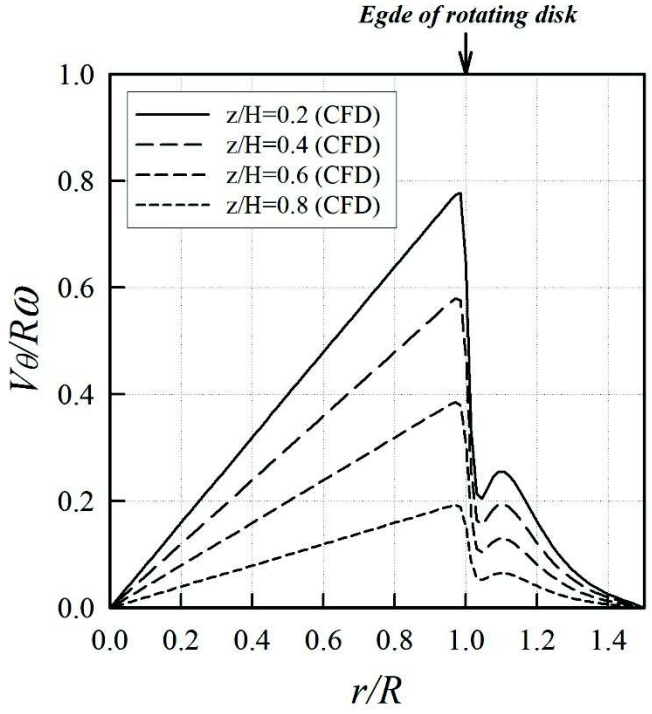

(b) Tangential velocity

Figure 3-8c Radial and tangential velocity profiles plotted as a function of r/R for rotational speeds of 500rpm (H=100μm).

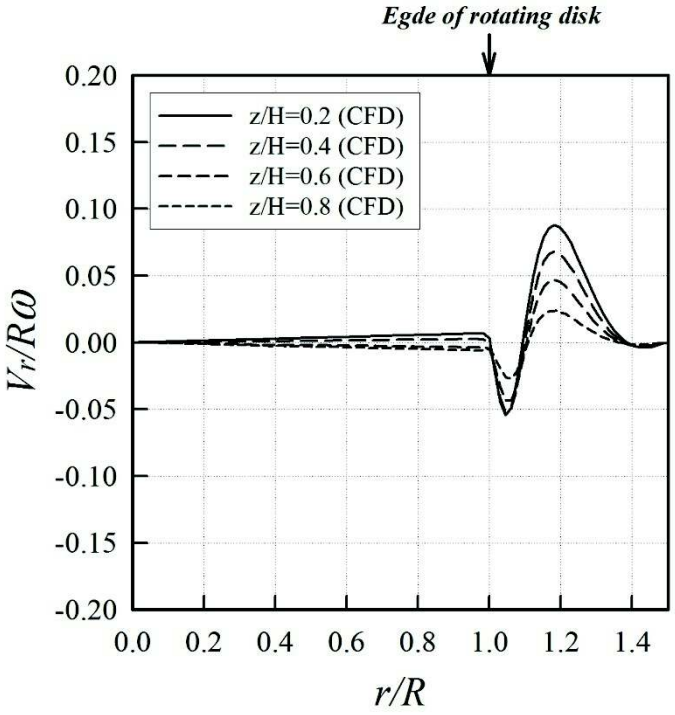

(a) Radial velocity

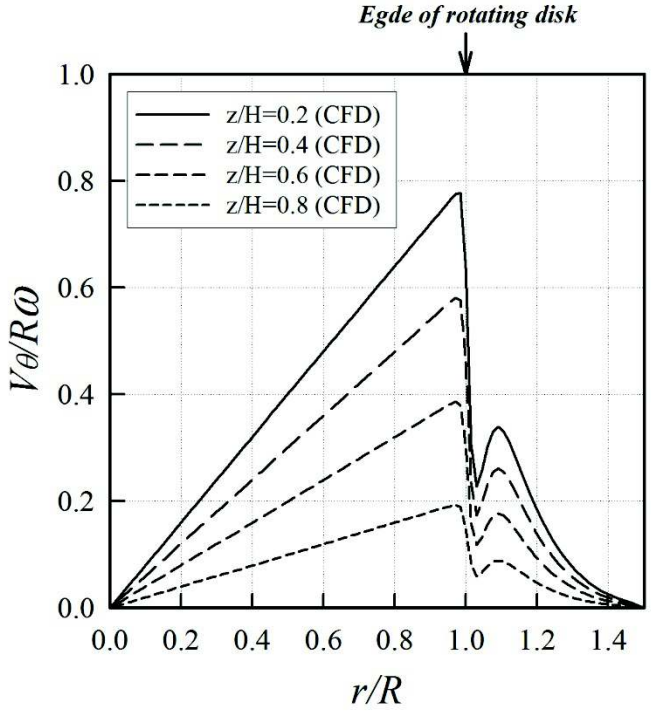

(b) Tangential velocity

Figure 3-8d Radial and tangential velocity profiles plotted as a function of r/R for rotational speeds of 700rpm (H=100μm).

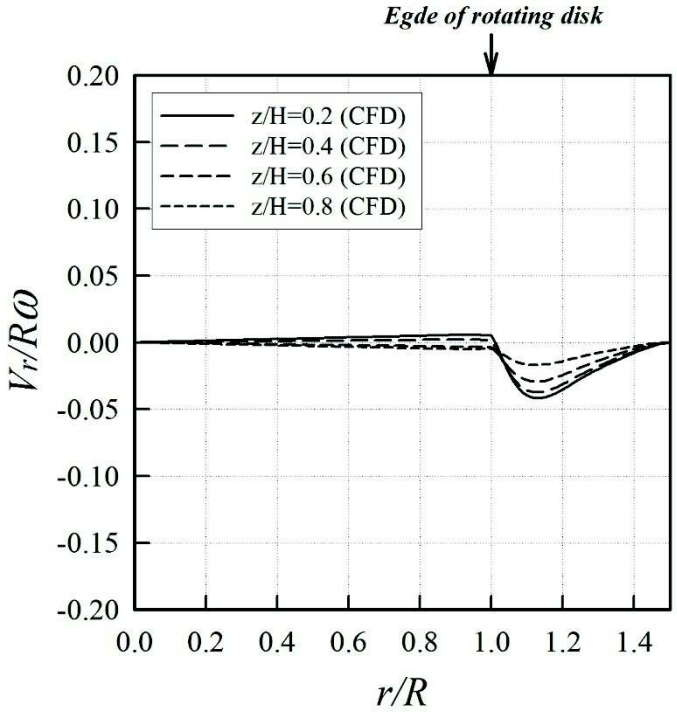

(a) Radial velocity

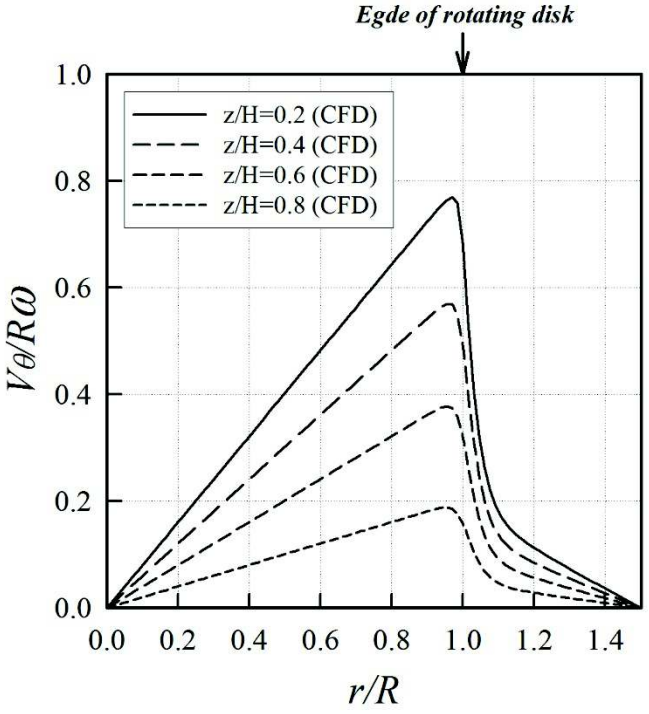

(b) Tangential velocity

Figure 3-9a Radial and tangential velocity profiles plotted as a function of r/R for rotational speeds of 100rpm (H=250μm).

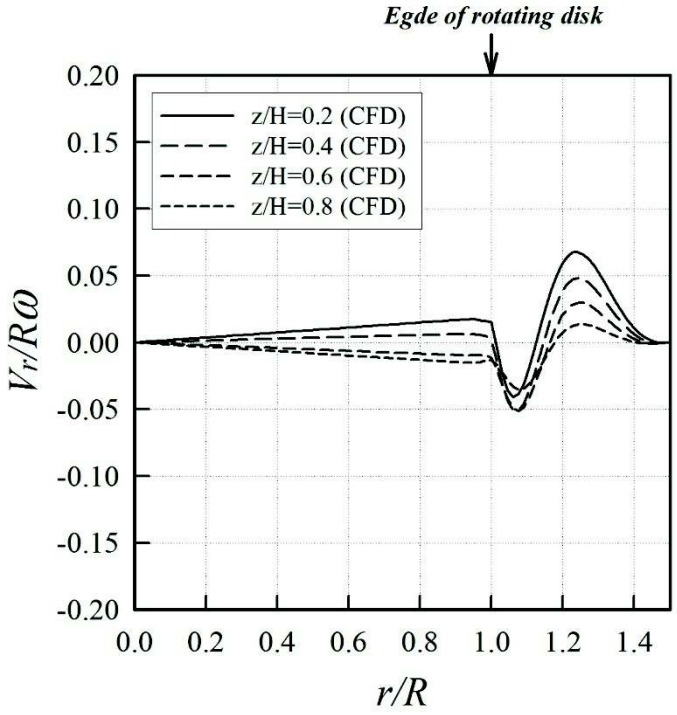

(a) Radial velocity

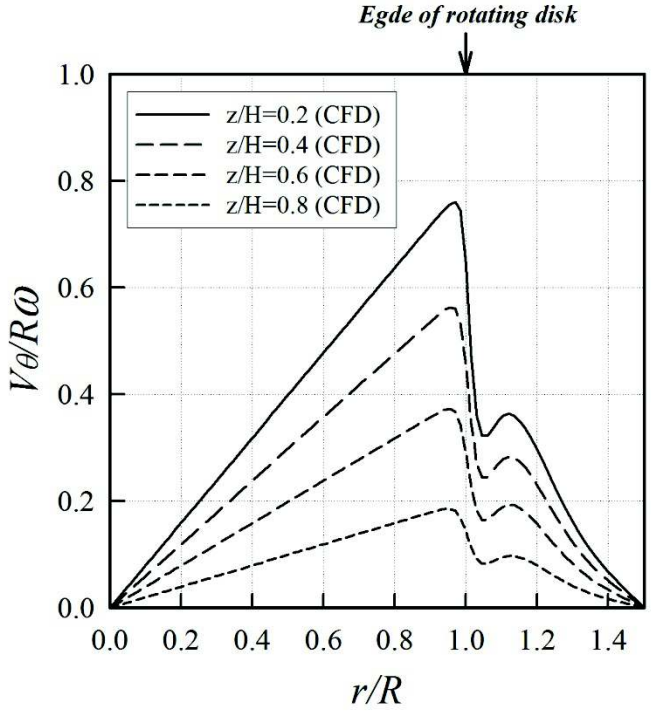

(b) Tangential velocity

Figure 3-9b Radial and tangential velocity profiles plotted as a function of r/R for rotational speeds of 300rpm (H=250μm).

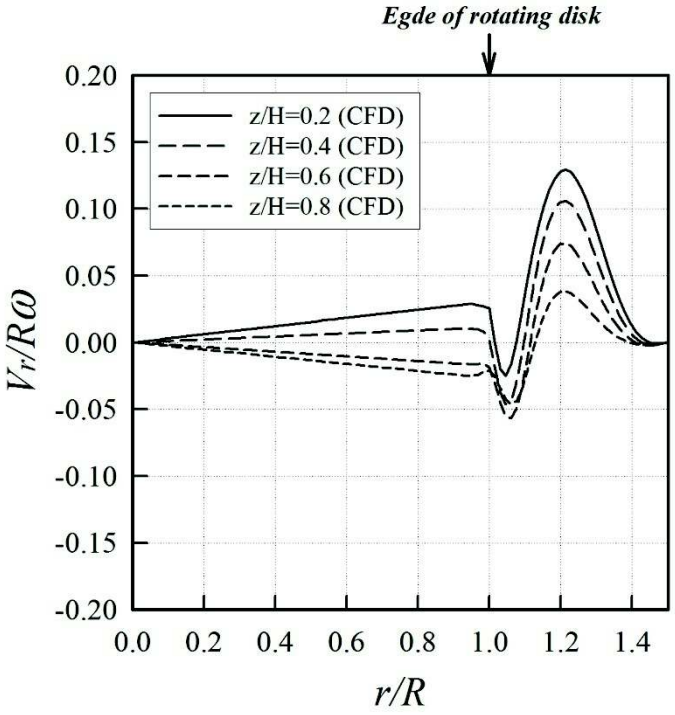

(a) Radial velocity

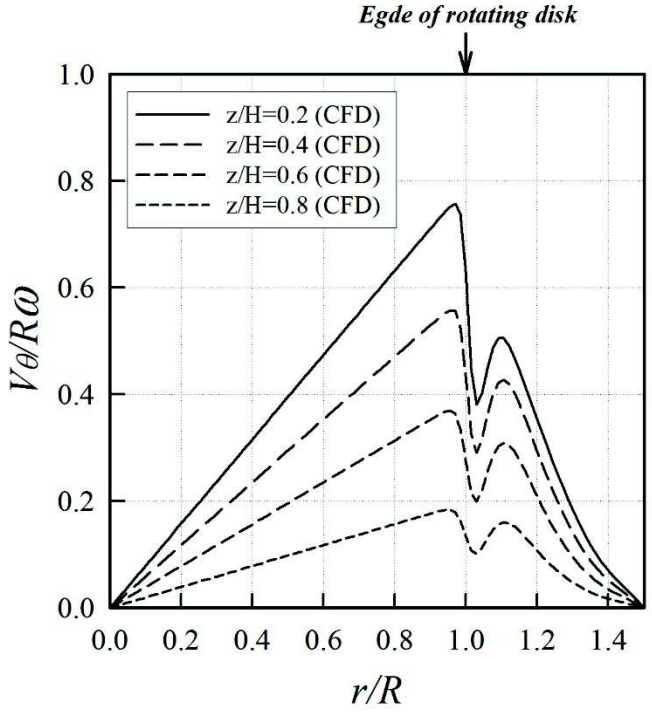

(b) Tangential velocity

Figure 3-9c Radial and tangential velocity profiles plotted as a function of r/R for rotational speeds of 500rpm (H=250μm).

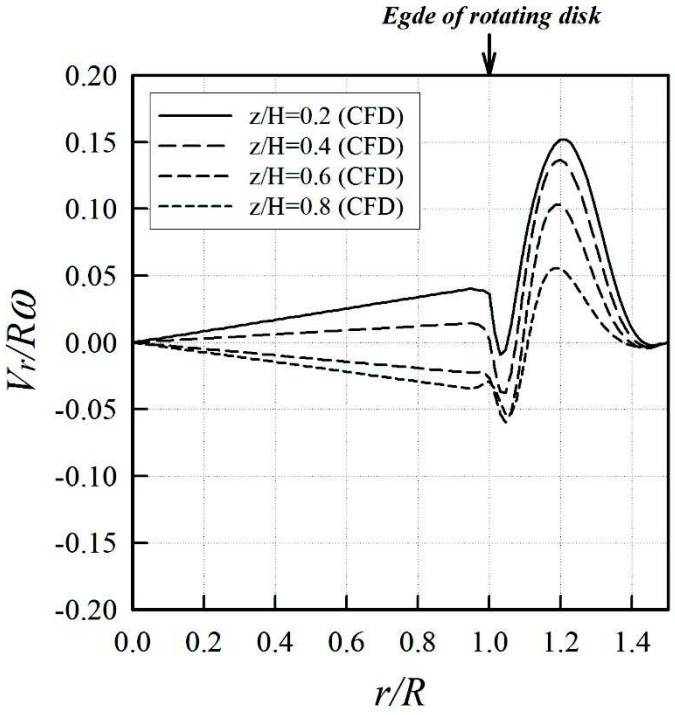

(a) Radial velocity

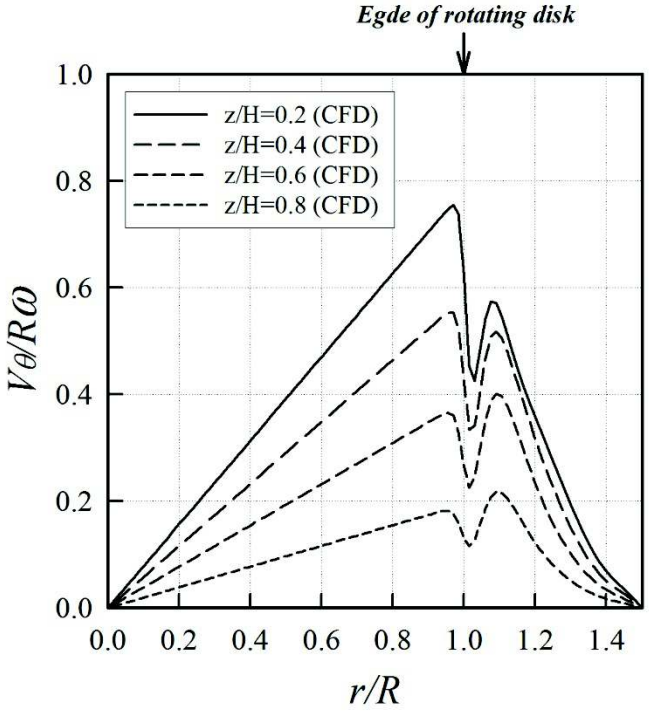

(b) Tangential velocity

Figure 3-9d Radial and tangential velocity profiles plotted as a function of r/R for rotational speeds of 700rpm (H=250μm).

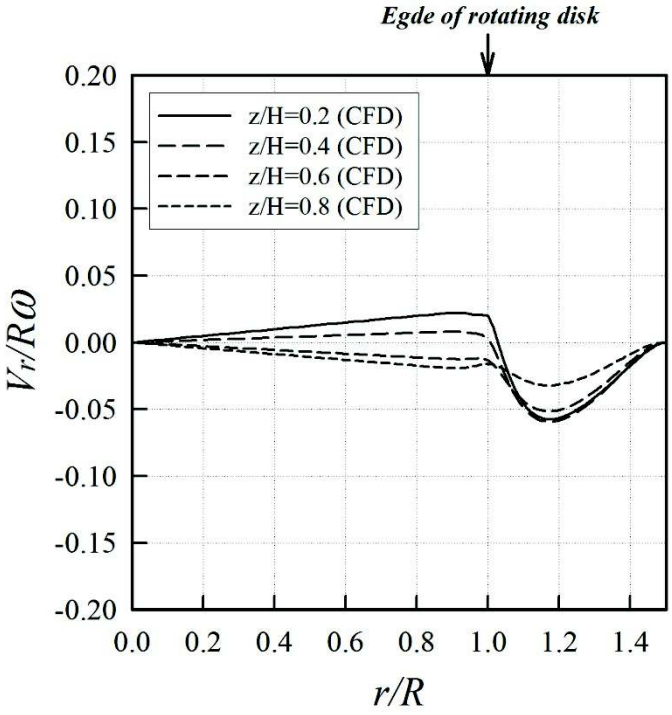

(a) Radial velocity

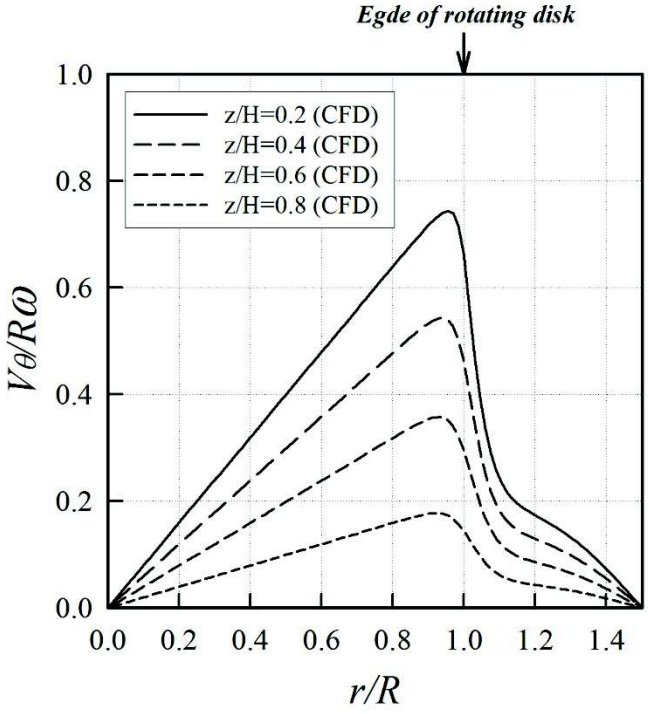

(b) Tangential velocity

Figure 3-10a Radial and tangential velocity profiles plotted as a function of r/R for rotational speeds of 100rpm (H=500μm).

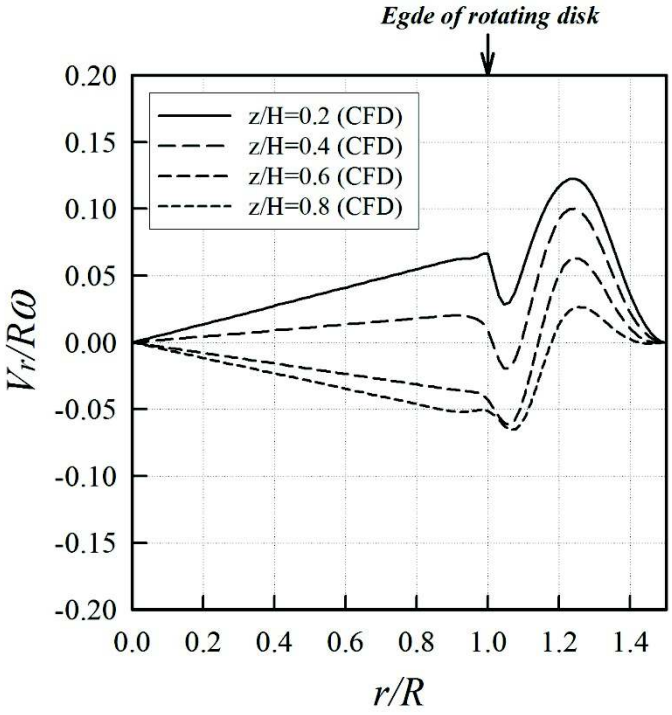

(a) Radial velocity

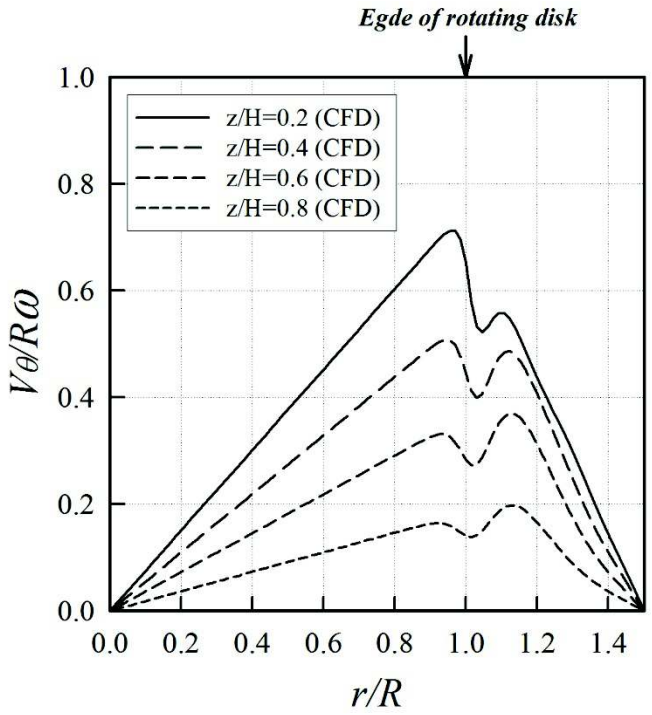

(b) Tangential velocity

Figure 3-10b Radial and tangential velocity profiles plotted as a function of r/R for rotational speeds of 300rpm (H=500μm).

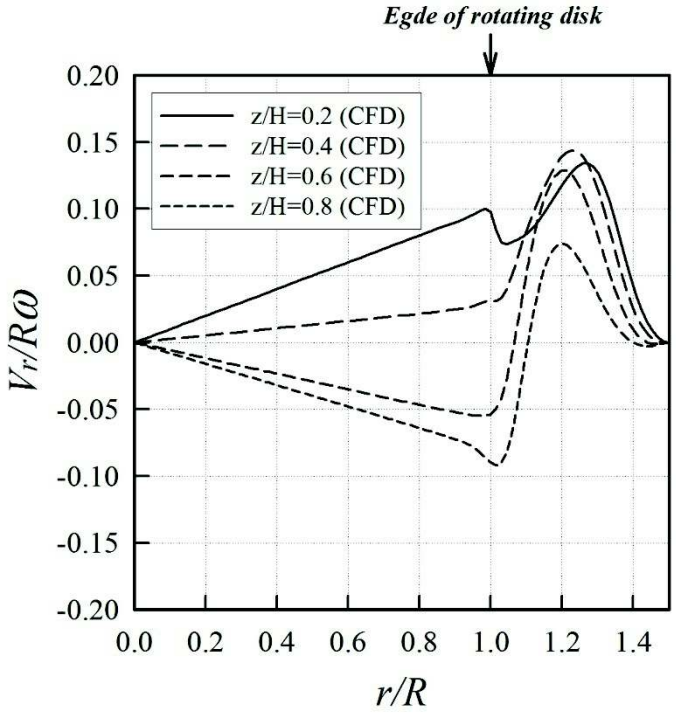

(a) Radial velocity

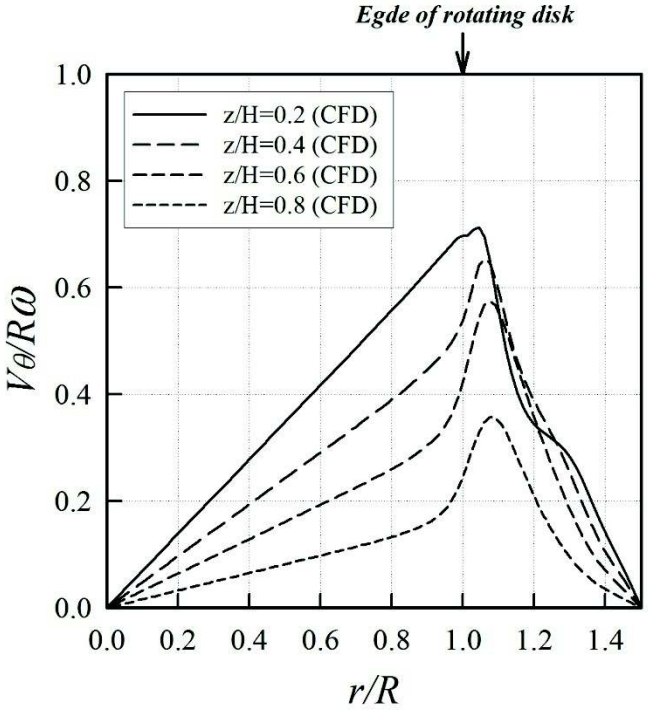

(b) Tangential velocity

Figure 3-10c Radial and tangential velocity profiles plotted as a function of r/R for rotational speeds of 500rpm (H=500μm).

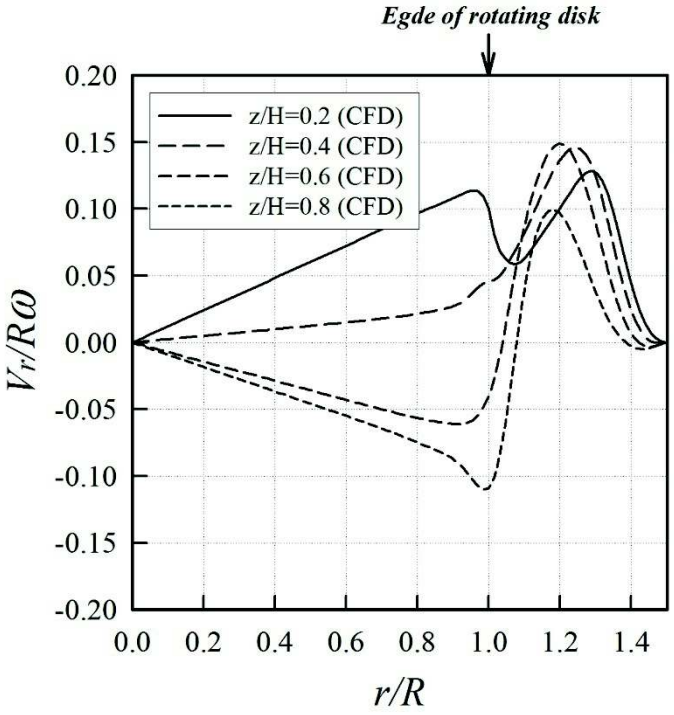

(a) Radial velocity

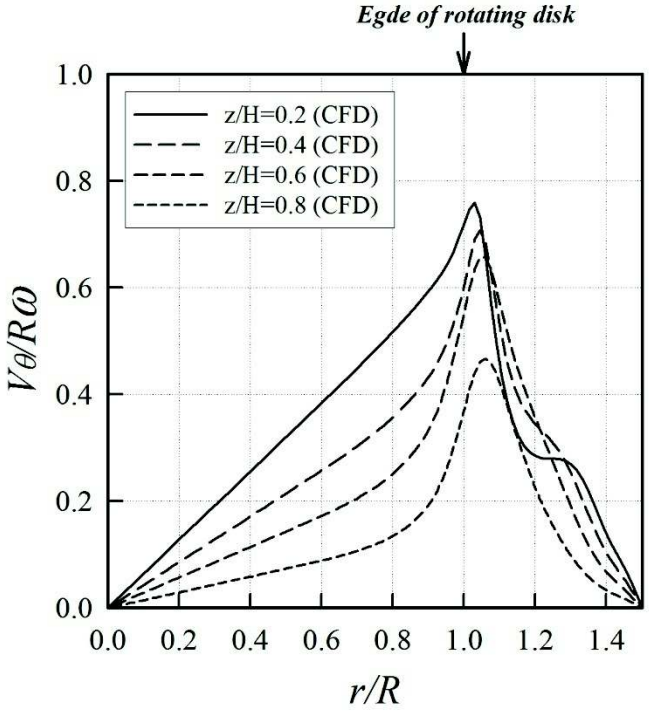

(b) Tangential velocity

Figure 3-10d Radial and tangential velocity profiles plotted as a function of r/R for rotational speeds of 700rpm (H=500μm).

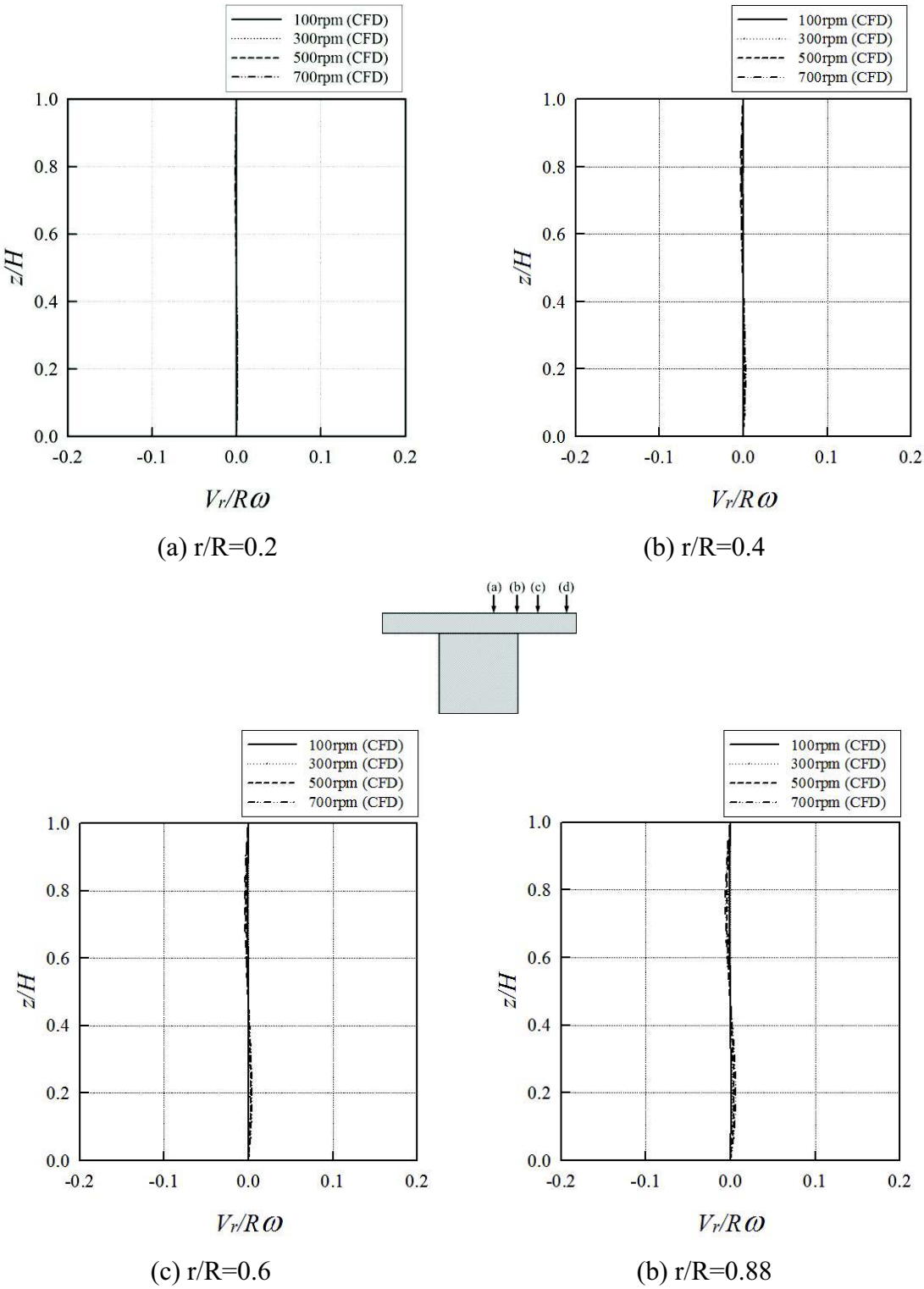

Figure 3-11a Radial velocity component plotted as a function of z/H (H=100μm).

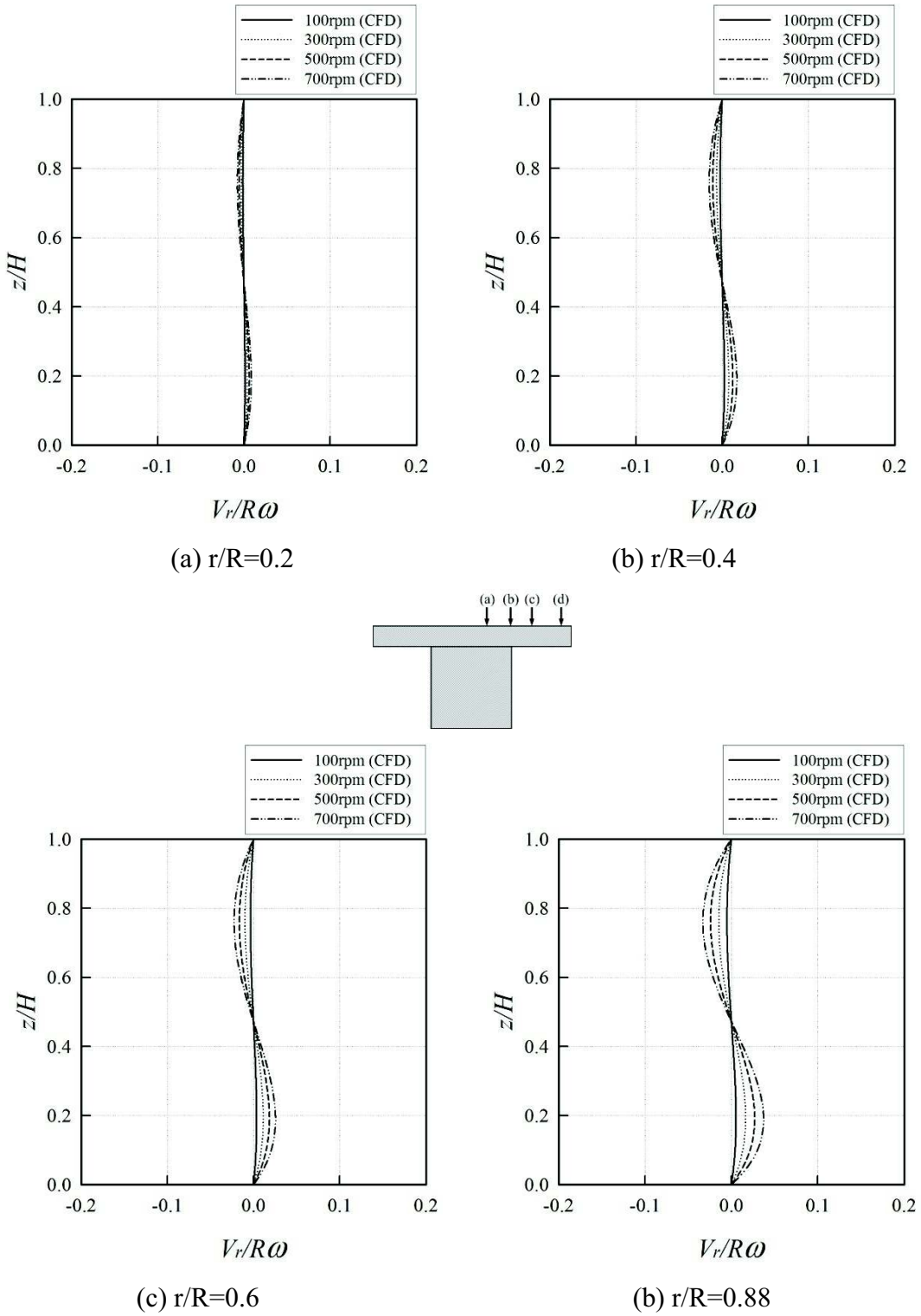

Figure 3-11b Radial velocity component plotted as a function of z/H (H=250μm).

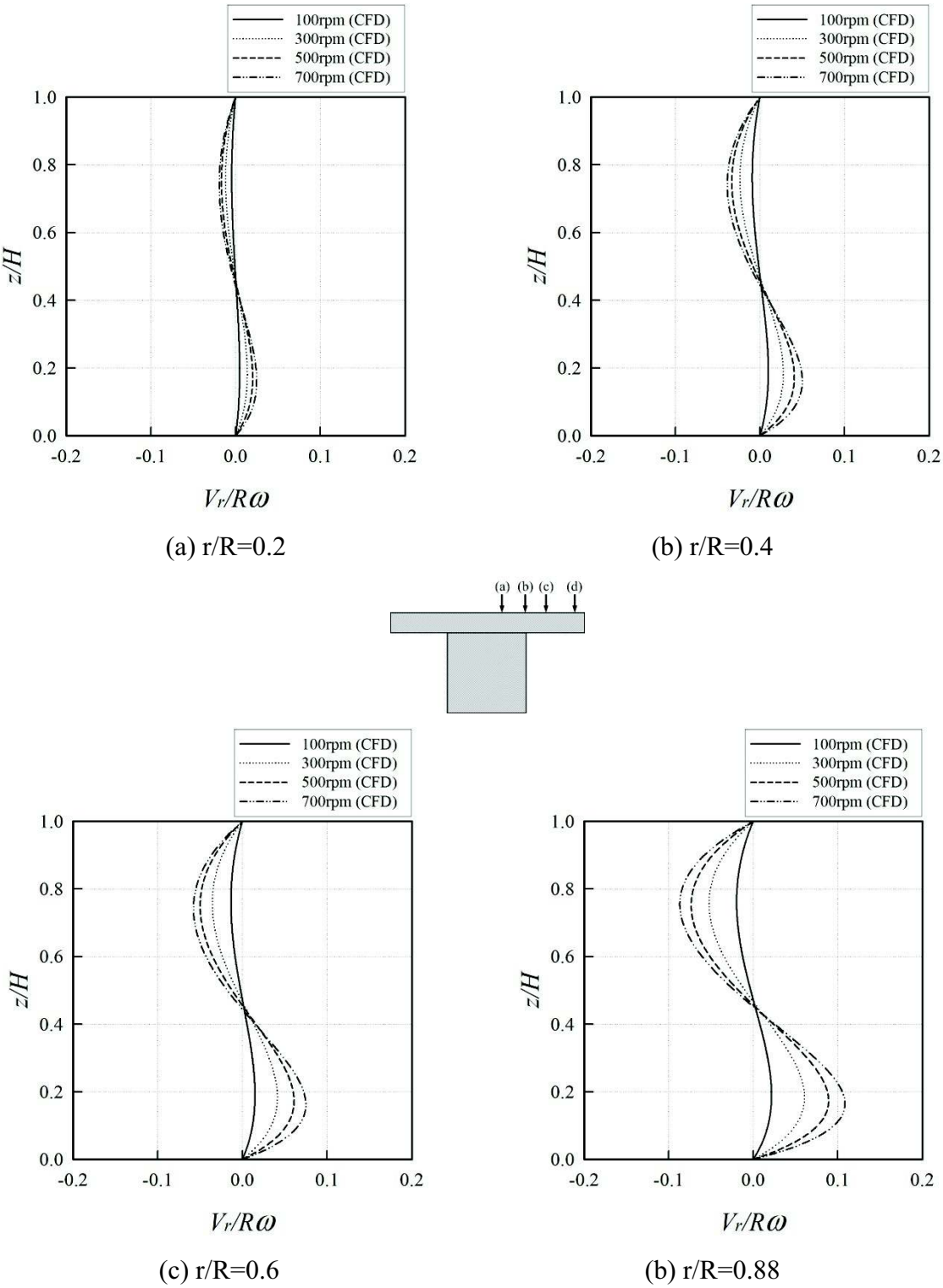

Figure 3-11c Radial velocity component plotted as a function of z/H (H=500μm).

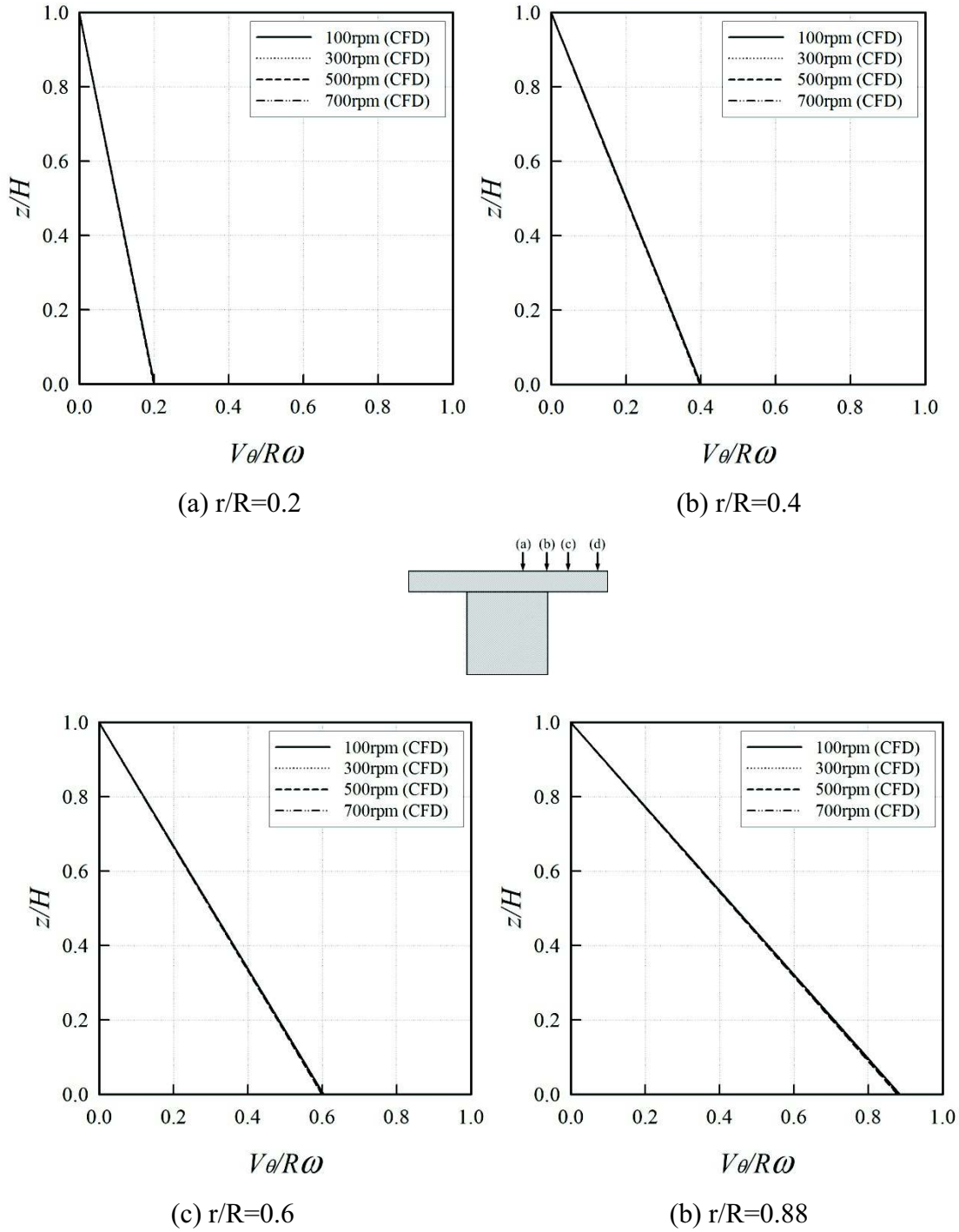

Figure 3-12a Tangential velocity component plotted as a function of z/H (H=100μm).

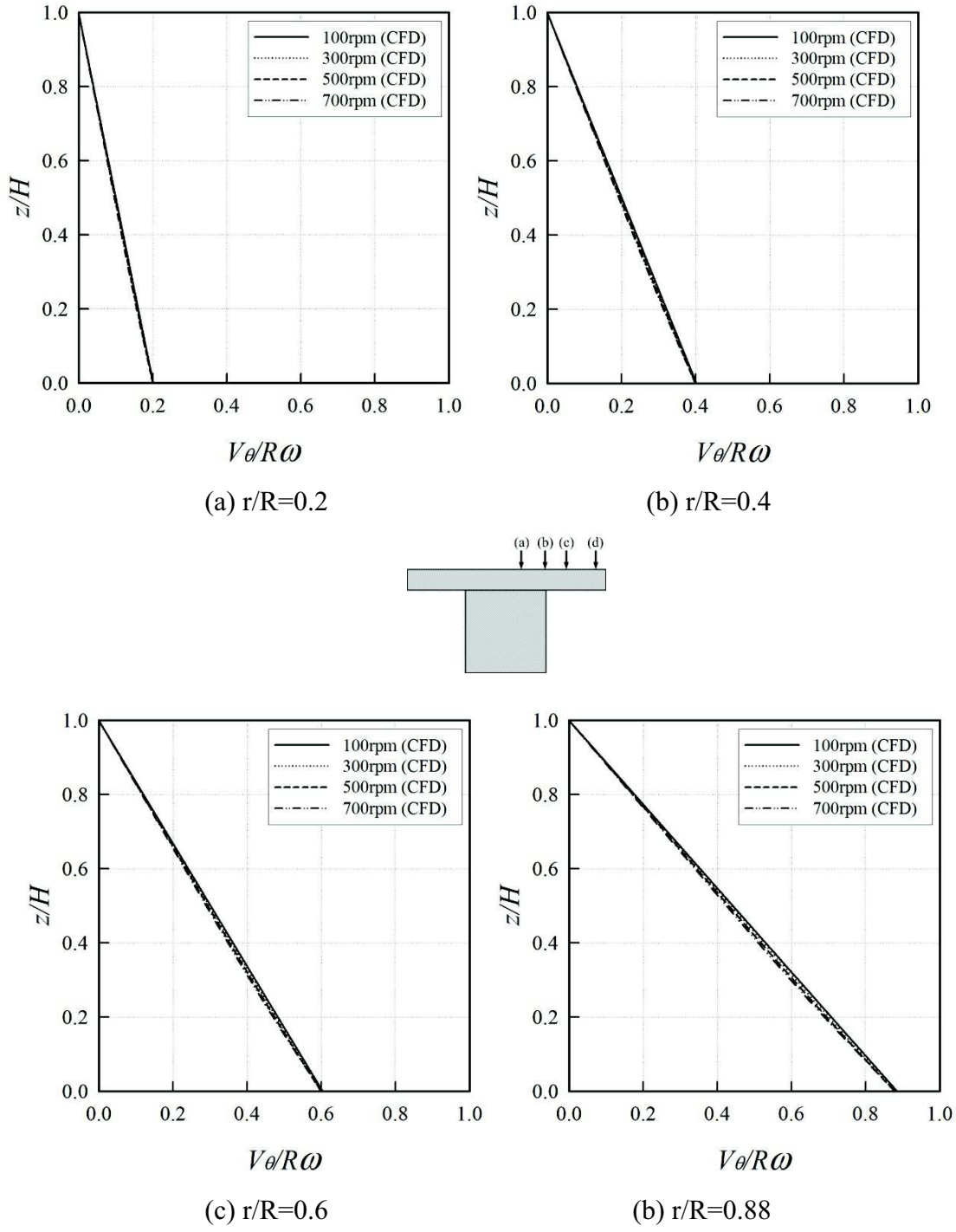

Figure 3-12b Tangential velocity component plotted as a function of z/H (H=250μm).

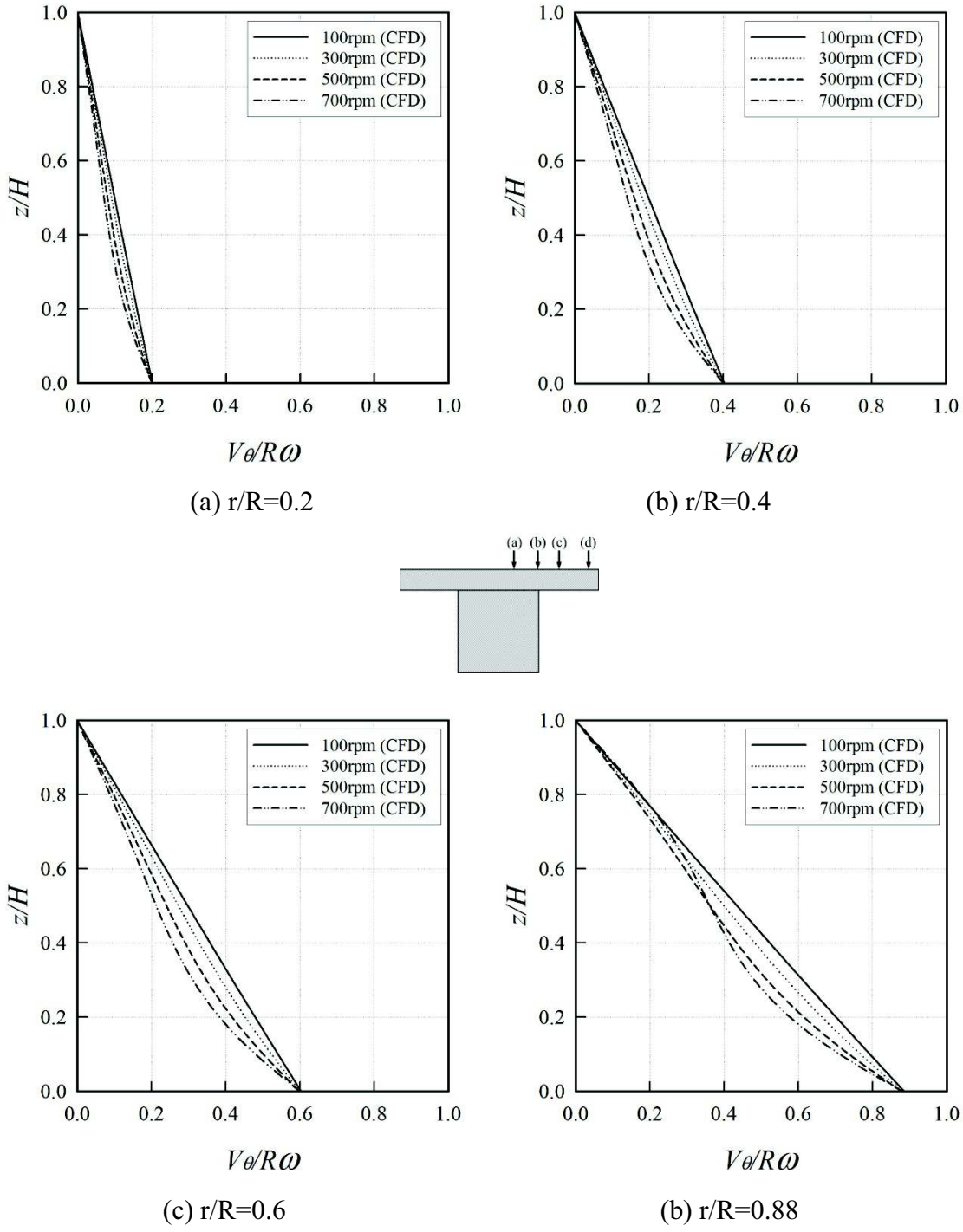

Figure 3-12c Tangential velocity component plotted as a function of z/H (H=500μm).

Chapter 4. Digital image processing – frequency sampling method

4.1 Introduction

Image processing is a general term for the wide range of techniques which exist for manipulating and modifying images in various ways. Photographers and physicists can perform certain image processing operations using chemicals or optical equipment.

In the early 1920s, true digital image processing (DIP) was not possible until the advent of large-scale digital computing hardware.

The early motivation for the development of DIP techniques came from the space program; in 1964, NASA's Jet Propulsion Laboratory used computers to correct distortions in images of the lunar surface obtained by the Ranger 7 probe.

Now, more than five decades later, DIP finds applications in areas as diverse as medicine, military reconnaissance and desktop publishing. We also have a concern to use digital image processing, i.e., that which is performed on fluorescent particle images in micro-PIV measurement of micro flow; especially MATLAB programming is used. In this chapter 4, it will be considered how digital images may be manipulated and enhanced to improve accuracy of measurement of flow velocity in micro rotating disk flow using micro particle image velocimetry.

Digital filters can be classified into two groups. In the first group, $f(x, y)$ is a finite-extent sequence, so the filters in this group are called finite impulse response (FIR) filters. In the second group, $f(x, y)$ is of infinite extent, so the filters in this group are called infinite impulse response (IIR) filters. Herein, we concentrate on the finite impulse response and describe in detail frequency sampling method to one method of FIR filters.

4.2 Digital Images

A digital image, which can be denoted by *I(x , y)*, is typically obtained by sampling the images, for instance, an image on CCD camera. The amplitude of a digital image is often quantized to 256 levels, which can be represented by 8 bits. Each level is commonly expressed by an integer; with 0 corresponding to the darkest level and 255 to the brightest. Each point *I(x, y)* is called a pixel (picture element). For monochrome images, the value of the function at any pair of coordinates, *x* and *y*, is the intensity of the light detected at that point.

In the micro-PIV experiment, the images using in calculating of velocity magnitude and velocity vectors have the spatial resolution of 1600×1200. The digital image with each pixel represented by 8 bits is shown in Fig. 4-1.

4.3 Sampling

The pattern is defined in a coordinate system whose origin is conventionally defined as the upper-left corner of the image (Figure 4-1). It can be described the pattern by a function, *I(x, y)*. For monochrome images, the value of the function at any pair of coordinates, *x* and *y*, is the intensity of the light detected at that point.

The function *I(x, y)* must be translated into a discrete array of numerical data if it is to undergo computer processing. This digital representation is only an approximation of the original image, but that is the price we must pay for the convenience of being able to manipulate the image using a computer. Translation of *I(x, y)* into an appropriate numerical form is accomplished by the processes of sampling and quantization.

Sampling is the process of measuring the value of the image function *f(x, y)* at discrete intervals in space. Each sample corresponds to a small, square area of the image, known as a pixel. A digital image is a two-dimensional array of these pixels. Pixels are indexed by *x* and *y* coordinates, which *x* and *y* have integer values.

4.3.1 Spatial resolution

The spatial resolution of an image is the physical size of a pixel in that image; i.e. , the area in the scene that is represented by a single pixel in the image. For a given field of

view, dense sampling will produce a high resolution image in which there are many pixels, each of which represents the contribution of a very small part of the scene; coarse sampling, on the other hand, will produce a low resolution image in which there are few pixels, each representing the contribution of a relatively large part of the scene to the image. In deciding whether a digital image has been sampled appropriately, we must consider the rapidity with which the value of *f (x, y)* changes as we move across the image. This rate of change is measured by spatial frequency. Gradual changes in *f(x, y)* are characterized by low spatial frequencies and can be represented adequately in a coarsely-sampled image; rapid changes are characterized by high spatial frequencies and can be represented accurately only in a densely-sampled image. Wherever possible, the sampling that we choose for an image should satisfy the Nyquist criterion. Essentially, this states that the sampling frequency should be at least double the highest spatial frequency found in the image. If we sample an image coarsely, such that the Nyquist criterion is not met, then the image may suffer from the effects of aliasing.

4.3.2 Quantization

It is usual to digitize the values of the image function, *f (x, y)*, in addition to its spatial coordinates. This process of quantization involves replacing a continuously varying *f (x, y)* with a discrete set of quantization levels. The accuracy with which variations in *f (x, y)* are represented is determined by the number of quantization levels that we use; the more levels we use, the better the approximation.

Conventionally, a set of *n* quantization levels comprises the integers 0, 1, 2,⋯, *n*-1.

0 and *n*-1 are usually displayed or printed as black and white, respectively, with intermediate levels rendered in various shades of grey. Quantization levels are therefore commonly referred to as grey levels. The collective term for all the grey levels, ranging from black to white, is a grey scale.

For convenient and efficient processing by a computer, the number of grey levels, *n*, is usually an integral power of two. It may be written by

$$n = 2^b, \tag{4.1}$$

where b is the number of bits used for quantization. b is typically 8, giving us images with 256 possible grey levels ranging from 0 (black) to 255 (white).

4.4 The frequency domain

Images represent variations of brightness in space. These spatial variations can be manipulated by operations such as convolution. There exists an alternative representation of an image based on the frequencies of brightness variation in that image. These can be converted into a spectrum of different frequency components and convert this spectral representation back into a spatial representation without any loss of information. These can also process the image in the frequency domain by manipulating its spectrum. In the section 4.4, the nature of the frequency domain is explained and considered the computational techniques used to move between domains and examine the ways in which images can be changed by manipulating their spectra.

4.4.1 Spatial frequency

The areas of an image in which grey level varies rapidly with distance contain high spatial frequencies; conversely, areas in which grey level varies slowly contain only low spatial frequency components. But what does it mean precisely by the term 'spatial frequency?' Frequency has a precise meaning when considering periodic functions. A periodic function such as the sinusoid in Fig. 4-2 consists of a fixed pattern or cycle that repeats endlessly in both directions. The length of this cycle, L , is known as the period of the function. The frequency of variation is the reciprocal of the period. If the variation is spatial and L is a distance, then l/L is termed the spatial frequency of the variation. A periodic variation is characterized by two further parameters: an amplitude and a phase. The amplitude (labeled A in Fig. 4-2) is the size of the variation-the height of a peak or depth of a trough. The phase (ϕ in Fig. 4-2) is the position of the start of a cycle, relative to some reference point (e.g., the origin). A sine function has $\phi = 0$ whereas a cosine function has $\phi = \pi / 2$.

What does a sinusoidal variation of image intensity look like? We investigate this by defining a sinusoidal function and rendering it as an image. A suitable function is

$$f(x,y) = 128 + A\sin(\frac{2\pi fn}{N-1}) + \phi \tag{4.1}$$

This function generates a sinusoidal variation along the *x* axis, about a mean grey level of 128. (This offset is necessary because 8-bit grey-scale images cannot represent the negative values produced by a sine function.) Amplitude, *A*, is a value in the range [1,127]. *N* is the width of the image, in pixels. The parameter *f* is a dimensionless spatial frequency, corresponding to the number of complete cycles of the sinusoid that fit into the width of the image. (Dividing by *N* would give the spatial frequency in units of cycles per pixel.) Lastly, ϕ is the phase.

Figure 4-3 shows the image generated by equation (4.2) with parameter values $N = 100$, $f = 3$, $A = 127$, and $\phi = 0$.

4.5 Fourier theory

4.5.1 Basic concepts

Techniques for the analysis and manipulation of spatial frequency are based on the work of the eighteenth century French physicist Jean Baptiste Joseph Fourier. Fourier developed a representation of functions, based on frequency, that is, of considerable importance in many branches of science and engineering.

Fourier's theory considers sinusoidal variations (i.e, sine and cosine waves), of the kind depicted in Fig. 4-2. The key idea is that any periodic function, however complex it might appear, can be represented as a sum of these simpler sinusoids. This solves the problem of whether it is meaningful to think of spatial frequency in a real, highly complicated image. Although there may be little regularity apparent in such an image, it can be decomposed into a set of sinusoidal components, each of which has a well-defined frequency.

A set of sine and cosine functions having particular frequencies are chosen for the representation. These are termed the basic functions of the representation. A weighted sum of these basis functions is called a Fourier series. The weighting factors for each sine and cosine function are known as the Fourier coefficients.

We can write the summation as follows:

$$\begin{aligned} f(x) &= \sum_{n=0}^{\infty} a_n \cos\left(\frac{2\pi fx}{L}\right) + b_n \sin\left(\frac{2\pi fx}{L}\right) \\ &= a_0 + \sum_{n=0}^{\infty} a_n \cos\left(\frac{2\pi fx}{L}\right) + b_n \sin\left(\frac{2\pi fx}{L}\right) \end{aligned} \tag{4.3}$$

The index *f* in this equation is the number of cycles of the sinusoid that fit within one period of *f(x)*. Thus, *f* can be considered as a dimensionless measure of the frequency of a basic function. Equation (4.3) indicates that a function with period *L* can be represented by two infinite sequences of coefficients.

These concepts may need convincing that a summation of smoothly varying functions such as sinusoids can synthesize the sharp discontinuities and relatively homogeneous regions that might be found in an image.

4.5.2 Extension to two dimensions

The notion of a Fourier series is equally valid in two dimensions and the basic functions are two-dimensional sine and cosine functions. A Fourier series representation of a two-dimensional function, $f(x, y)$, having a period L in both the x and the y directions, can be written

$$f(x,y) = \sum_{f_x=0}^{\infty}\sum_{f_y=0}^{\infty} a_{f_x,f_y} \cos\left[\frac{2\pi(f_x x + f_y y)}{L}\right] + b_{f_x,f_y} \sin\left[\frac{2\pi(f_x x + f_y y)}{L}\right] \tag{4.4}$$

Here, f_x and f_y are the number of cycles fitting into one horizontal and vertical period of $f(x, y)$. We can regard the Fourier series representation of $f(x, y)$ as a pair of two-dimensional arrays of coefficients, each of infinite extent. The Fourier series in equation (4.4) can be used to represent any image.

4.6 The discrete Fourier transform

Fourier theory provides us with a means of determining the contribution made by any basic function to the representation of some function *f(x)*. The contribution is determined by projecting *f(x)* onto that basic function. This procedure is described as a Fourier transform. When applying the procedure to images, it must be dealt explicitly with the fact that an image is

- Two-dimensional
- Sampled
- Of finite extent

These considerations give rise to the discrete Fourier transform (DFT).

The DFT of an $N \times N$ image can be written

$$F(f_x, f_y) = \frac{1}{N} \sum_{x=0}^{N-1} \sum_{y=0}^{N-1} f(x,y) \left[\cos\left(\frac{2\pi(f_x x + f_y y)}{N} \right) + j \sin\left(\frac{2\pi(f_x x + f_y y)}{N} \right) \right] \tag{4.5}$$

or, $\cos\theta + j\sin\theta$ can be written in exponential form,

$$F(f_x, f_y) = \frac{1}{N} \sum_{x=0}^{N-1} \sum_{y=0}^{N-1} f(x,y) e^{-j2\pi(f_x x + f_y y)/N} \tag{4.6}$$

$F(f_x, f_y)$ is a complex number and now dealing with a set of complex coefficients, rather than two sets of real coefficients; as was the case with the Fourier series in equation (4.4).

For any particular spatial frequency specified by f_x and f_y, evaluating equation (4.6) gives us the contribution that the corresponding pair of basic images makes to a Fourier representation of the image *f*; in essence, it tells us how much of that particular frequency is present in the image. Of course, in order to build up a complete picture of

the relative importance of different frequencies, it must be evaluated by the equation for all f_x and f_y. It is usual to apply the term 'Fourier transform' to the process of calculating all the values of $F(f_x, f_y)$ or to the values themselves.

There also exists an inverse Fourier transform that converts a set of Fourier coefficients into an image. It has a form very similar to the forward transform:

$$f(x,y) = \frac{1}{N}\sum_{x=0}^{N-1}\sum_{y=0}^{N-1} F(f_x, f_y) e^{j2\pi(f_x x + f_y y)/N} \tag{4.7}$$

The only material difference is the sign of the exponent. Comparing equations (4.6) and (4.7), it is clear that the forward transform of an $N \times N$ image yields an $N \times N$ array of coefficients. Since the inverse transform reconstructs the original image from this set of coefficients, they must constitute a complete representation of the information present in the image. When $F(f_x, f_y)$ is manipulated, it is said that the image is being processed in the frequency domain; conversely, when pixel values, *I(x, y),* are manipulated, the image is being processed in the spatial domain. Although these manipulations may result in the loss of information from the image, the transformation from one domain to the other through a forward or inverse Fourier transform does not, in itself, result in any information loss.

4.6.1 The spectra of an image

It was already said that $F(f_x, f_y)$ is a complex number. Its real and imaginary parts are not particularly informative in themselves; it is far more useful to think of the magnitude and phase of $F(f_x, f_y)$.

This is expressed as;

$$F(f_x, f_y) = R(f_x, f_y) + jI(f_x, f_y) = \left|F(f_x, v)\right| e^{j\phi(f_x, f_y)} \tag{4.8}$$

,where $R(f_x, f_y)$ and $I(f_x, f_y)$ are the real and imaginary parts of $\left|F(f_x, f_y)\right|$,

$\left|F(f_x, f_y)\right|$ is the magnitude and $\phi(u, v)$ is the phase.

Magnitude and phase are given by

$$\left|F(f_x, f_y)\right| = \sqrt{R^2(f_x, f_y) + I^2(f_x, f_y)} \tag{4.9}$$

$$\phi(f_x, f_y) = \tan^{-1}\left[\frac{I(f_x, f_y)}{R(f_x, f_y)}\right] \tag{4.10}$$

Equations (4.9) and (4.10) allow us to decompose an array of complex coefficients into an array of magnitudes and an array of phases. The magnitudes correspond to the amplitudes of the basic images in our Fourier representation. The array of magnitudes is termed the amplitude spectrum of the image. Likewise, the array of phases is termed the phase spectrum. When the term 'spectrum' is used on its own, the amplitude spectrum is normally implied. This is because the phases are generally less significant for the purposes of interpretation. Another term that is used is power spectrum, or spectral density. The power spectrum of an image is simply the square of its amplitude spectrum, i.e.,

$$P(f_x, f_y) = \left|F(f_x, f_y)\right|^2 = R^2(f_x, f_y) + I^2(f_x, f_y) \tag{4.11}$$

It can be rendered by the spectra of an image as images themselves, for the purposes of visualization and interpretation.

Figure 4-4 shows examples of an amplitude spectrum and a phase spectrum of a fluorescent particle image.

4.6.2 The fast Fourier transform

Calculating a single value of $F(f_x, f_y)$ by equation (4.6) involves a summation over all pixels in the image. If the image has dimensions $N \times N$, then this is an $O(N^2)$ operation. However, there are N^2 values of $F(f_x, f_y)$ to calculate, so the overall complexity of a DFT is $O(N^4)$. This is very inefficient.

Fortunately, a much faster method exists, known as the Fast Fourier transform (FFT).

The classic two-dimensional FFT algorithm takes advantage of the separability of the Fourier transform, which allows us to perform a one-dimensional FFT along each row of the image to generate an intermediate array, followed by another one-dimensional FFT down each column of this array to produce the final result. The one-dimensional FFT algorithm uses another trick to speed up calculations. It so happens that a Fourier transform of length N can be written as the sum of two Fourier transforms, each of length $N/2$. If N is a power of two, this decomposition can be applied recursively until the point is reached, where we are computing transforms of length 2.

The overall cost of this procedure is $O(N \log_2 N)$, compared with $O(N^2)$ for a directly calculated one-dimensional transform.

Exploiting separability alone reduces the complexity of a two-dimensional Fourier transform from $O(N^4)$ to $O(N^3)$. When we introduce the one-dimensional FFT, the cost of transforming an $N \times N$ image becomes $O(N \log_2 N)$.

4.7 Filtering of images

Images can be filtered in the spatial domain by operations such as convolution. Convolution with the appropriate kernel can blur or sharpen an image. The operation suppresses or enhances certain spatial frequencies relative to others. However, it cannot be quantified by the effect because the operation takes place in the spatial domain. The frequency domain is the more natural domain for filtering because of the effect that a filter has on the spatial frequencies present in an image. Moreover, filtering in the frequency domain is simpler, computationally, than convolution in the spatial domain.

Filtering can be expressed generally as the point-by-point multiplication of the spectrum by a filter transfer function. It can be expressed by

$$G(f_x, f_y) = F(f_x, f_y)H(f_x, f_y) \tag{4.12}$$

,where $F(f_x, f_y)$ is the spectrum of the image, $H(f_x, f_y)$ is the filter transfer function and $G(f_x, f_y)$ is the filtered spectrum. An inverse Fourier transform of

$G(f_x, f_y)$ must be computed to see the results of filtering as an image. Remember that we are dealing with complex numbers here. The multiplication in equation (4.12) could, in theory, affects both the magnitude and phase of $F(f_x, f_y)$. In practice, most filters are zero-phase-shift filters; that is, they affect magnitude rather than phase. There is a fundamental relationship between filtering done by convolution in the spatial domain and filtering done by multiplication in the frequency domain. This is expressed by the convolution theorem, which states that

$$f * h \Leftrightarrow FH \tag{4.13}$$

The left-hand side of this expression represents the convolution of an image, f, with a kernel, h. The right-hand side of the expression represents the product of the Fourier transform of the image, $F(f_x, f_y)$, and the Fourier transform of the kernel, $H(f_x, f_y)$.

The symbol *, which links the two sides, indicates that they form a 'Fourier transform pair'; the left-hand side can be converted into the right-hand side by a Fourier transform, whereas the right-hand side can be converted into the left-hand side by an inverse Fourier transform. Equation (4.13) tells us that convolving an image with a given kernel has the same effect on an image as multiplying the spectrum of that image by the Fourier transform of the kernel. Any result achievable by convolution in the spatial domain can also be obtained by a multiplication in the frequency domain, and vice versa. This means that we always have two different ways of carrying out linear filtering operations. Given a kernel, it can be convolved that kernel with the image, or can be filtered in the frequency domain through the following procedure:

[Step 1] Compute the Fourier transform of the image
[Step 2] Compute the Fourier transform of the kernel
[Step 3] Multiply the two transforms together
[Step 4] Compute the inverse Fourier transform of the product

In step 3, the multiplication is done on a point-by-point basis, which means that the transforms of the kernel and the image must have the same dimensions. We accomplish

this by padding out the kernel with zeros prior to computing its transform.

Although it may seem strange to perform this rather complicated sequence of operations when we have a kernel that can be used directly for convolution, significant computational benefits can accrue from working in the frequency domain.

In the spatial domain, filtering requires approximately N^2n^2 multiplications and a similar number of additions. In the frequency domain, however, filtering (Step 3 above) requires only N^2 multiplications. Of course, there is a significant cost associated with FFT computation, but if n is large enough the total cost of filtering in the frequency domain falls below that of operating in the spatial domain.

4.8 Frequency sampling method

The frequency sampling method creates a filter based on a desired frequency response. If given a matrix of points that define the shape of the frequency response, this method creates a filter, whose frequency response passes through those points. Frequency sampling places no constraints on the behavior of the frequency response between the given points; usually, the response ripples in any areas. The ripples mean oscillations around a constant value. The frequency response of a practical filter often has ripples when the frequency response of an ideal filter is flat; if compared to the desired frequency response. These ripples are a fundamental problem with the frequency sampling design method. They occur wherever there are sharp transitions in the desired response; can reduce the spatial extent of the ripples by using a larger filter.

Despite of such a disadvantage, the frequency sampling method is used in practice because of its conceptual and computational simplicity.

The desired frequency response $H_d(f_x, f_y)$ used by frequency sampling method is sampled at equally spaced points on the Cartesian grid; the result is inverse discrete Fourier transformed. Let $H'(x, y)$ be obtained by

$$H'(x,y) = H_d(f_x, f_y)e^{-jf_x(N_1-1)/2}e^{-jf_y(N_2-1)/2}\Big|_{f_x=(2\pi/N_1)x, f_y=(2\pi/N_2)x} \qquad (4.14)$$

,where $H_d(f_x, f_y)$ is the desired zero-phase frequency response, and N_1 and N_2 are odd. The corresponding sequence $h'(x, y)$ is obtained from equation (4.14) by

$$h'(x, y) = IDFT\,[H'(f_x, f_y)] \tag{4.15}$$

Finally, the zero-phase filter $h(x, y)$ designed is given by

$$h(x, y) = h'\left(x + \frac{N_1 - 1}{2}, y + \frac{N_2 - 1}{2}\right) \tag{4.16}$$

The linear phase term in equation (4.14) and the resulting shift of the sequence in equation (4.16) are due to the fact that the DFT is defined only for a first-quadrant support sequence, which cannot zero phase. The inverse DFT in equation (4.15) can be computed by using an FFT algorithm for highly composite numbers N_1 and N_2. From the definition of the Fourier transform and the DFT, the frequency response of the designed filter $H(f_x, f_y)$ can be shown to be related to $H'(x, y)$ and therefore to $H_d(f_x, f_y)$ by

$$\begin{aligned} H(f_x, f_y) = {} & \frac{e^{-jf_x(N_1-1)/2} e^{-jf_y(N_2-1)/2}}{N_1 N_2} \\ & \cdot \sum_{x=0}^{N_1-1} \sum_{y=0}^{N_2-1} \frac{H'(x, y)}{(1 - e^{-j(2\pi/N_1)x} e^{-jf_x})(1 - e^{-j(2\pi/N_2)y} e^{-jf_y})} \end{aligned} \tag{4.17}$$

4.8.1 High pass filtering

An ideal high pass filter is defined. Frequencies up to the cutoff frequency are suppressed, whereas frequencies beyond this point pass through unchanged. The transfer function is

$$H(f_x, f_y) = \begin{cases} 0 & r(f_x, f_y) < r_0 \\ \\ 1 & r(f_x, f_y) \geq r_0 \end{cases} \tag{4.18}$$

This filter has an inverted cylindrical shape, as shown in Fig.4-5. Since with the ideal high pass filter, the sharp cutoff leads to ringing in the filtered image.

The examples of high pass filter designed by the frequency sampling method are shown in Fig. 4-6. Figure 4-6 shows the result of a high pass filter design with various sampling number. The region of the transition samples used is shown in Fig. 4-6(a), and the transition samples used are samples of a circularly symmetric linear interpolation between 0 and 1. The perspective plot and the contour plot of the frequency response of the resulting filter are shown in Fig. 4-6(a) and (b), respectively.

4.9 Summary for filtering in the frequency domain

This filtering procedure is summarized in Fig. 4-7.

1. The pre-processing stage has procedures such as determining image size and generating a filter.

2. The filter function $H(f_x, f_y)$ multiplies both the real and imaginary parts of $F(f_x, f_y)$ and compute the inverse Fourier transform of the product. If $H(f_x, f_y)$ is real, then the phase of the results is not changed.

3. Post-processing entails computing the real part of the result, cropping the image, and converting it to class uint8 or uint16 for storage.

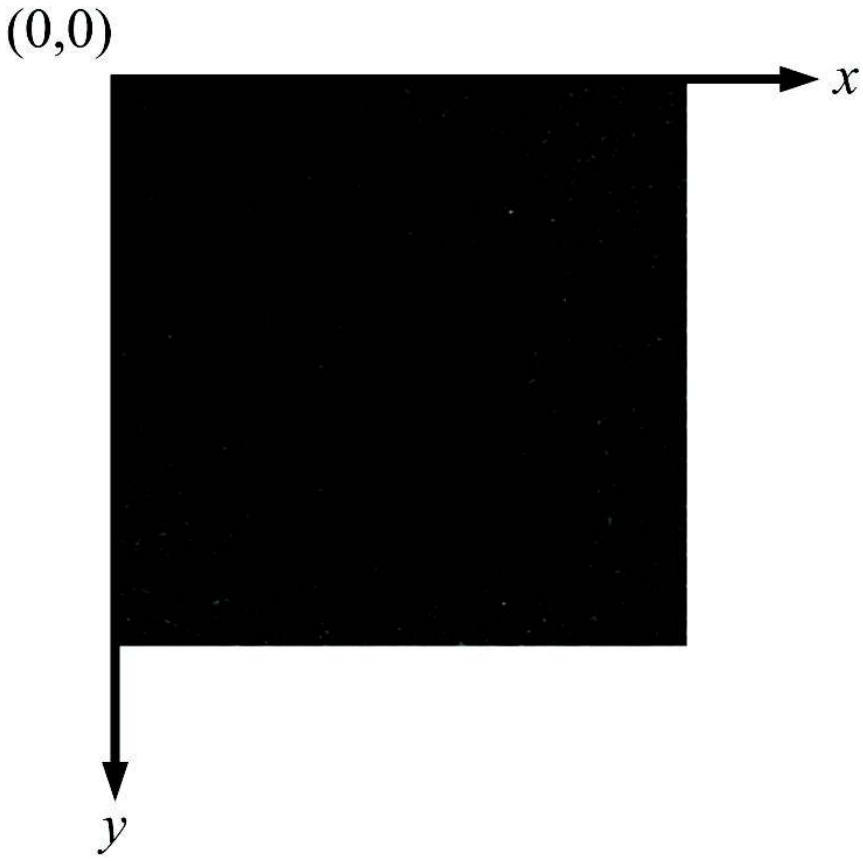

Figure 4-1 Coordinate system for a fluorescent particle image

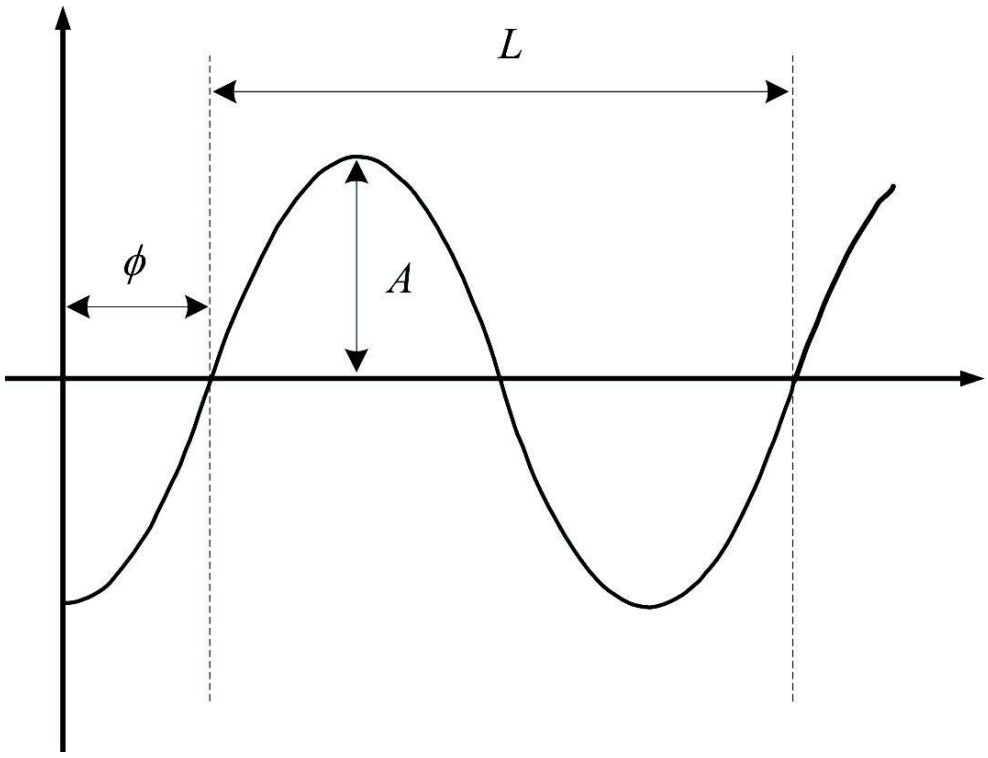

Figure 4-2 A sinusoidal function, characterized by a period(L), an amplitude (A) and phase(ϕ)

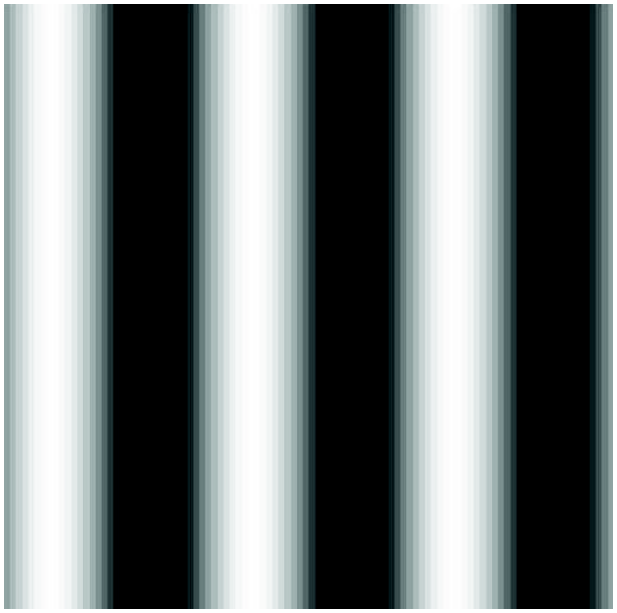

Figure 4-3 An image with a horizontal sinusoidal variation in grey level

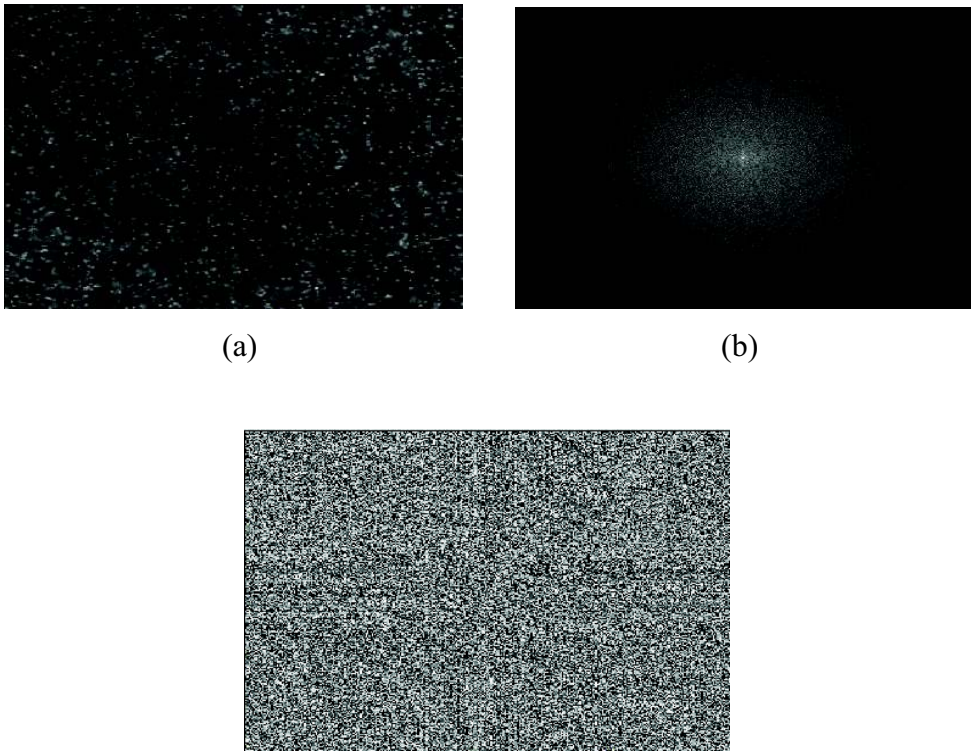

(a) (b)

(c)

Figure 4-4 A fluorescent particle image and its spectra.
(a) Image. (b) Amplitude spectrum. (c) Phase spectrum.

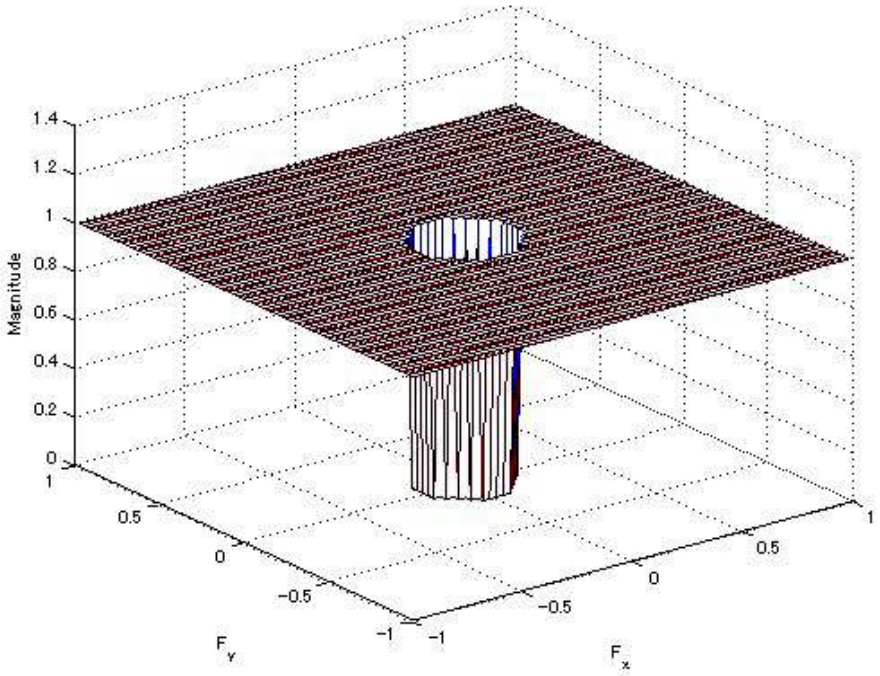

Figure 4-5 Example of an ideal high pass filter.

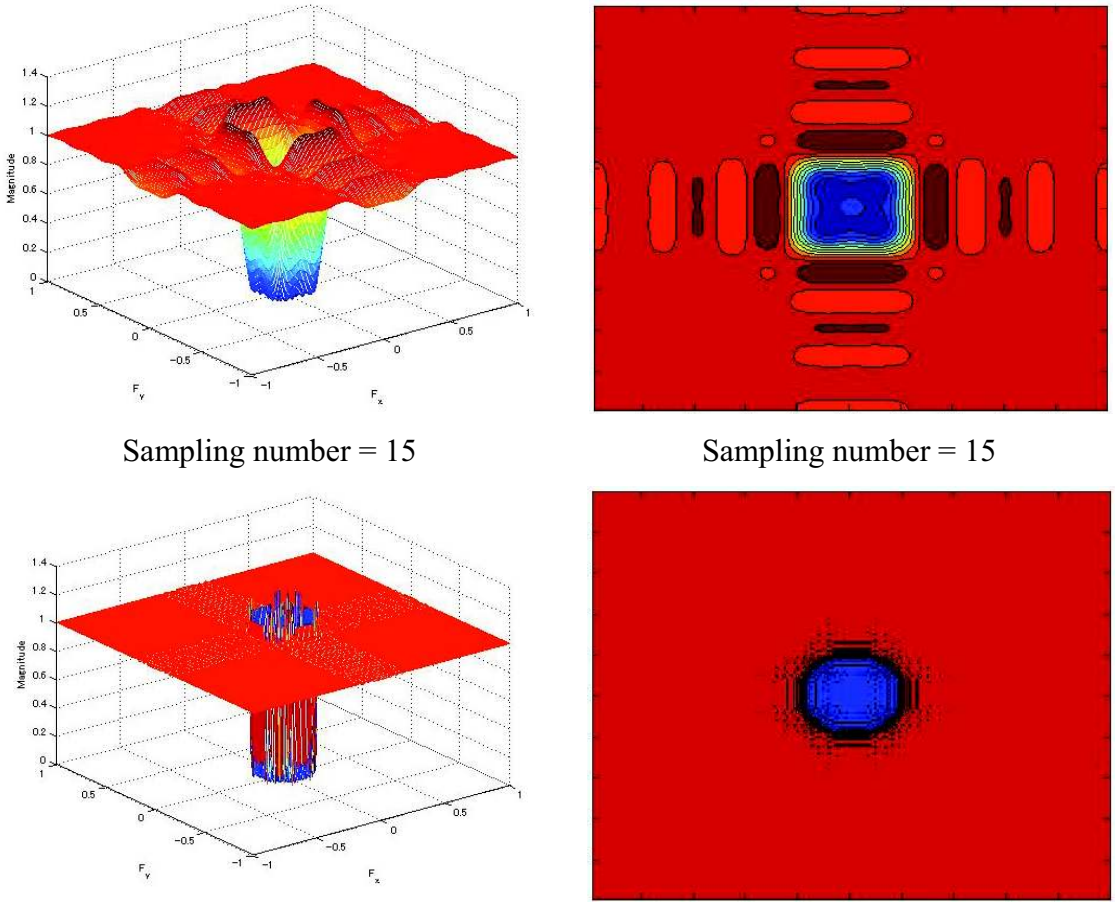

Sampling number = 15 Sampling number = 15

Sampling number = 149 Sampling number = 149

Figure 4-6 Effect of sampling numbers of high-pass filter designed by the frequency sampling method (a) perspective plot of the filter frequency response (b) contour plot of the filter frequency response (continue).

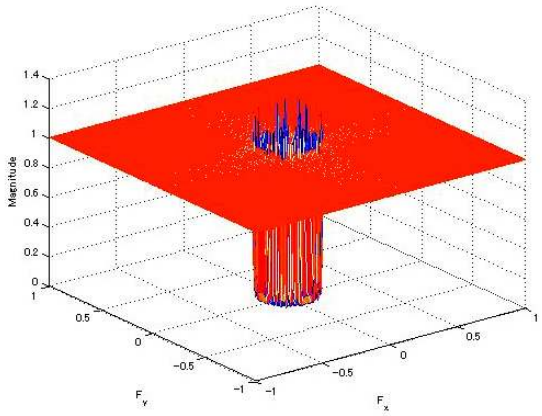

Sampling number = 499

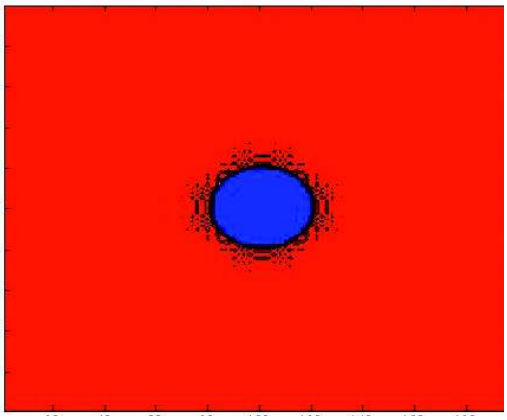

Sampling number = 499

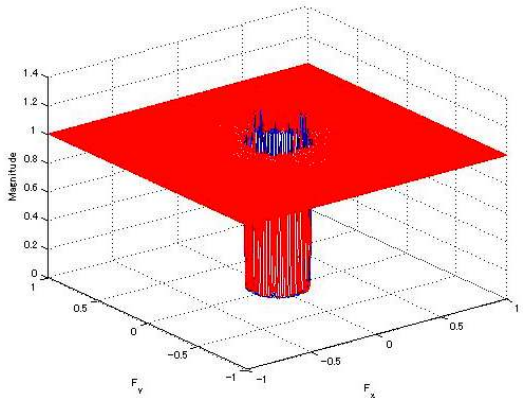

Sampling number = 1023

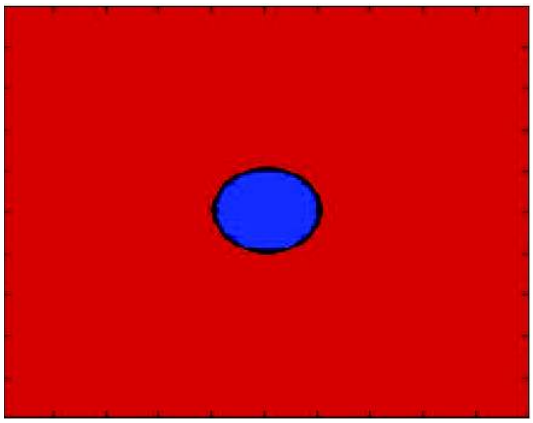

Sampling number = 1023

Figure 4-6 Various examples of high-pass filter designed by the frequency sampling method (a) perspective plot of the filter frequency response (b) contour plot of the filter frequency response (continue).

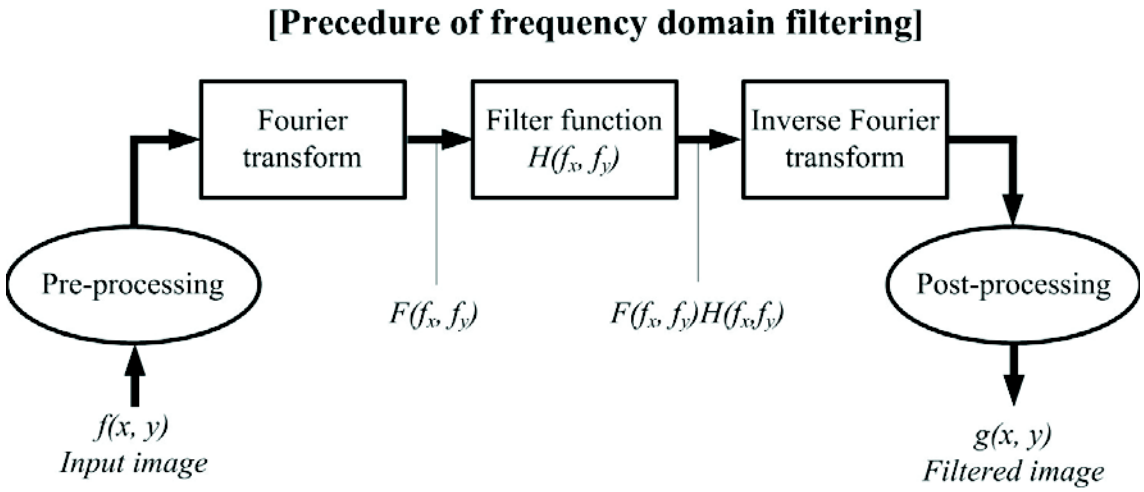

Figure 4-7 Steps for filtering in the frequency domain

Chapter 5. Micro-PIV measurement and CFD analysis of a thin liquid flow between stationary and rotating disks

5.1 Background

Recent progress in micro-PIV techniques has enabled one to make detailed measurement of fluid velocities in small-scale flows whose representative dimensions are in the order of sub-millimeter or even less. Such flows are seen in micro tubes/channels, porous media, droplets, films, and fluid layers. The present study focuses on a thin liquid layer that is present between a pair of rotating and stationary disks, whose separation is also in sub-millimeter order. This type of flow can be seen, for example, in the gap between an impeller and a casing in fluid machinery, in the gap between a rotating disk and its housing in hard disk drives, as well as in optical disk drives. Another application where this type of flow plays an important role is rotation-shearing chemical reactors that can enhance the mixing of chemical species introduced into the gap between rotating and stationary disks (e.g., Saito. 2001). This application utilizes the strong shear in a thin liquid layer where the liquid injected into the primary liquid layer undergoes highly three-dimensional deformation that leads to a remarkable enhancement of mixing of the liquids. As this mixing enhancement is dependent on the flow characteristics in the thin liquid layer, their clarification by means of both experimental and numerical methods is required for the design of higher-performance chemical reactors.

The micro-PIV technique was developed to make spatially-resolved measurement of small-scale fluid flows (e.g., Santiago et al. 1998). This technique has been used for the measurement of two-component flow velocities in two-dimensional domain in several micro-flow devices, such as a micro-pump (Sheen et al. 2008), a micro-valve (Pernod et al. 2010), a micro-actuator (Hagsäter et al. 2007), and a micro-mixer (Erkan et al. 2008). A well-known drawback of micro-PIV is its poor spatial resolution in the depth-of-field (DOF) direction of the measurement domain. As reported by Meinhart et al. (2000), the effective DOF of micro-PIV is determined by the spatial resolution of the objective used

for imaging, by the effect of diffraction in the DOF direction, and the size of the tracer particles used. The resultant DOF usually becomes much larger than the specified spatial resolution of the objective. This issue can be overcome by the use of three-dimensional micro-PIV techniques, as reported by Yoon and Kim (2006) and Park and Kihm (2006). This approach could be quite effective if the technique is successfully implemented into the actual measurement of the small-scale flow of interest. A different approach that is relatively simple, and thus easier, to implement is the use of digital filtering techniques to strengthen the signal-to-noise ratio of the particle images taken during the micro-PIV measurement. Gui et al. (2002) reported the use of digital filtering techniques for micro-PIV. Bourdon et al. (2004) proposed a new technique called "power-filtering technique" to improve the DOF in micro-PIV measurement. The principle behind this approach is to strengthen the signal (or intensity) from the particle images that are in focus in the measurement domain; it reduces the effective DOF for correlation analysis.

The present study aims at understanding the characteristics of the flow field in a strongly-sheared thin liquid layer between a pair of rotating and stationary disks. This particular configuration provides a basic flow configuration for the rotation-shearing chemical reactors mentioned above. The disk's diameter is 10mm and the gap between them is 500μm. The flow until the rotational speed of 700rpm remains laminar, while further increment in either the rotational speeds or the dimension of the flow geometry can result in the onset of a turbulent flow. The present study focuses only on the laminar flow where both experimental and numerical methods are used for the clarification of the flow characteristics. A simple digital filtering technique is implemented into a conventional micro-PIV technique, in order to resolve a steep velocity gradient in the liquid layer, particularly in the region adjacent to the rotating wall. A commercial CFD software, STAR-CD, is used to obtain the numerical results for the incompressible, laminar flow. The results are compared with the experimental micro-PIV results. The experimental and numerical results are discussed to understand the characteristics of the flow fields, for various rotational speeds.

5.2 Experimental method

5.2.1 Rotating-disk apparatus

The rotating disk is placed in the housing, as schematically shown in Fig. 5-1. The rotating disk is made of stainless steel and it is 10mm in diameter and 1mm in thickness. Its surface is polish finished and painted in black to facilitate a proper PIV measurement. The disk is connected to a shaft of 4mm diameter. This shaft is driven by a DC motor whose rotational speed is controlled externally and can be increased up to 3000rpm.

The housing has a cylindrical inner shape with the diameter of 15mm. The inner surface of the housing is also painted in black, except for the surface of the glass window that is used for the observation and illumination during the experiment. The gap between the upper surface of the rotating disk and the lower surface of the glass window can be varied; it is 500μm in the present study. A great attention is paid to make the two surfaces parallel with each other. The housing is filled with distilled water, which is seeded with 3μm-diameter spherical fluorescent particles. The water layer in the gap is the target of the present measurement. All the experiments are carried out at the room temperature (about 20°C) and atmospheric pressure (about 1×10^5Pa).

5.2.2 Micro-PIV setup

Figure 5-2 shows the schematic diagram of the present micro-PIV system. It consists of a double-pulsed Nd:YAG laser, a time-delay generator, a microscope with an air immersed objective, a CCD camera, and a personal computer for image acquisition. The beam emitted from the Nd:YAG laser (λ=532nm) is guided through an optical fiber to the illumination port of the microscope. A neutral-density (ND) filter is used to attenuate the laser beam power. The laser beam guided to the objective illuminates the liquid layer through an air immersion objective of 5× (*NA*=0.14) or 10× (*NA*=0.28). These objectives have long working distances of 34.0mm and 33.5mm, respectively. The flow is seeded with fluorescently-dyed 3μm-diameter polystyrene spherical particles. Their excitation and fluorescent wavelength are 542nm and 612nm, respectively. The fluorescent light emitted from the particles is collected by an interline-transfer CCD camera that has the spatial resolution of 1600×1200 pixels and the

intensity resolution of 10 bits. Although this interlined-transfer CCD has a low level of dark-current noise, the use of 3μm-diameter particles, which are larger than those (say, 1μm in diameter) used in typical micro-PIV measurements, is needed to achieve good visibility in the present measurement where the objectives with relatively low *NA* are used. A long-pass filter whose cut-off wavelength is 580nm is placed in front of the CCD camera, so that the background reflection of the excitation laser beam is filtered out.

The time interval between the two laser-pulses is varied from 0.1ms to 0.8ms, depending on the rotation speed of the disk. The present fields of view are 2.4mm×1.8mm and 1.2mm×0.9mm for the 5× and 10× objectives, respectively. The position of the focal plane in the liquid layer is adjusted by a 3-D traverse system that is installed below the rotating-disk apparatus. The spatial resolution of this positioning is ±1.5μm. The radial position of each measuring domain is also controlled by this 3-D traverse system. The acquired PIV images are analyzed by using the PIV software that is based on the direct cross-correlation algorithm. The size of the interrogation window is 90×90 pixels, with a 50% overlap. It yields the spatial resolution of 132μm. Although this interrogation window size is larger than the standard ones (32×32 pixels or 64×64 pixels), it is chosen by the fact that the present flow field does not vary steeply in the radial or tangential direction, even if it does vary steeply in the DOF direction. For ensemble averaging, 100 instantaneous velocity maps are generated from 200 PIV images acquired during the experiment.

5.2.3 Digital filtering technique

The DOF is studied previously by Meinhart et al (2000), who proposed the following expression:

$$DOF = \frac{3n\lambda}{NA^2} + \frac{2.16nd_p}{NA} + d_p \tag{5.1}$$

where n is the refractive index of the medium in front of the objective, λ is the wavelength of the illumination light in the vacuum, d_p is the diameter of tracer particle,

and *NA* is the numerical aperture of the objective. After substituting the values corresponding to the study, in the Eq. (1), (i.e., n=1.0, λ=0.612μm, d_p=3μm, *NA*=0.14 and 0.28), the DOF comes out to be 143.0μm and 49.6μm for the 5× and 10× objectives, respectively. These values are very large if compared to the thickness of the liquid layer, which has steep velocity gradients.

In order to reduce the DOF, and thus to improve the spatial resolution, a simple digital filtering technique is implemented. As demonstrated by Bourdon et al. (2004), the filtered particle images can lead to a substantial reduction of DOF, if the filter is designed appropriately. For the present measurement, a conventional high-pass filtering is found to work well. The cutoff frequency is chosen to be f_{cutoff}=0.1 pixel^{-1}. Its inverse (10 pixels) is two to three times larger than the size of the individual, in-focus particle images (Fig. 5-3). The high-pass filter is obtained from the desired frequency response by using the frequency sampling method (Lim. 1990). The desired frequency response, $H(f_x, f_y)$, can be expressed as follows:

$$H(f_x, f_y) = \begin{cases} 0 & f < f_{cutoff} \\ \\ 1 & f \geq f_{cutoff} \end{cases} \tag{5.2}$$

where $f = \sqrt{f_x^2 + f_y^2}$, and f_x and f_y are the horizontal and vertical frequencies, respectively. As shown later, this high-pass filtering can substantially improve the measurement near the rotating disk where the large velocity gradient in the DOF would cause a bias in the measured velocity. Figure 5-3 shows the original (unfiltered) and filtered particle image in an interrogation window. From here, it is evident that the in-focus particle images (i.e., smaller and brighter ones) are enhanced, while the out-of-focus particle images (i.e., larger and obscured ones) are attenuated. The effect of this digital filtering on the velocity measurement is presented in more detail later in this paper.

5.3 CFD method and grid system

The numerical simulations in this study are carried out by using the commercial software STAR-CD. It solves the three-dimensional, incompressible, laminar Navier-Stokes equations by finite volume method. The SIMPLE method is chosen for the pressure-velocity coupling and the algebraic multi-grid solver is used for the velocity and pressure corrections.

All spatial discretizations are carried out by using the standard, second-order, central-difference scheme. The entire flow domain, shown in Fig. 5-1, which consists of the gap between the disks and the annular region between the rotating disk and the housing, is discretized into a grid system having 3 million O-type hexahedral cells. The calculations are done on a Pentium 2.4GHz, single processor machine. It took around 10 hours to complete the calculation for one rotational speed case.

As for the boundary conditions, all the solid surfaces, including that of the rotating disk, are assumed to have no-slip condition. The convergence of the calculation is checked by monitoring if the residual error during the calculation has reached below 10^{-4}.

5.4 Results and discussion

5.4.1 Overall velocity profiles

Figures 5-4(a)~(c) represent the mean radial and tangential velocities (V_r and V_θ) for the rotational speeds of 300, 500, and 700rpm, respectively. The experimental and CFD results are plotted for z/H=0.2, 0.4, 0.6, and 0.8 where the velocities are non-dimensionalized by the tangential velocity of the disk edge, $R\omega$. Note that the 5× objective is used for this measurement and no digital filtering is applied here. The overall agreement between experimental and CFD results is good. For all the rotational speeds, the tangential velocities increase almost linearly with r, for r/R<0.9. Near the disk edge (i.e., r/R>0.9), however, they start to either decrease or increase non-linearly, depending on the rotational speed. The agreement between PIV and CFD results is not satisfactory here. The CFD results (not shown here) indicate that there exists a 3-D vortical motion in the outer peripheral region (i.e., r/R>1.0), and it does not appreciably

affect the flow field in the gap (say, $r/R<0.9$). A similar linear increment is also seen in the radial velocities. It should be mentioned that there is a slight misalignment (about 3 degrees) between the radial directions of the calculated flow field and that of the PIV measurement. It is corrected in the data analysis. In fact, this correction is clearly visible in the measured radial velocities, while negligible in the measured tangential velocities, as the large difference in their magnitudes. The radial velocities are positive for z/H=0.2 and 0.4, while they become negative for z/H=0.6 and 0.8; the negative value indicates the presence of a secondary flow, consisting of an outward flow near the rotating disk and an inward flow near the stationary disk.

The secondary flow is presented in more detail in Fig. 5-5 where the radial velocities are plotted as a function of z/H at r/R=0.20, 0.40, 0.60, and 0.88. The non-dimensionalized magnitude of the secondary flow increases with rotational speed, with a zero-crossing point at around z/H=0.48. The inward flow near the stationary disk is not desirable for the development of rotation-shearing chemical reactors, because it would hinder the reactant from flowing smoothly out of the reaction zone. The secondary flow affects the profile of the tangential velocities as shown in Fig. 5-6 where the tangential velocities are plotted as a function of z/H. While the profile is almost linear for 300rpm, as in a laminar Couette flow, it starts to become non-linear for the 500rpm and 700rpm, showing a steeper velocity gradient near the rotating disk. The flow fields for these rotational speeds remain laminar. It suggests that the assumption of the linear profile that is made often in such type of flows (e.g., Soo 1958) needs some modification.

5.2 Velocity profiles near the rotating disk

As for the overall profiles shown so far, the PIV and the CFD results are in fair agreement with each other. However, the agreement is found to deteriorate in the region near the rotating disk. It improves appreciably if the digital high-pass filtering technique (DHPF technique, hereafter) is applied to the acquired PIV images. As the micro-PIV technique is more efficient than the numerical technique for the parametric evaluation of the present flow field under various conditions, the deterioration and improvement of the agreement is analyzed in detail here.

Figure 5-7 shows the profiles of velocity magnitude measured near the rotating disk surface. The rotational speed is 500rpm. The results are plotted as a function of z/H on the logarithmic scale. It is recognized that the PIV results without using the DHPF technique, particularly those for r/R=0.6, starts to deviate from the CFD profile for z/H<0.1. This unreasonable profile is due to the DOF effect, as illustrated in Fig. 5-8 where the measuring domains at various distances from the rotating disk surface are depicted. If the measuring domain overlaps with the rotating disk, it will give a measurement that is lower than the true value that is defined at the central position of the domain. This deviation, therefore, becomes largest for the domain whose central position is located at the surface of the rotating disk. On the other hand, if the domain does not overlap with the rotating disk, little deviation occurs in the present, almost linear velocity profile. Also little deviation occurs in the region near the stationary disk where the magnitude of the velocity is small. In Fig. 5-7, the PIV results with the DHPF technique, for f_{cutoff} =0.05, 0.10, 0.15, and 0.20 pixel^{-1}, are included. It is seen that the PIV results with f_{cutoff}=0.10 and 0.15 pixel^{-1} are in good agreement with the CFD results, for all r/R shown here. The cutoff-frequency range is reduced to the cutoff-wavelength range of 6.7~10.0pixels. It should be noted that this cutoff-wavelength range is two to three times larger than the typical diameter of in-focus particle images as shown in Fig. 5-3.

Figure 5-9 shows a comparison among the PIV results for the 5× objective case (both with and without the DHPF technique (f_{cutoff}=0.1 pixel^{-1})), the PIV results for the 10× objective case (without filtering), and the CFD results at r/R=0.20, 0.36, and 0.60. The reasonable agreement between the filtered PIV results from the 5× objective and the unfiltered PIV results from the 10× objective suggests that the DOF is substantially improved by the use of the DHPF technique. It should be mentioned that the 5× objective provides a two times wider field of view than the 10× objective; and thus facilitating a more efficient evaluation of the rotation-shearing chemical reactors.

5.5 Conclusions

A strongly-sheared flow in the thin liquid layer between a pair of rotating and stationary disks, whose separation was 500μm, was studied experimentally and numerically with an objective to clarify the characteristics of the basic flow found in rotation-shearing chemical reactors. The micro-PIV technique was used to measure two-component velocities in the liquid layer. The commercial CFD software was used to provide data to compare and validate the micro-PIV results.

As for the overall velocity profiles in the liquid layer, the micro-PIV and the CFD results are in fair agreement; both are showing (1) the linear increase of tangential and radial velocities with radial position, and (2) the presence of a secondary flow that consists of an outward flow near the rotating disk and an inward flow near the stationary disk. This secondary flow is strengthened with the rotational speed and is responsible for the deviation of tangential velocity component from its linear profile in the direction of the thickness.

Measurement of near-wall from the present micro-PIV technique is appreciably improved by the use of a simple, digital, high-pass filtering technique that is applied to the acquired particle images. It is shown that the cutoff frequency of 0.1~0.15 pixel^{-1} (or cutoff wavelength of 6.7~10.0 pixels) works well with this technique. This cutoff wavelength is two to three times larger than the typical diameters of the in-focus particle images that are acquired in this study. It is demonstrated that the micro-PIV measurement with the high-pass filtering technique can provide detailed information about the flow field in the thin liquid layer between the rotating and stationary disks.

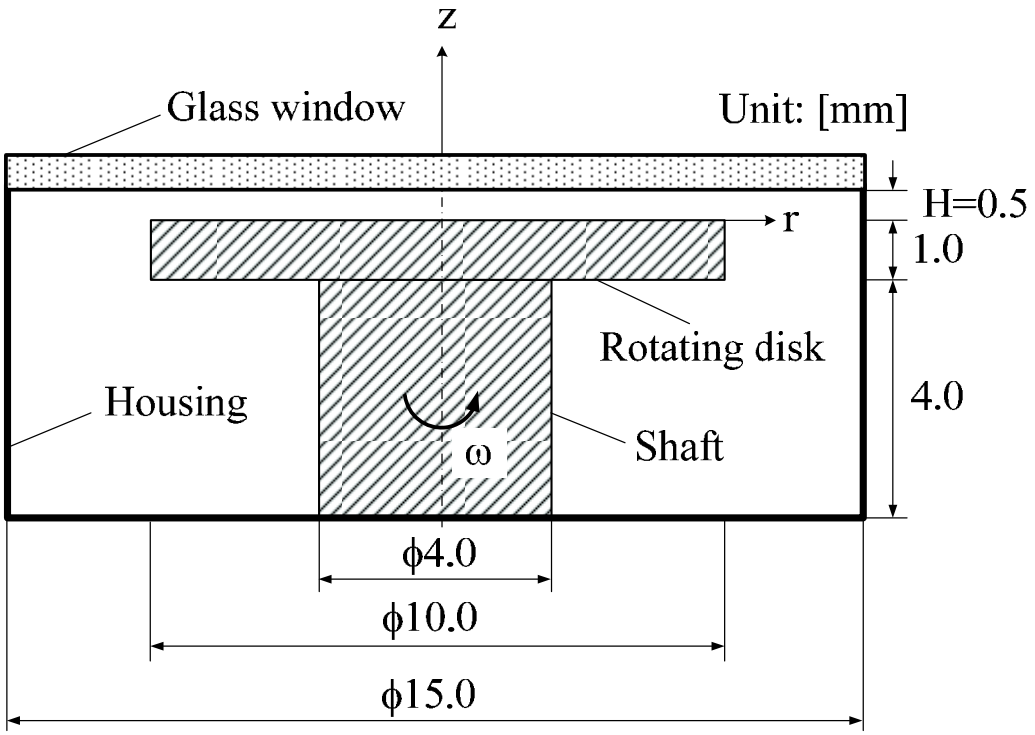

Figure 5-1 Schematic diagram of the rotating disk apparatus.

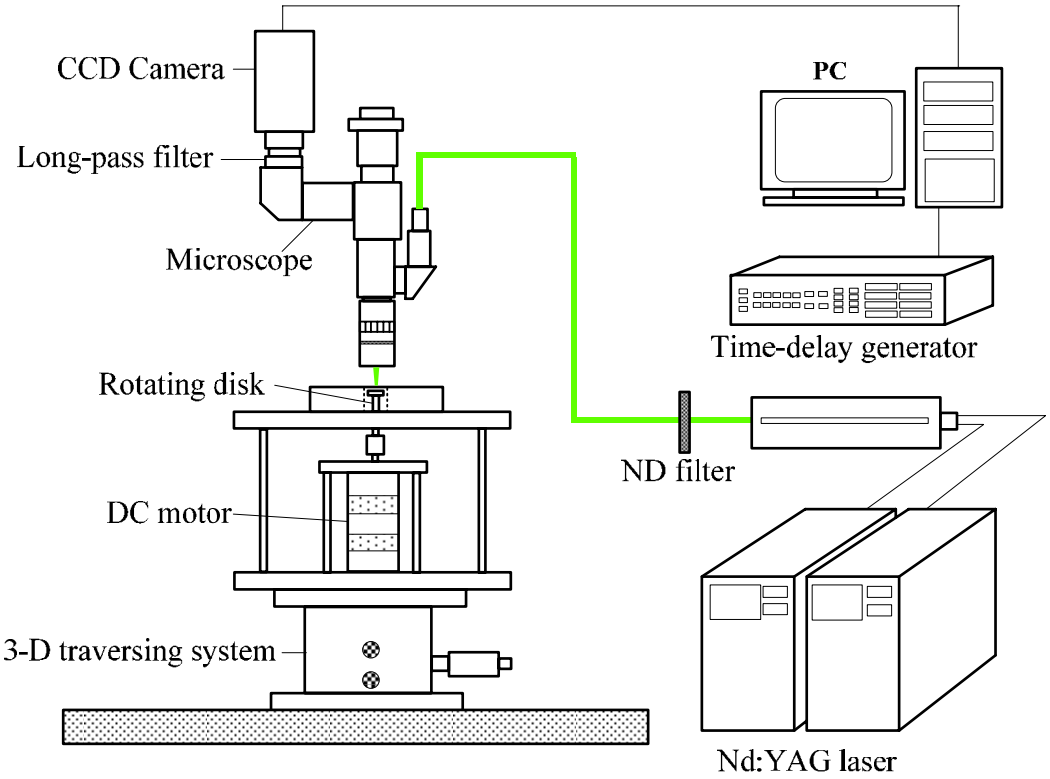

Figure 5-2 Schematic diagram of the present micro-PIV system.

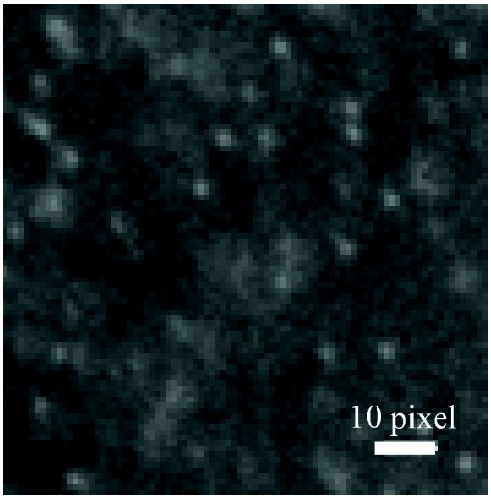

(a) Original particle image

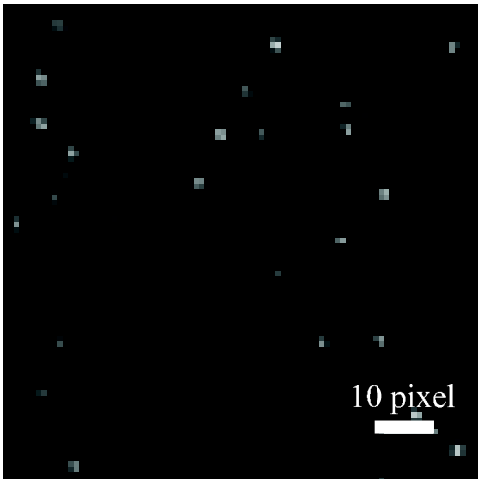

(b) High-pass filtered particle image

Figure 5-3　Original and high-pass filtered particle images in an interrogation window of 90×90 pixels in size.

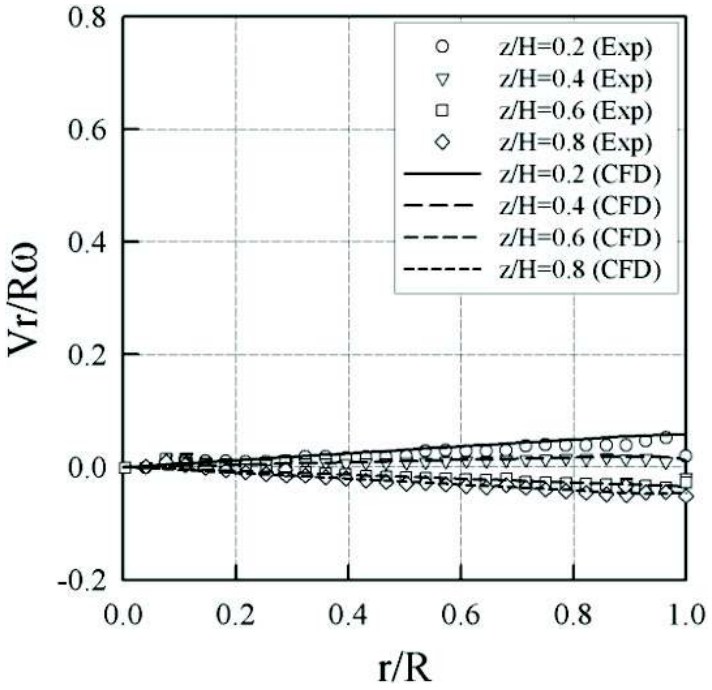

(a) Radial velocity

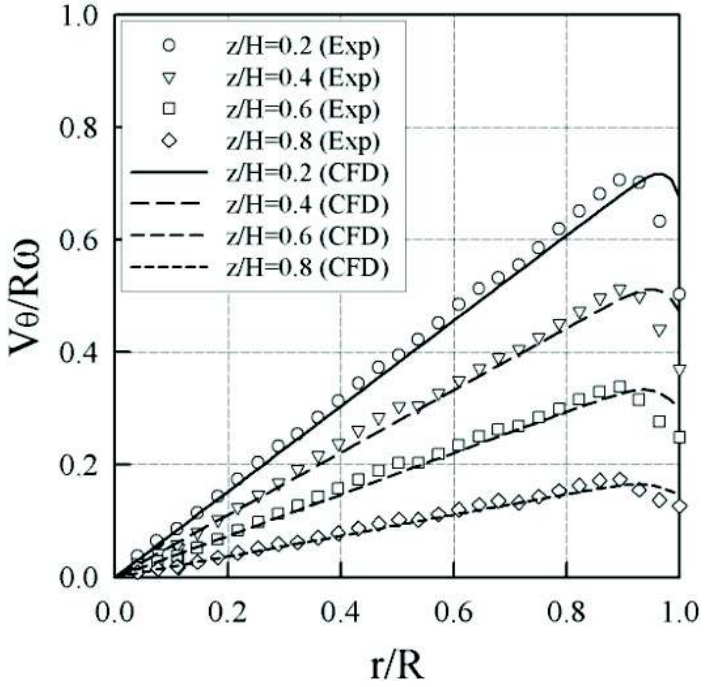

(b) Tangential velocity

Figure 5-4 Radial and tangential velocity profiles plotted as a function of r/R for rotational speeds of 300rpm (continue).

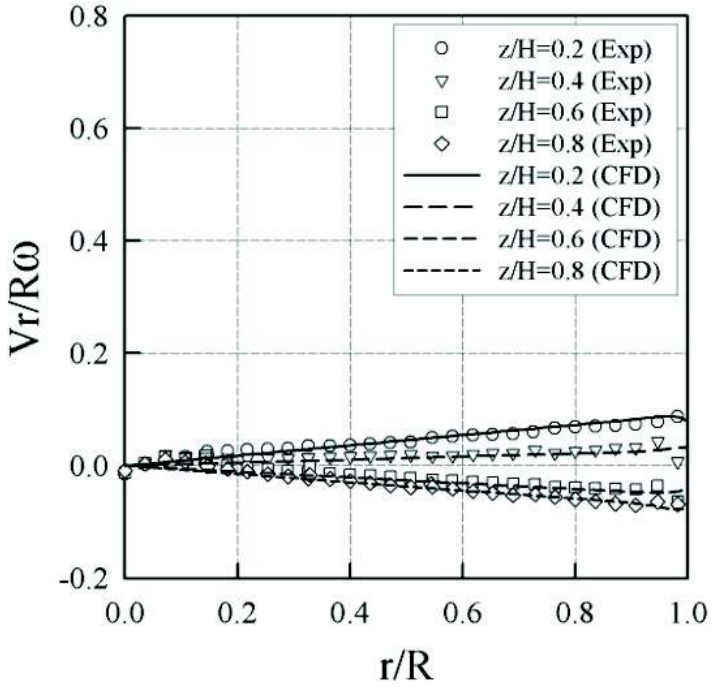

(a) Radial velocity

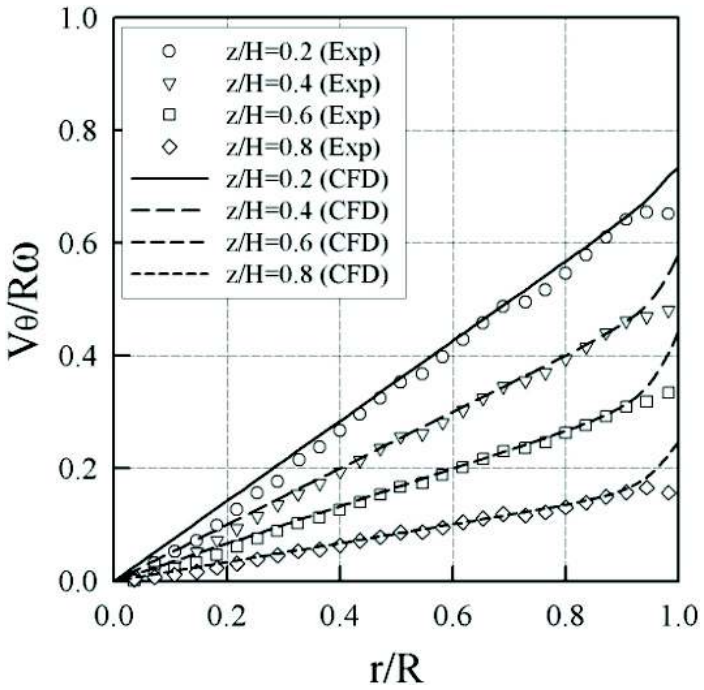

(b) Tangential velocity

Figure 5-4 Radial and tangential velocity profiles plotted as a function of *r*/*R* for rotational speeds of 500rpm (continue).

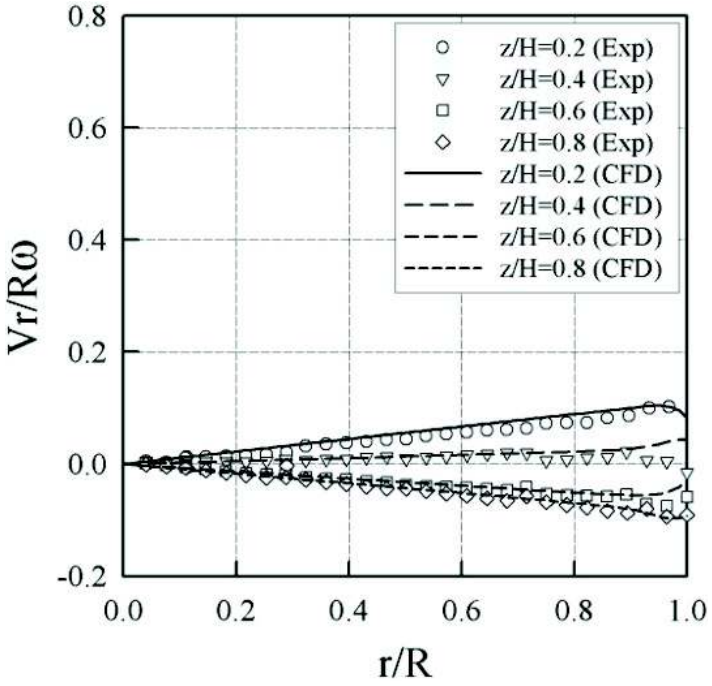

(a) Radial velocity

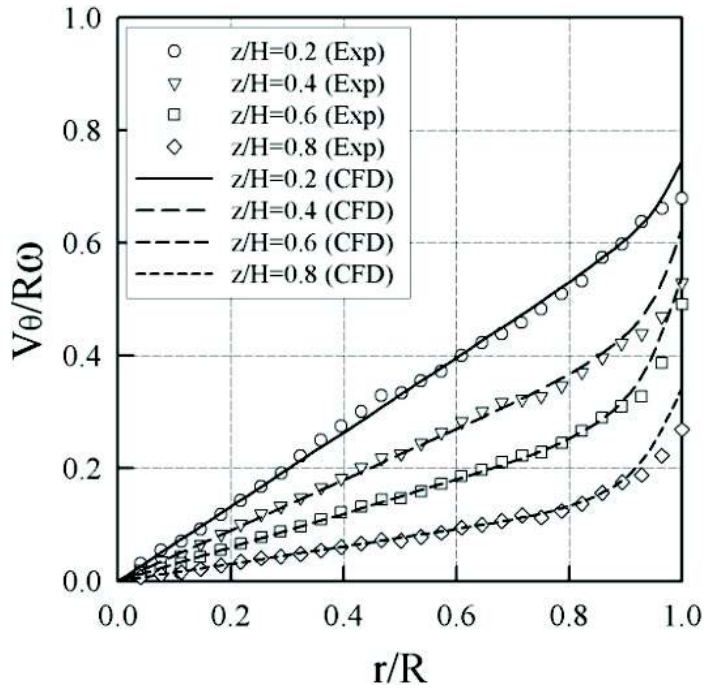

(b) Tangential velocity

Figure 5-4 Radial and tangential velocity profiles plotted as a function of *r*/*R* for rotational speeds of 700rpm.

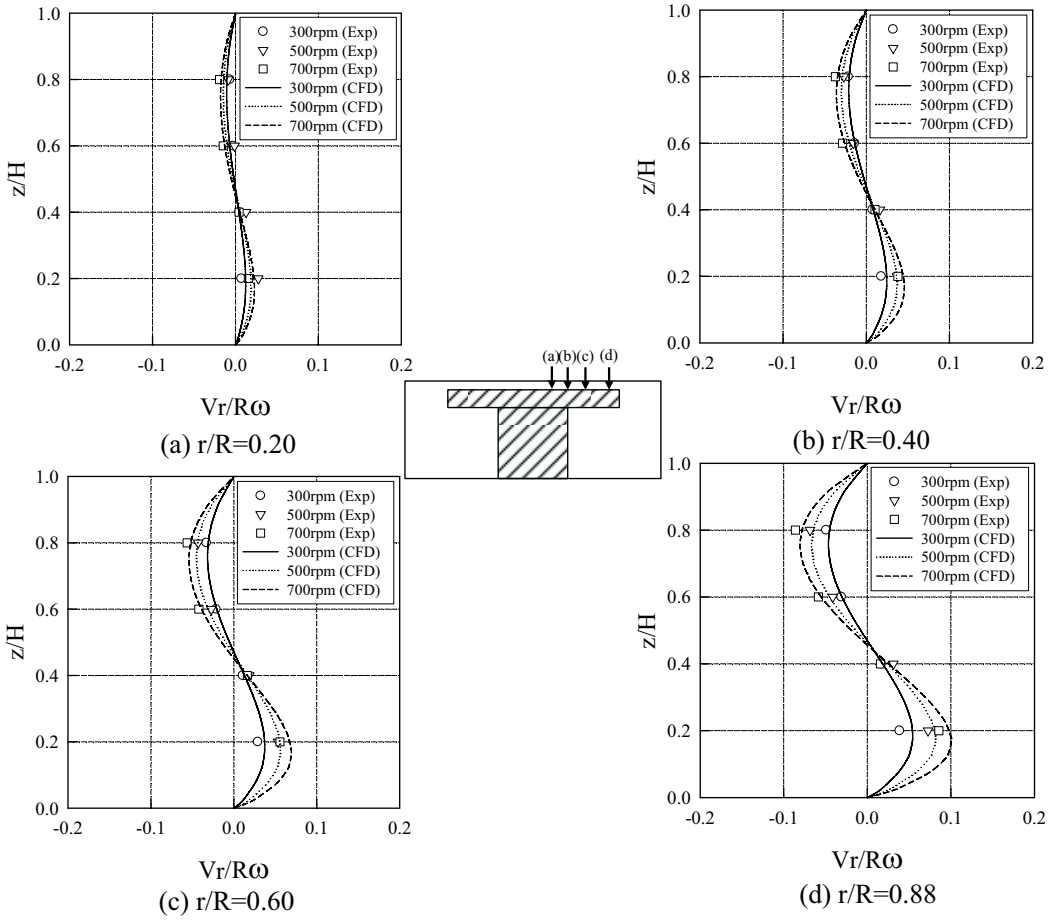

Figure 5-5 Radial velocity component plotted as a function of z/H.

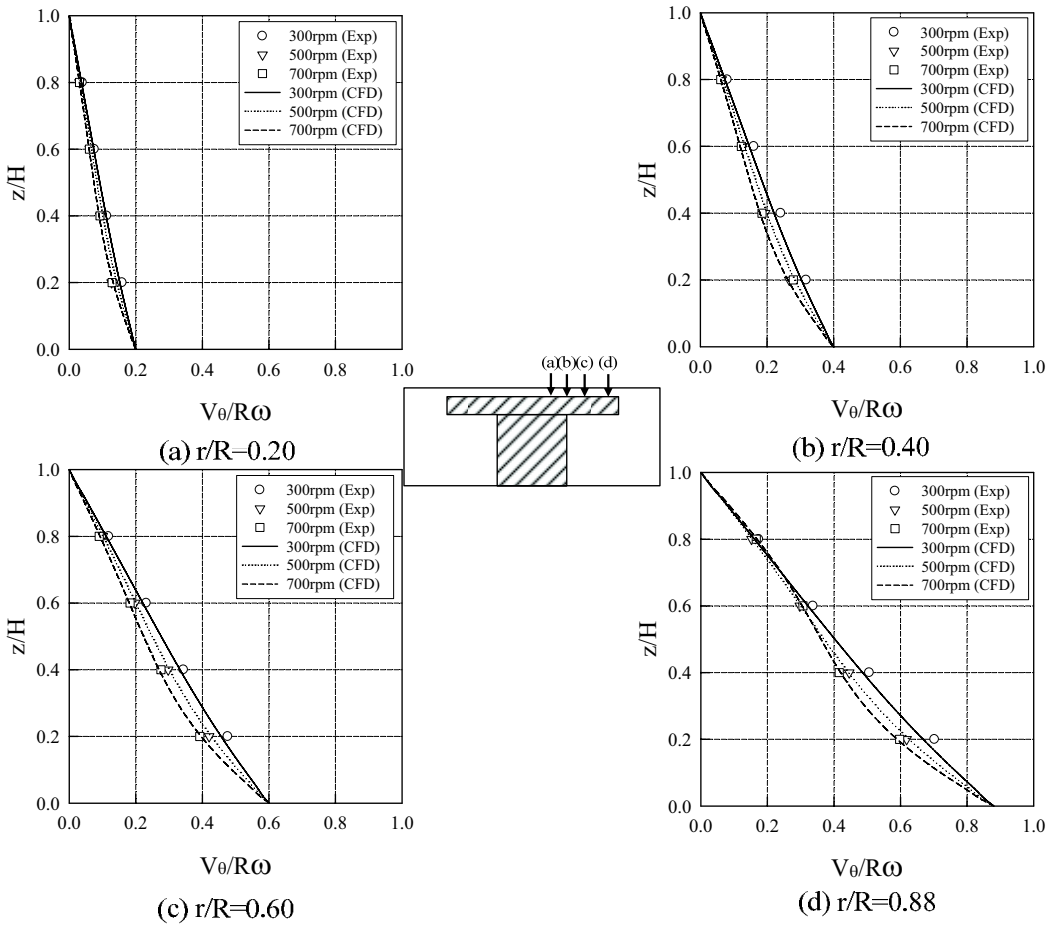

Figure 5-6 Tangential velocity component plotted as a function of z/H.

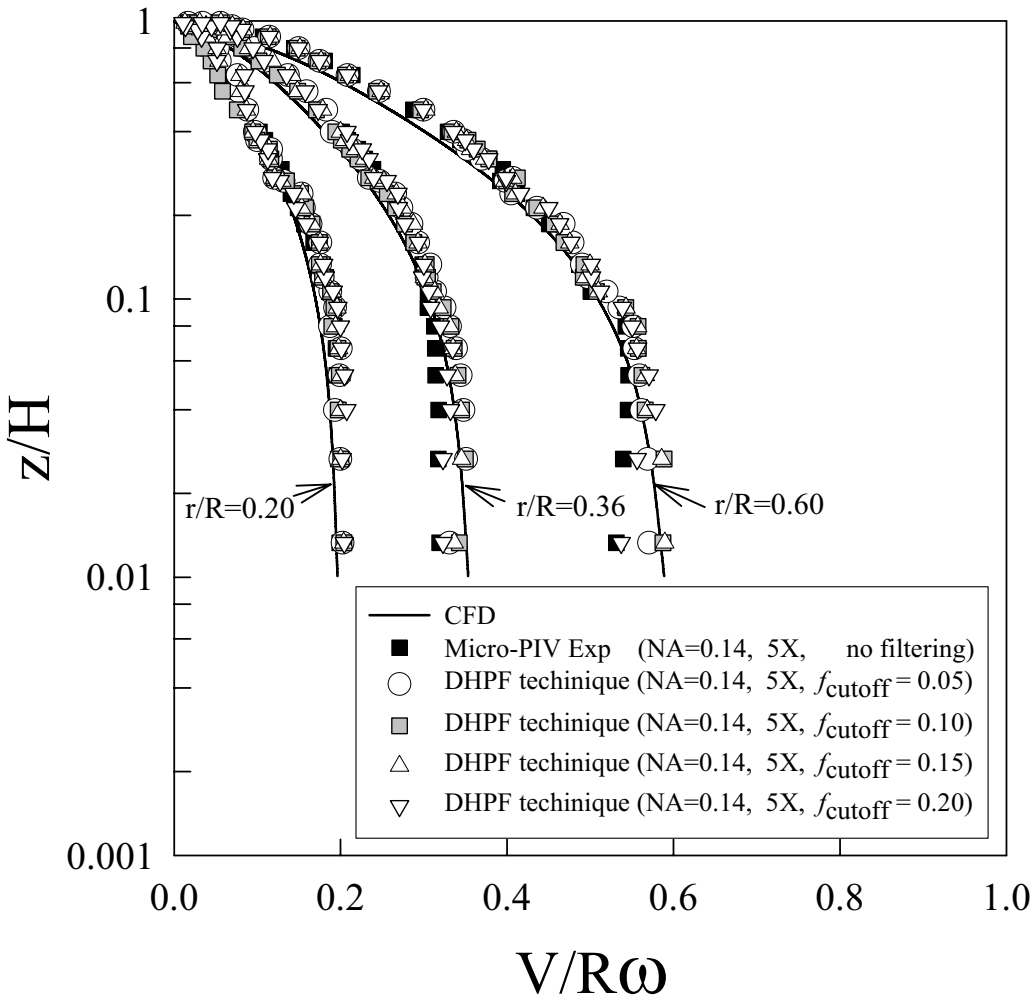

Figure 5-7 Velocity magnitude near the rotating disk surface at 500rpm

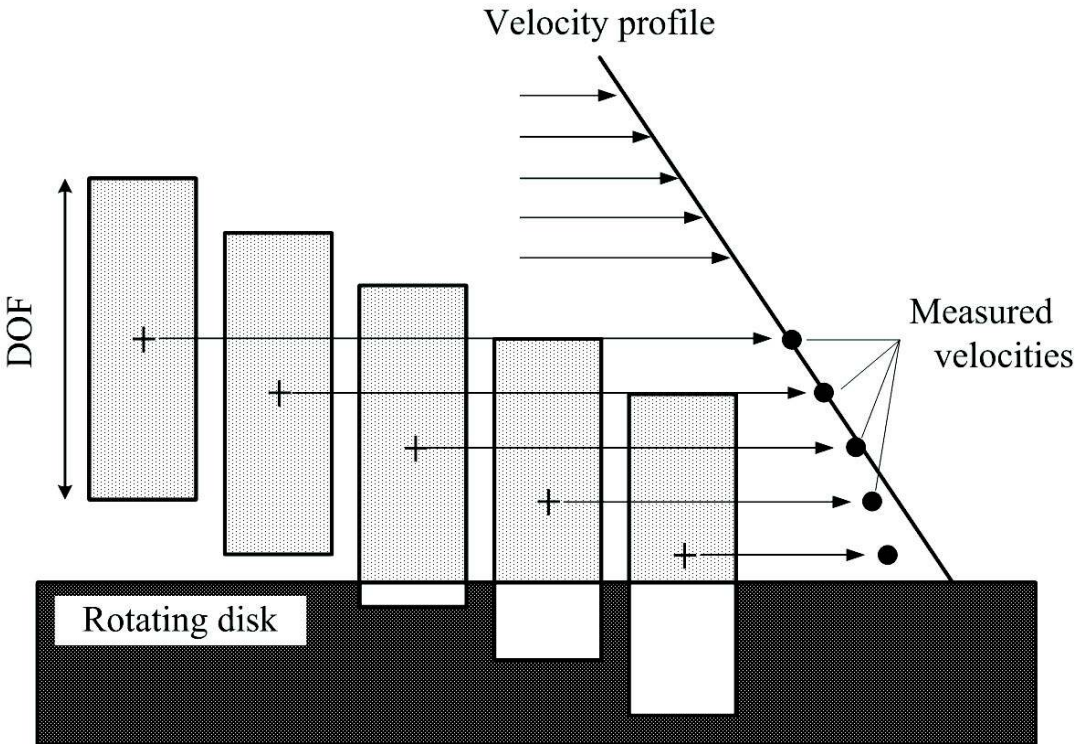

Figure 5-8 Effect of DOF on the measured velocities near the rotating disk surface.

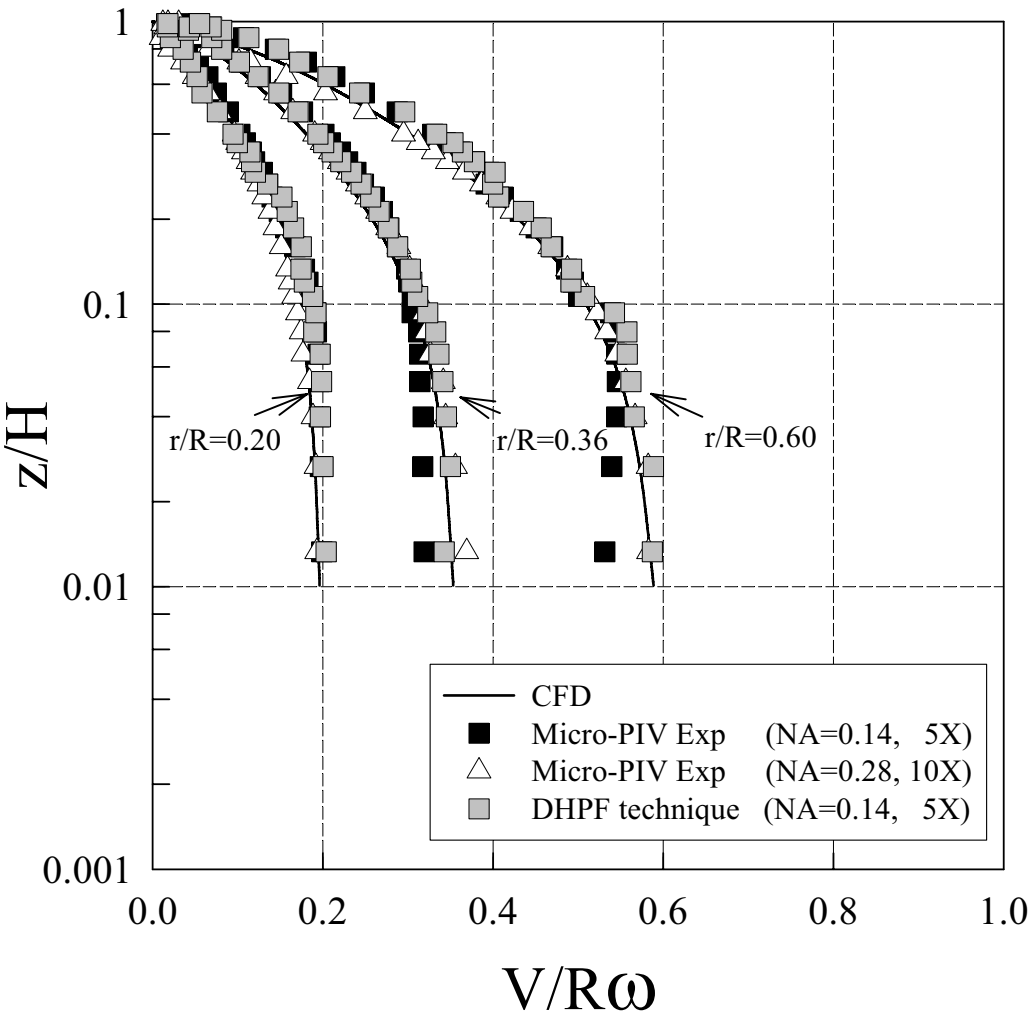

Figure 5-9 Comparison between the micro-PIV results using 5× objective, those using 10× objective, and the CFD results at 500rpm.

Chapter 6. Three-dimensional micro-PTV technique with stereoscopic viewing attachment

6.1 Background

Micro-scale flows have been receiving much interest from micro-electromechanical systems (MEMS) applications. However, conventional visualization techniques are not necessarily satisfactory for the visualization of micro-scale flows. In order to observe and measure complex flow phenomena in micro-scale, a suitable experimental technique that has a sufficient temporal and spatial resolution is needed (Lee et al. 2009). The PIV/PTV techniques are very powerful tools for obtaining velocity field information of various flows and they are advantageous if compared to other conventional point-wise velocity measurement techniques such as hot-wire anemometry and LDV. The PIV/PTV techniques have been applied to various industrial fields related to pharmaceutical (Reyes et al. 2002), electro-devices (Meinhart et al. 1998), and chemical reactors (Melin et al. 2004). The need for measuring three-dimensional (3-D) flows in microfluidic devices is rapidly growing in order to understand the basic physics behind the micro-scale flow phenomena.

Table 6-1 compares the basic capabilities of the 3-D micro-PTV techniques mentioned above. Note that only the techniques for three-dimensional, three-component (3D-3C) measurement are considered here.

Kim and Lee (2007) developed a holographic micro-PTV (HMPTV) technique to measure the temporal variation of 3-D velocity field of a micro-scale flow. This system was applied to measure instantaneous 3-D velocity vectors of flow in a micro tube with different particle number densities and flow rates.

Yoon and Kim (2006) developed a defocusing micro-PTV (DMPTV) method to detect 3-D particle positions in a 3-D volume of micro-scale flows using a calibration-based defocusing concept. They measured a three-dimensional flow in a micro channel having a backward-facing step.

Park and Kihm (2006) described a 3-D micro particle-tracking velocimetry technique that uses a single camera with deconvolution microscopy. This method tracks the line-

of-sight(s) flow vectors by comparing the outmost diffraction ring size of defocused particle images with computed point spread function. 3-D measurements of the flow over a spherical body were performed using this method.

In the present study, we propose a new compact stereoscopic micro-PTV system with a stereo optical attachment. The basic idea was presented previously by the authors (Lee et al. 2009). The attachment developed here has a higher capability for fine optical adjustment than the one presented previously. This micro-PTV technique is verified through a detailed measurement of 3-D flow in a thin liquid layer between rotating and stationary disks. This flow configuration is studied with a view to developing an active micro reactor that can achieve enhanced mixing and chemical reaction (Lee et al. 2011).

6.2 Experimental method

6.2.1 Stereoscopic micro-PTV setup

Figure 6-1 shows the schematic diagram of the stereoscopic micro-PTV system used in the present study. It consists of a high-repetition pulse Nd:YAG laser with 532nm wavelength, a microscope, a high-speed CMOS camera, a 5× air-immersed long-working-distance objective, a stereo optical attachment, a 3-D traversing system, and a personal computer for image acquisition. As shown in Table 1, this system provides a field of view of 1500×1000μm^2 and a depth-of-field of 300μm.

The important optics for stereo image is the stereo optical attachment, which is shown schematically in Fig. 6-2. It consists of a prism and two flat mirrors which are mounted in a compact cylinder and is fixed on the outer diameter of the objective. The stereoscopic viewing angle is designed to be 46 degrees. With this arrangement, two-separated stereo images from different angles can be obtained with a single high-speed CMOS camera.

In the experiment, the laser beam guided to the objective illuminates the liquid layer through the air-immersion 5× objective (NA=0.14). This objective has a long working distance of 34.0mm. The flow is seeded with fluorescently-dyed 7μm-diameter polystyrene spherical particles. Their excitation and fluorescent wavelength are 542nm and 612nm, respectively. The fluorescent light emitted from the particles is collected by

a high-speed CMOS camera that has a photodiode array of 1024×1024 pixels. The use of 7μm-diameter particles, which are larger than those (say, 1μm in diameter) used in typical micro-scale flowing measurements, is needed to achieve good visibility in the present measurement where the objective lens with relatively low *NA* is used. A long-pass filter whose cut-off wavelength is 580nm is placed in front of the high-speed CMOS camera, so that the background reflection of the excitation laser beam is filtered out.

A precision 3-D traversing system (1.5μm resolution) is used for accurate positioning of the rotating-disk apparatus. The radial position of each field of view relative to the axis of the rotating disk is adjusted by the 3-D traversing system. It is also used for the positioning and displacement of a calibration plate, which is placed in the liquid layer. Details of the stereo calibration are given below. The acquired PTV images are analyzed by using commercial PTV software. Its algorithm is the same as those reported by Nishino et al (1989). For PTV analysis, instantaneous velocity vectors are accumulated from 300 PTV images acquired during the experiment.

6.2.2 Rotating-disk apparatus

The rotating disk is placed in the housing, as schematically shown in Fig. 6-3. The rotating disk is made of stainless steel and it is 10mm in diameter and 1mm in thickness. Its surface is polish finished and painted in black to facilitate a proper PIV measurement. The disk is connected to a shaft of 4mm diameter. This shaft is driven by a DC motor whose rotational speed is controlled externally and can be increased up to 3000rpm.

The housing has a cylindrical inner shape with the diameter of 15mm. The inner surface of the housing is also painted in black, except for the surface of the glass window that is used for the observation and illumination during the experiment. The gap (*H*) between the upper surface of the rotating disk and the lower surface of the glass window can be varied; it is 250μm and 500μm in the present study. A great attention is paid to make the two surfaces parallel with each other. The housing is filled with distilled water, which is seeded with 7μm-diameter spherical fluorescent particles. The water layer in the gap is the target of the present measurement. All the experiments are

carried out at the room temperature (about 20°C) and atmospheric pressure (about 1×10^5Pa).

6.2.3 Calibration method

For the technique presented in this paper, an accurate stereoscopic camera calibration is needed. As shown in Fig. 6-4, a calibration plate is mounted on a high-precision z-axis traversing stage having a resolution of 0.5μm. The details of the calibration plate are given in Fig. 6-5. To achieve exactly the same optical path conditions, a water layer is generated between the calibration plate and the glass plate. Note that the glass plate is made of the same material and has the same thickness as the glass window of the rotating-disk apparatus. The calibration target is traversed stepwise in z-direction from -135μm to +135μm with an interval of 45μm, and an image needed for calibration procedure is acquired at each position. For example, Figure 6-6 shows the microscope images of the calibration plate and the fluorescent particles used in the measurement. Each image comprises left-view and right-view images, which are separated without overlapping with each other.

6.3 CFD method and grid system

The numerical simulations in this study are carried out by using the commercial software STAR-CD. It solves the three-dimensional, incompressible, laminar Navier-Stokes equations by finite volume method. The SIMPLE method is chosen for the pressure-velocity coupling and the algebraic multi-grid solver is used for the velocity and pressure corrections. All spatial discretizations are carried out by using the standard, second-order, central-difference scheme.

The entire flow domain, shown in Fig. 6-3, which consists of the gap between the disks and the annular region between the rotating disk and the housing, is discretized into a grid system having 3 million O-type hexahedral cells. The calculations are done on a Pentium 2.4GHz, single processor machine. It took around 10 hours to complete the calculation for one rotational speed case. As for the boundary conditions, all the solid surfaces, including that of the rotating disk, are assumed to have no-slip condition.

The convergence of the calculation is checked by monitoring if the residual error during the calculation has reached below 10^{-4}.

6.4 Results and discussion

6.4.1 Displacement measurement and measurement range

As a first check of the present technique, 3-D position and displacement of each calibration dot, such as shown in Fig. 6-6, is measured. The displacements given to the calibration dots are 20μm, 20μm and 25μm in x, y and z directions, respectively. The precision 3-D traversing system (1.5μm resolution) is used for this check. The uncertainties of the displacement measurement are shown in Fig. 6-7, where the mean deviations, δx, δy and δz from the given displacement in the respective direction are plotted as a function of z position of the calibration plate. The error bar for each data point represents twice the standard deviation of the measurements. It is seen that δx, δy and δz are quite reasonable (in other words, nearly zero) in the entire range of z positions examined here (i.e., the range from -100μm to +50μm). Judging from that the error bars are sufficiently small, it can be said that the non-zero value of each data point is caused by the inaccuracy of the traversing system.

As a second check of the present technique, the effective depth-of-field of the present measurement is evaluated by examining the number of measured velocity vectors. This velocity measurement is made by using fluorescent particles that are glued to the surface of a glass plate placed in the measuring volume so that the z-positions of the particles can be known from the z-position of the plate. The result is shown in Fig. 6-8, where the number of vectors obtained is plotted as a function of their z-position. It is seen that the maximum number is about 60 and it occurs at z=50μm. For larger or smaller z position, the number decreases almost linearly and it becomes a half of the maximum at z=-100μm and +220μm. This reduction is due to the deterioration of particle images caused by the out-of-focus effect. If the effective depth-of-field is defined as a range corresponding to the full width at half maximum in the number of vectors obtained, it would be 300μm in the present optical conditions. As this effective

depth-of-field is not large enough to cover the entire thickness of the water layer between the disks (i.e., 500μm), a set of two experiments, one is focused at z=125μm from the surface of the rotating disk and the other at z=375μm are done here so that the entire thickness is measured.

6.4.2 Velocity profiles in rotating liquid layer

Figure 6-9 shows a 3-D plot of the velocity vectors measured at a rotational speed of 300rpm in the radial range of $0.2 < r/R < 0.4$. The velocity vectors represent a rotational flow field in the thickness of the liquid layer. It is qualitatively recognized that the velocity magnitude increases with r, as is expected from this flow field. Figure 6-10 shows the mean radial and tangential velocities, V_r and V_θ, for the rotational speed of 500rpm. The data obtained by using a conventional 2D-2C PIV technique by Lee et al (2011) are included for comparison. All the results are plotted as a function of r/R at z/H=0.2, 0.4, 0.6, and 0.8, where the velocities are non-dimensionalized by the tangential velocity of the disk edge, $R\omega$ The agreement between the present 3D-3C data and the previous 2D-2C data is good for both tangential and radial velocities. The tangential velocities increase almost linearly with r, for r/R<0.9. Near the disk edge, however, they start to either decrease or increase non-linearly. Not shown here, these results near the disk edge are due to 3-D vortical motions that are present in the region between the disk edge and the side wall of the casing. The radial velocities also vary linearly, but their gradients are positive for z/H=0.2 and 0.4 while negative for z/H=0.6 and 0.8. This means that the flow fields in the liquid layer consist of an outward flow near the rotating disk and an inward flow near the stationary disk.

Figure 6-11 shows the comparison with the velocity vectors measured and CFD results at H=250μm, 500μm and a rotational speed of 500rpm. The present stereoscopic micro-PTV results suggested show good agreement when compared with CFD results

6.5 Conclusions

A stereoscopic micro particle tracking velocimetry (micro-PTV) technique has been developed by using a single camera with a stereo optical attachment. The attachment developed here is shown to have a higher capability of fine optical adjustment than the previous one proposed by the authors. This stereoscopic micro-PTV technique is validated through a three-dimensional measurement of a rotating flow in a thin liquid layer between a rotating disk and a stationary disk. This rotating liquid layer is 10mm in diameter and the gap between the disks is 500μm. The rotational speed examined is 500rpm. It is shown that the effective depth-of-field of the present technique is 300μm for the imaging optics using a 5× objective (NA=0.14). The measured velocities compare reasonably well with the previous results obtained with a conventional 2D-2C PIV technique.

Table 6-1. Comparison of the basic capabilities of the 3D micro-PTV

Method	Objective (*NA*)	Measurement Volume (μm^3)	Cell resolution (A) (μm/pixel)	Uncertainty in z-direction (B) (μm)	B/A (pixel)
Holographic	60× (1.10)	350 × 100 ×100	0.34	0.25	0.73
Defocusing	20× (0.40)	768 × 388 ×100	0.60	0.26	0.43
Deconvolution	40× (0.75)	165 × 93 ×25	0.16	-	-
Present	5× (0.14)	1500 × 1000 ×300	1.46	0.60	0.41

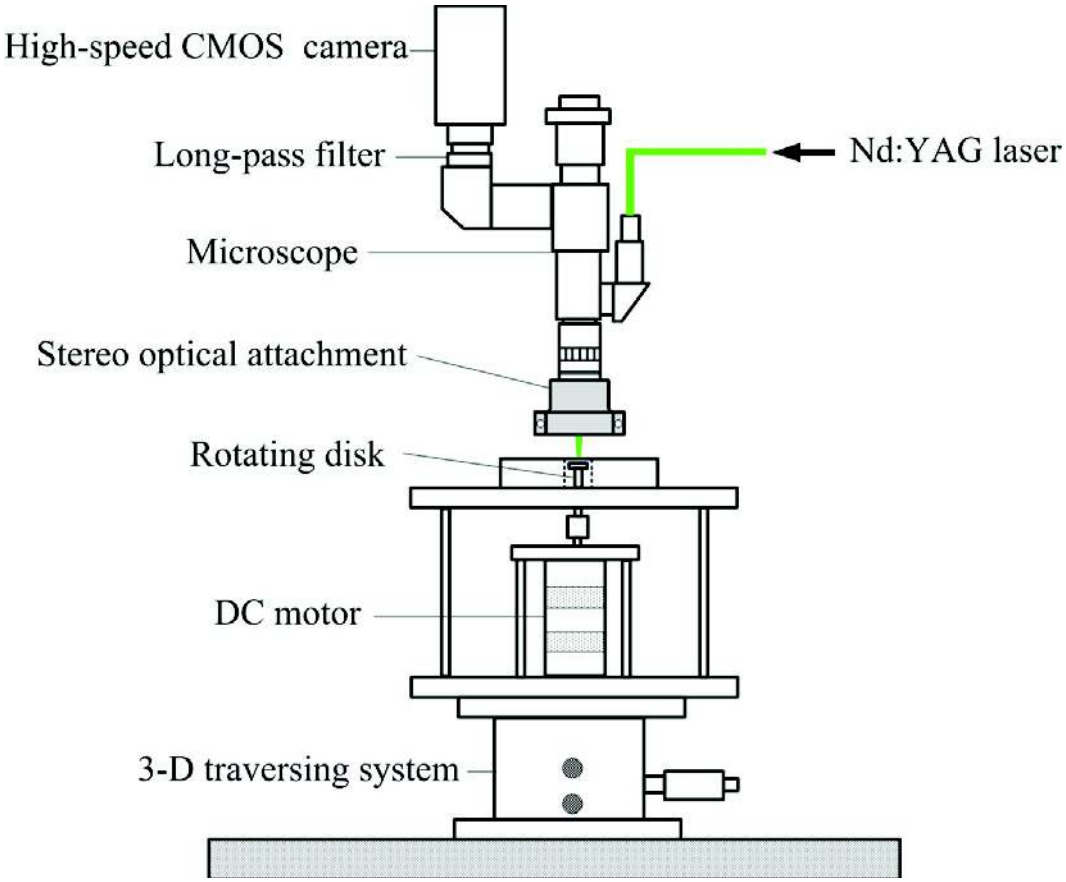

Figure 6-1 Schematic diagram of stereoscopic micro-PTV system.

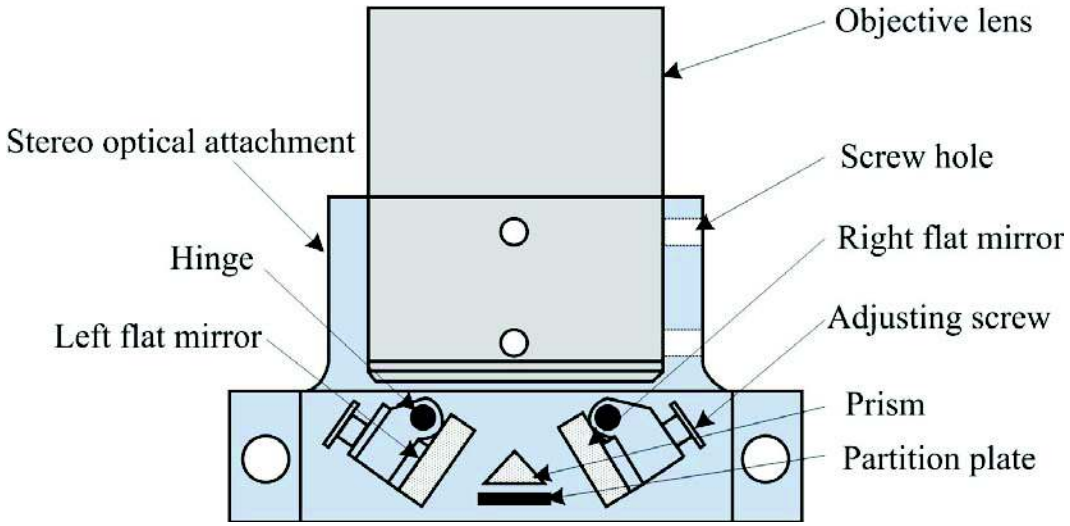

Figure 6-2 Schematic diagram of stereo optical attachment.

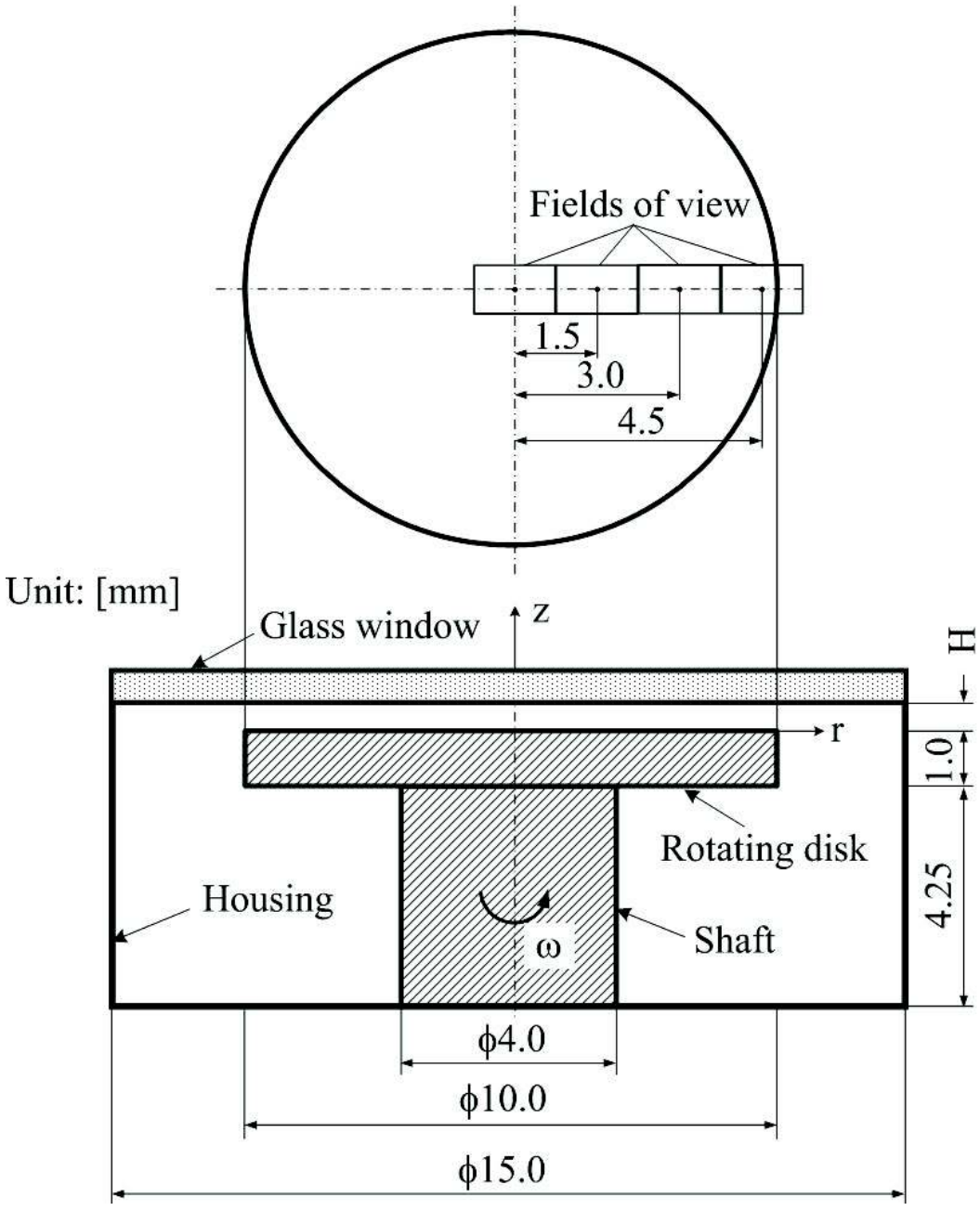

Figure 6-3 Schematic diagram of rotating-disk apparatus.

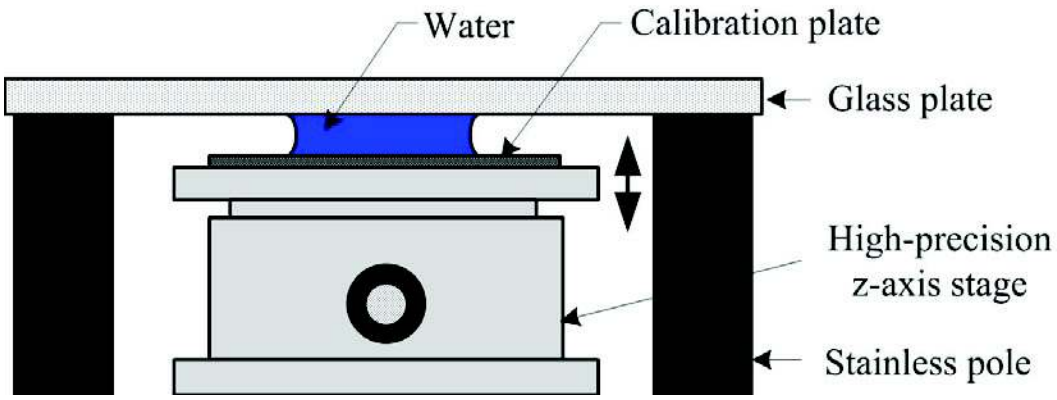

Figure 6-4 Calibration method.

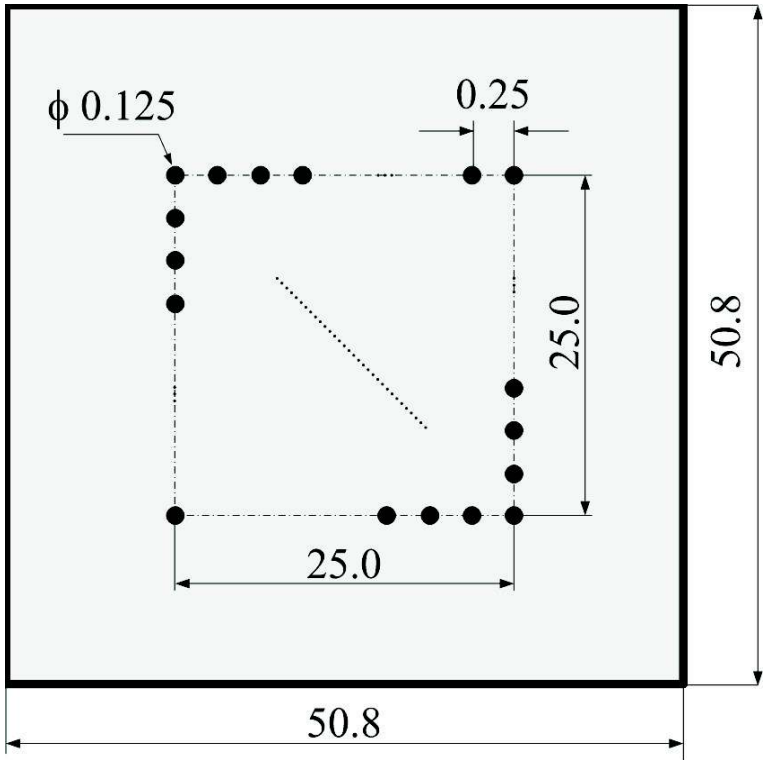

Figure 6-5 Calibration plate.

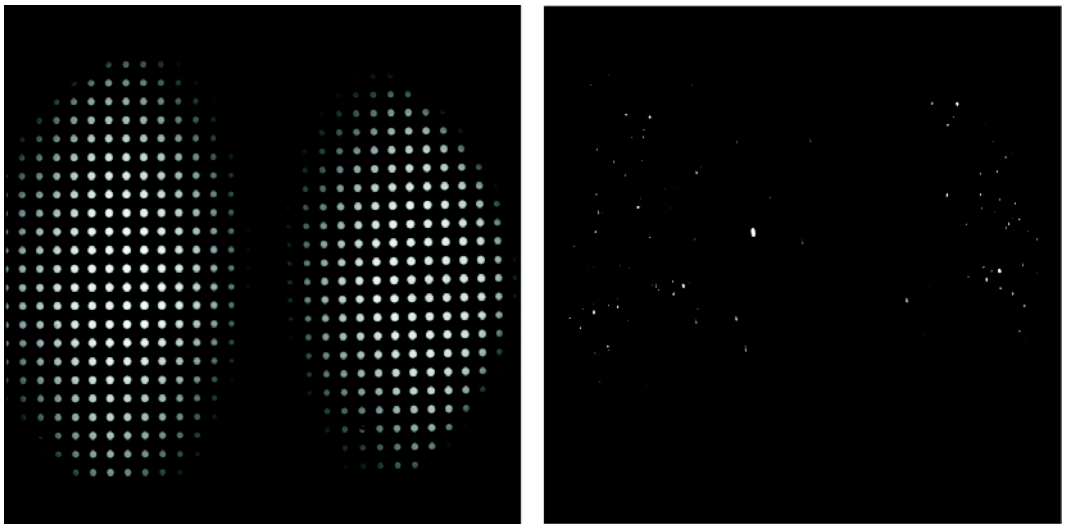

(a) (b)

Figure 6-6 Microscope image of (a) calibration and (b) fluorescent particle in 7μm diameter.

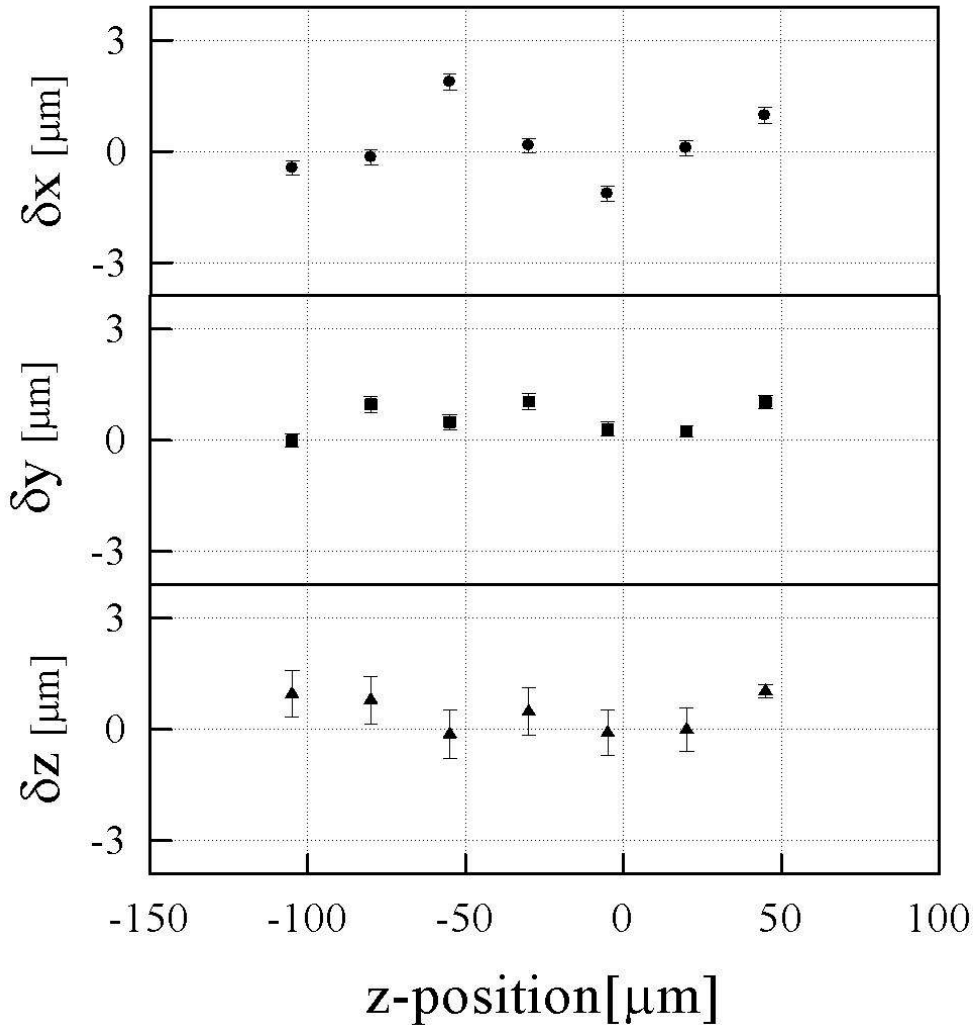

Figure 6-7 The measured displacements of translation (a) ~20μm in X (b) ~20μm in (c) ~25μm in Z.

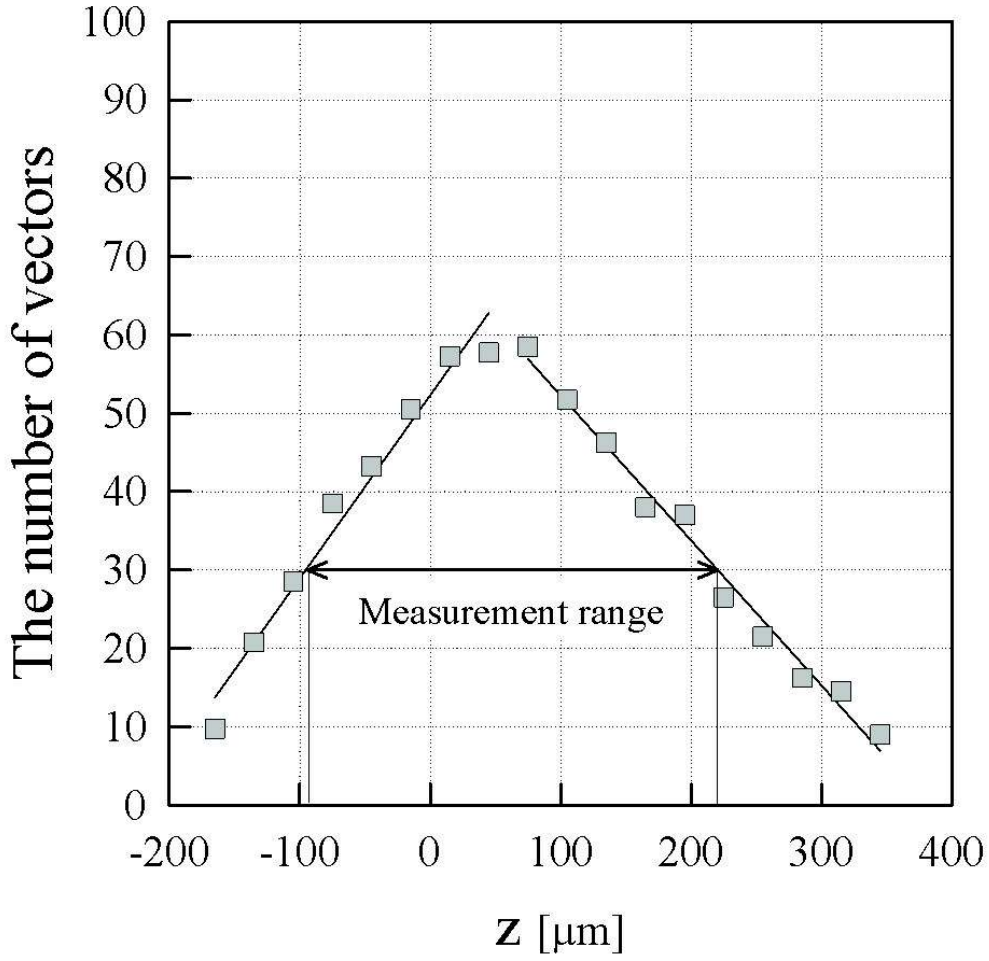

Figure 6-8 Measurement range in the depth direction.

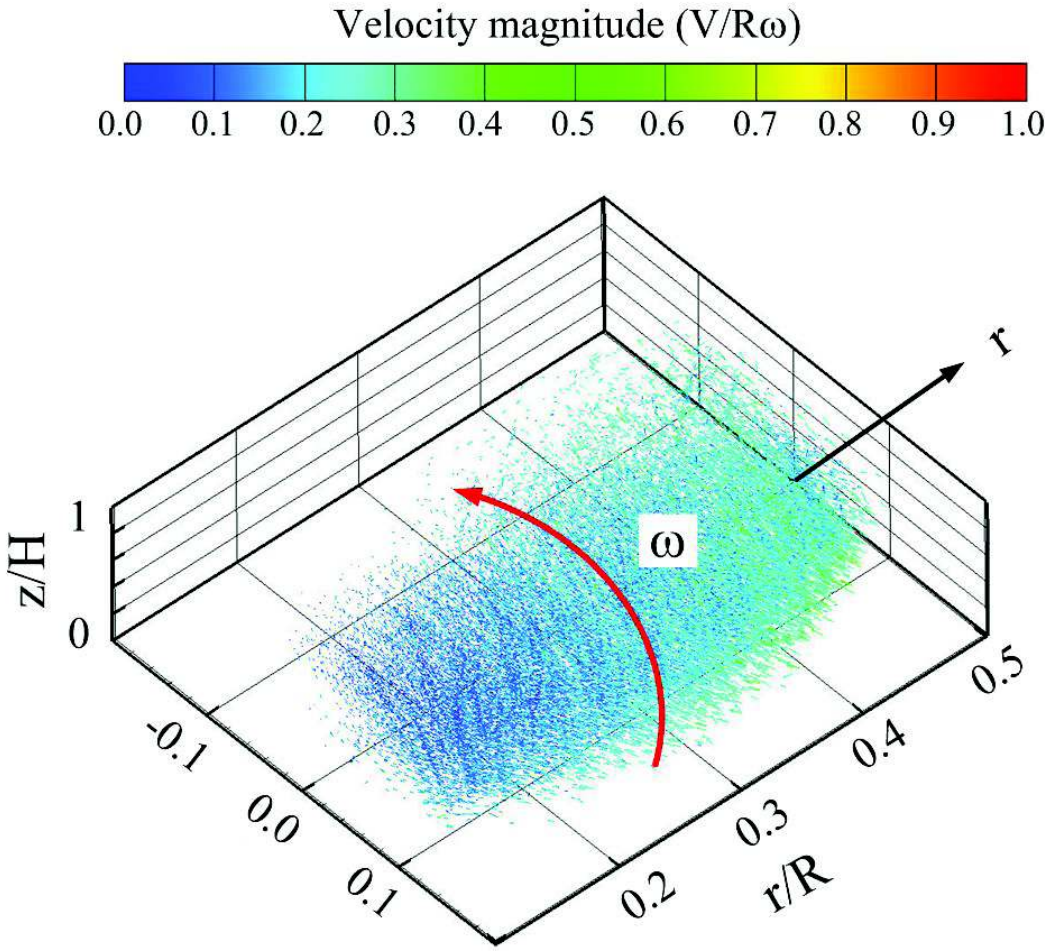

Figure 6-9 Three-dimensional plot of velocity vectors at a rotational speed of 300rpm.

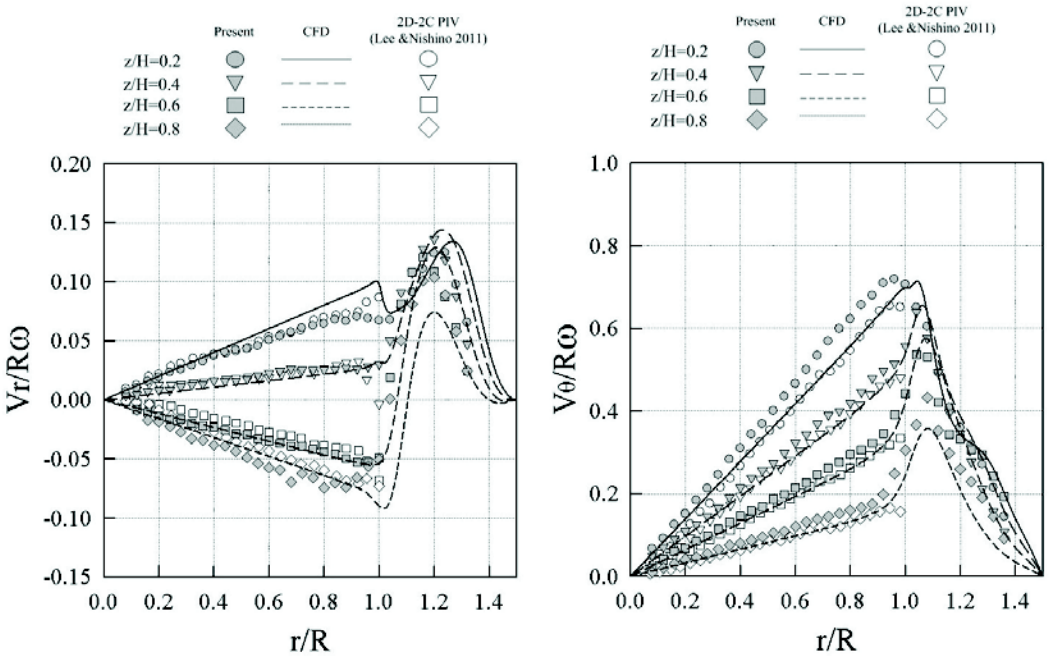

(a) H=500μm

Figure 6-10 Radial and tangential velocity profiles at various rotational-speeds (ω=500rpm) (continue).

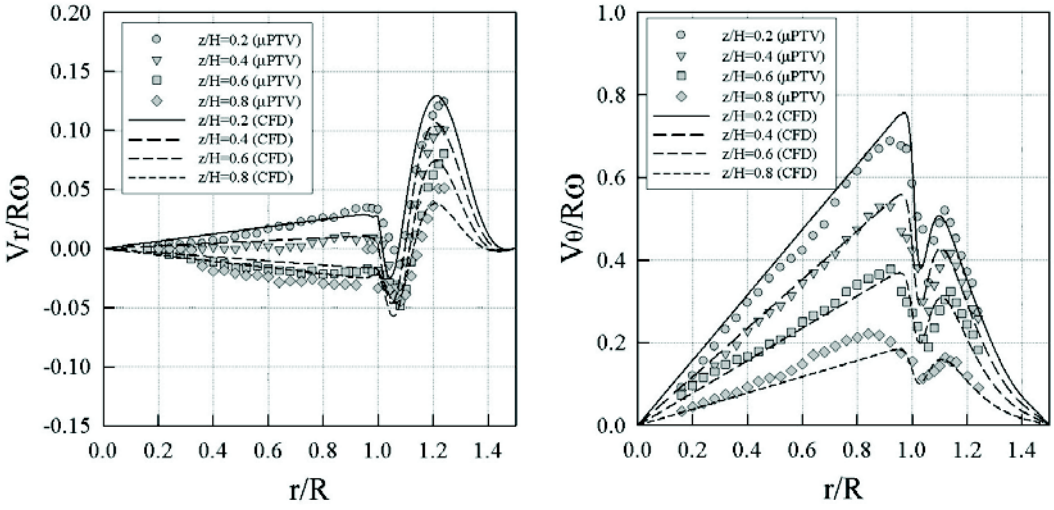

(b) H=250μm

Figure 6-10 Radial and tangential velocity profiles at various rotational-speeds (ω=500rpm).

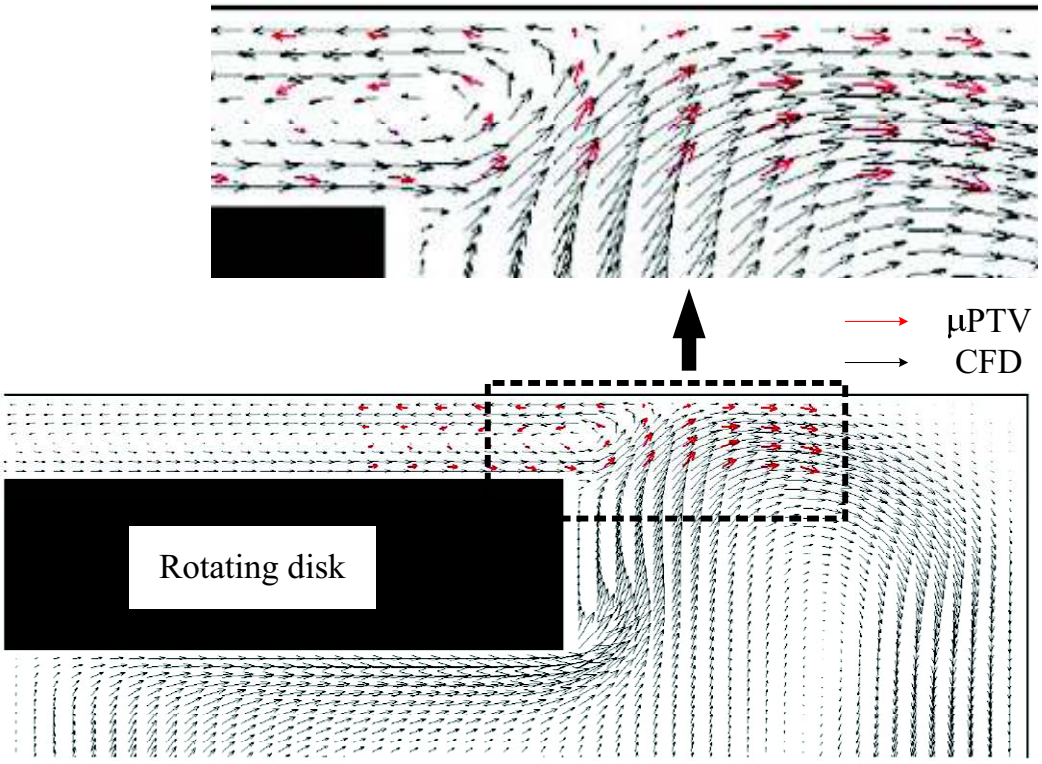

(a) H=500μm

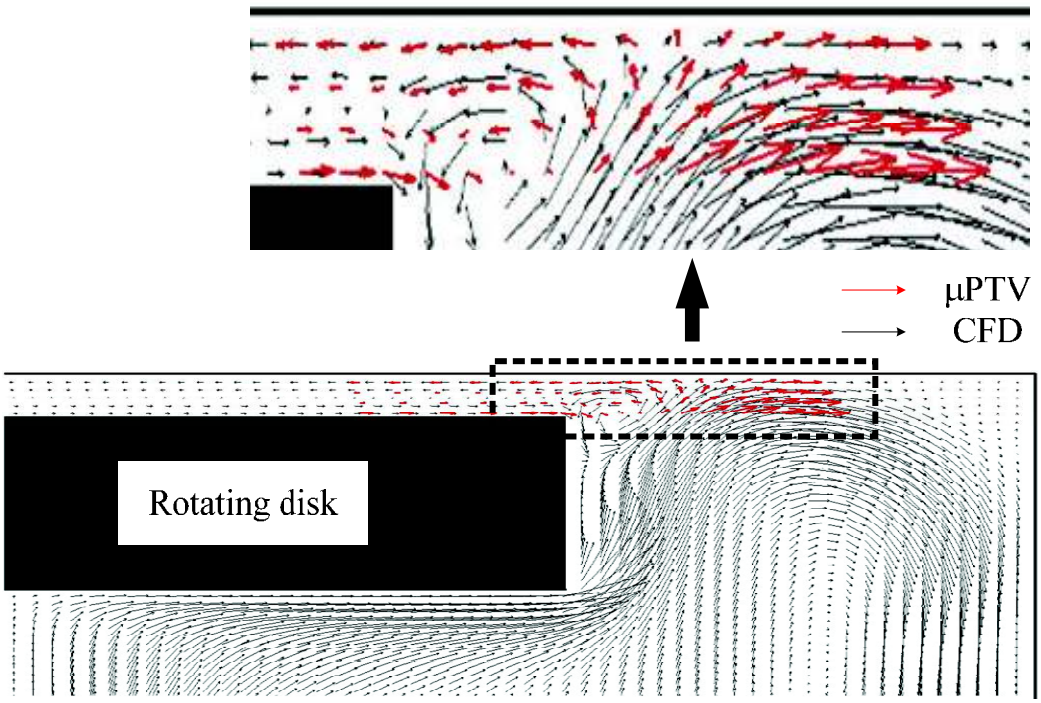

(b) H=250μm

Figure 6-11 Velocity-vector profiles near the edge of rotating disk (ω=500rpm).

Chapter 7 Empirical approach

The rotating-disk system has been used in many scientific and engineering applications. Examples are seen in turbomachinery (such as pumps and gas turbines), disk brakes of automobiles, rotating-disk air cleaners, systems of microclimate, extractors, dispensers of liquids, evaporators, circular saws, medical equipment, food process engineering, etc. Recently, particular attention is also paid to the rotation-shearing micro reactor that is under development for enhancement of mixing of chemical species.

In this rotation-shearing micro reactor, the friction torque caused by the shear stress due to the liquid flow in the gap between rotating and stationary disks is one of the most important design parameters because it determines the power loss and the heat transfer, both of which are strongly related to the flow in the gap. The induced flow depends on the geometries of the stationary and rotating disks, for example, the height of the gap between the disks, their radius, their rotational speed and so on.

In this chapter, an empirical expression is proposed to predict tangential velocity profiles and therefore tangential shear stresses in the laminar flow between rotating and stationary disks. If such information becomes available, we can calculate or estimate the rate of heat transfer that affects the rate of chemical reaction in the rotation-shearing micro reactor. First of all, we propose an equation for the following tangential velocities expressed as a function of z/H, r/R, and ω, as shown in equation (7.1).

$$\frac{V_\theta}{R\omega} = \left(\frac{a - \dfrac{z}{H}}{c + d\dfrac{z}{H}} \right)^n \cdot \frac{r}{R} \tag{7.1}$$

where a, b, d, and n are constant which are dependent on the internal flow.

The proposal of equation (7.1) is based on the assumption of a Couette flow without secondary flow between stationary and rotating disks. In fact, if a, c, and n are equal to 1 and d is equal to 0, the equation gives a velocity profile of Couette flow which refers to the laminar flow of viscous fluid in the space between two parallel disks.

The simplified equation is expressed as follows:

$$\frac{V_\theta}{R\omega} = \left(1 - \frac{z}{H}\right) \cdot \frac{r}{R} \tag{7.2}$$

This Couettee flow is driven by the viscous drag force acting on the fluid by the wall.

Figures 7-1(a), (b), 7-2(a), (b) and 7-3(a), (b) show the radial profiles of shear stress at stationary and rotating disks for H=100μm, 250μm and 500μm in the range of 100rpm to 700rpm. These figures compare the present CFD results with the profiles given by Equation (7.1). It is seen that the shear stresses, both at the stationary and the rotating disks, increase almost linearly with increasing r/R and with the rotational speed. Note that the shear stress is evaluated from the velocity gradient at the wall that are given from Equation (7.1).

From Figs.7-1 and 7-2, we can recognize that the shear stresses at stationary and rotating disks are quite similar in magnitude. Since the radial velocities in the gap are much smaller than the tangential velocities, as seen in Figs. 3-11a and 3-11b, the tangential velocities are not affected appreciably by the radial velocities and consequently the tangential velocities exhibit Couette-type linear profiles. The shear stresses for H=100μm are about two times larger than those for H=250μm.

However, Fig. 7-3 shows different characteristics. The shear stresses at the stationary and the rotating disks are not similar in magnitude as seen in Figs. 7-3(a) and (b). The magnitude at the rotating disk is consistently larger than that at the stationary disk, in contrast to Figs.7-1 and 7-2. This result for larger H is obviously due to the effect of the radial velocities to the tangential velocities as shown in Fig. 3-12c. This means that the Couette-flow assumption is not valid anymore for H=500μm (and probably for larger H) and for rotational speeds of 300rpm, 500rpm and 700rpm.

We have also found, as an important design criterion for rotation-shearing micro reactors, that the decrease of the gap between stationary and rotating disks, i.e., H, can decrease the magnitude of the secondary flow with respect to the magnitude of the tangential velocity. This feature may be used to suppress unwanted effect of the secondary flow (in other words, the reversal flow) that would otherwise cause duplicate reaction in the gap.

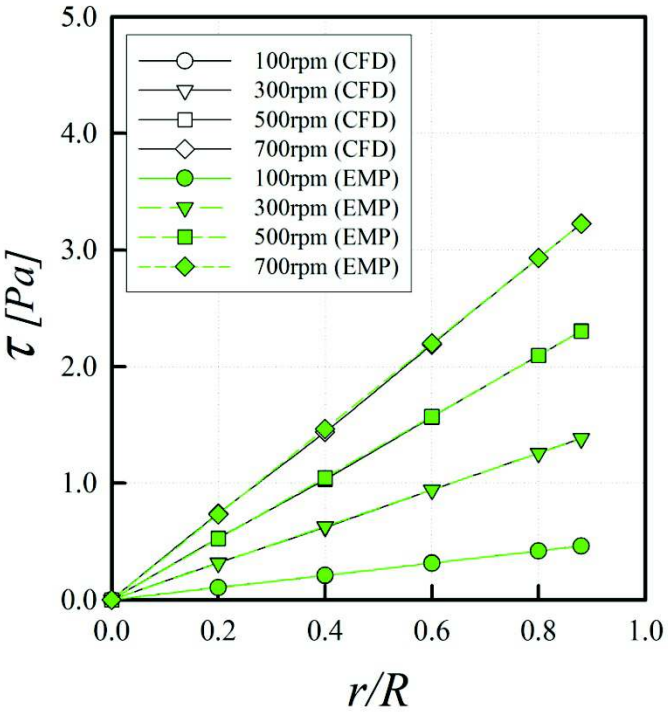

(a) stationary disk

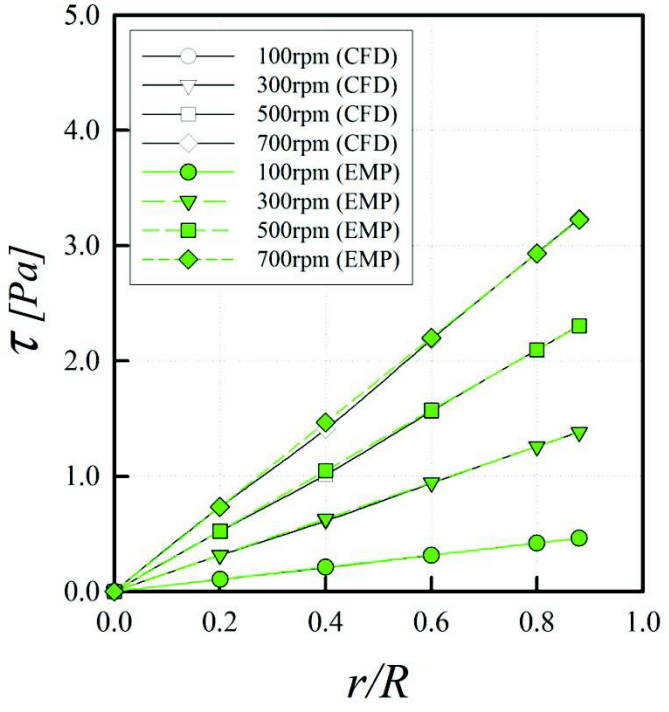

(b) rotating disk

Figure 7-1 Shear stress at stationary and rotating disks (H=100μm)

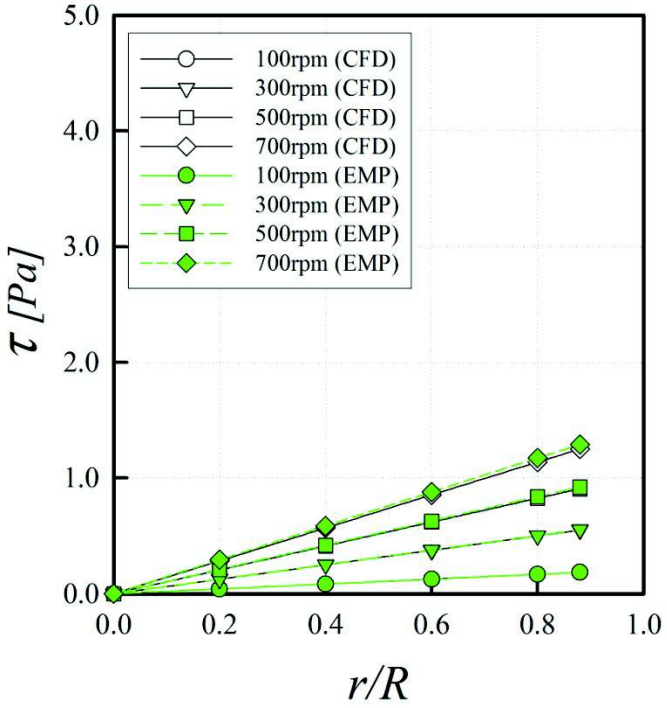

(a) stationary disk

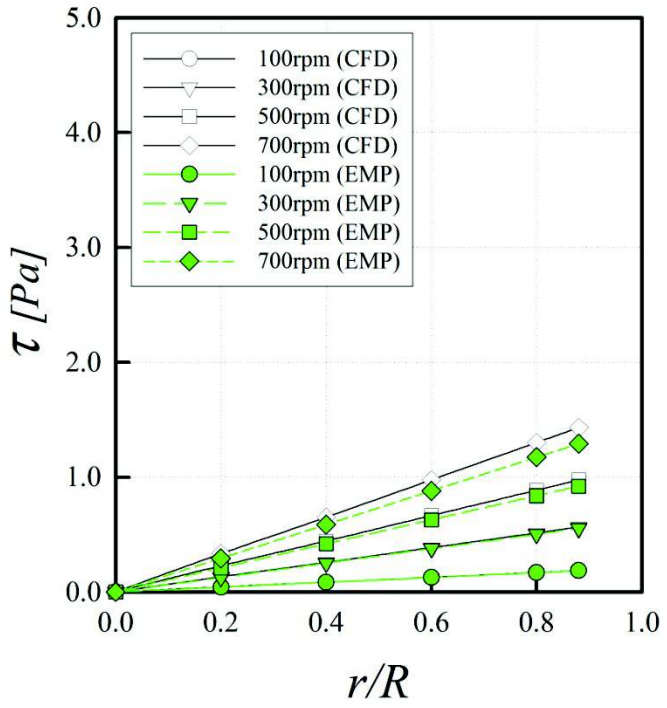

(b) rotating disk

Figure 7-2 Shear stress at stationary and rotating disks (H=250μm)

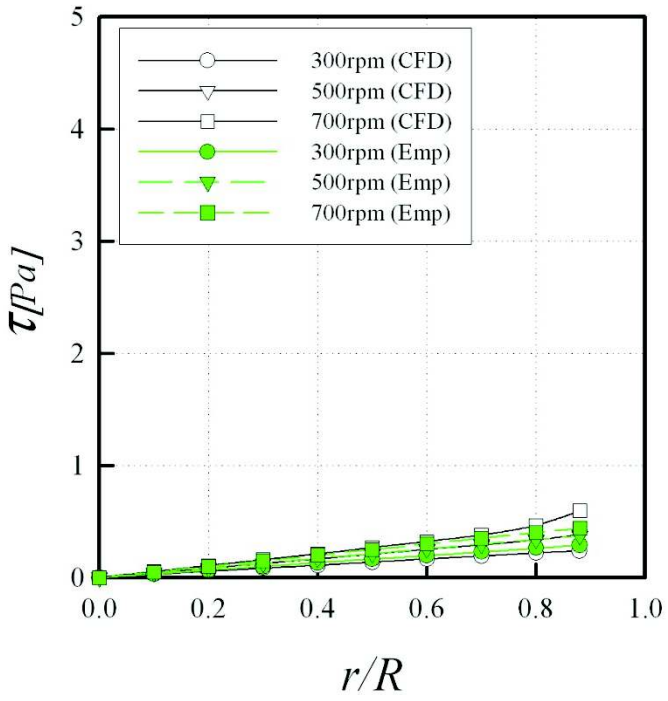

(a) stationary disk

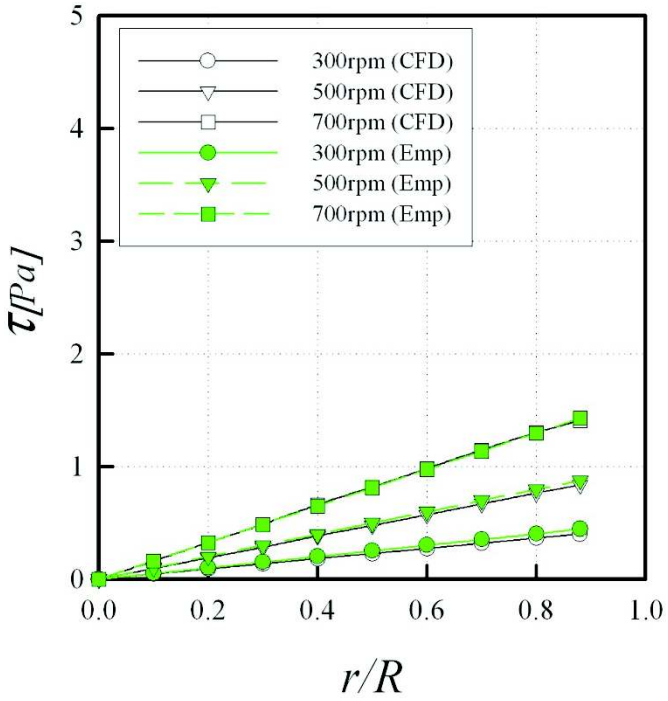

(b) rotating disk

Figure 7-3 Shear stress at stationary and rotating disks (H=500μm)

(This graph was made by the conditions of a=c=1.01, d=0.95, n=0.83 at 300rpm, a=c=1.00001, d=0.98, n=0.958 at 500rpm, and a=c=1.00001, d=1.3, n=0.96 at 700rpm in equation (7.1))

Chapter 8 Conclusions

The present study is intended to develop two/three dimensional PIV measurement technique. Such measurement techniques developed was applied to the micro rotation flow. In recent years, emerging in the field of micro-flow to the active micro-reactor can be applied. Each chapter can be summarized as follows:

In chapter 1, the detailed understanding of the flow inside the micro-scale passage is very important for their optimum design and active/passive control of flow with rapid development in MEMS technology. In order to observe the flow phenomena in micro-fluidics, a suitable experimental technique that can resolve the temporal and spatial resolutions of the given micro-scale flow is definitely needed so that two/three dimensional PIV technique was introduced.

In chapter 2, since the first micro-PIV experiment was carried out by Santiago et al (1998), micro-PIV measurement technique has been developed rapidly. This chapter was to provide the theoretical and technical methods to understand a micro-PIV system and technical technique.

In chapter 3, the numerical simulation was carried out by using the commercial software STAR-CD. It solves the three-dimensional, incompressible, laminar Navier-Stokes equations by finite volume method. The SIMPLE method is chosen for the pressure-velocity coupling and the algebraic multi-grid solver is used for the velocity and pressure corrections. The objective of this chapter is to be compared and validated with two/three-velocity components of micro-PIV and stereoscopic micro-PTV.

In chapter 4, digital image filtering was introduced in order to improve measure accuracy of near-wall flow from the present micro-PIV technique. Frequency sampling method was used to design a simple, digital, high-pass filter.

In chapter 5, the micro rotating flow between a pair of rotating and stationary disks, whose separation was 500μm, was studied experimentally and numerically with an objective to clarify the characteristics of the basic flow found in rotation-shearing chemical reactors. The micro-PIV technique was used to measure two-component velocities in the liquid layer. The commercial CFD software was used to provide data to compare and validate the micro-PIV results. As for the overall velocity profiles in the liquid layer, the micro-PIV and the CFD results are in fair agreement; both are showing (1) the linear increase of tangential and radial velocities with radial position, and (2) the presence of a secondary flow that consists of an outward flow near the rotating disk and an inward flow near the stationary disk. This secondary flow is strengthened with the rotational speed and is responsible for the deviation of tangential velocity component from its linear profile in the direction of the thickness. Measurement of near-wall from the present micro-PIV technique is appreciably improved by the use of a simple, digital, high-pass filtering technique that is applied to the acquired particle images. It is shown that the cut-off frequency of 0.1~0.15 pixel^{-1} (or cut-off wavelength of 6.7~10.0 pixels) works well with this technique. This cutoff wavelength is two to three times larger than the typical diameters of the in-focus particle images that are acquired in this study. It is demonstrated that the micro-PIV measurement with the high-pass filtering technique can provide detailed information about the flow field in the thin liquid layer between the rotating and stationary disks.

In chapter 6, a stereoscopic micro-PTV technique was shown using a single camera with a stereo optical attachment. The attachment developed here was shown to have a higher capability of fine optical adjustment than the previous one proposed by the authors. This stereoscopic micro-PTV technique was validated through a three-dimensional measurement of a rotating flow in a thin liquid layer between a rotating disk and a stationary disk. This rotating liquid layer is 10mm in diameter and the gap between the disks is 500μm. The rotational speed examined is 500rpm. It is shown that the effective depth-of-field of the present technique is 300μm for the imaging optics using a 5× objective (NA=0.14). The measured velocities compare reasonably well with the previous results obtained with a conventional 2D-2C PIV technique.

In chapter 7, in these rotating systems, the problem of friction torque by shear stress, power loss, and of heat transfer is strongly related to inside flowing induced by the rotating disk such as the circulation and secondary flows. These induced flows depend on the geometries of the stationary and rotating disks, for example, gap between stationary and rotating disk as well as radius and angle of rotation disk and so on. The approximate analytical equation was inferred as the function of z/H, r/R, and ω. We have also found, as an important design criterion for rotation-shearing micro reactors, that the decrease of the gap between stationary and rotating disks, i.e., H, can decrease the magnitude of the secondary flow with respect to the magnitude of the tangential velocity. This feature may be used to suppress unwanted effect of the secondary flow (in other words, the reversal flow) that would otherwise cause duplicate reaction in the gap.

Chapter 9 Appendix

9.1 Mfile of frequency sampling method

```
%=========================================================================
%    Digital Image Filtering for Micro-PIV
%
%                                                    2011.2.8
%                                              Written by H.J LEE
%=========================================================================
clc;
close all;
imgRaw = imread('53.bmp','bmp');

% Normalize Image
imgPIV = double(imgRaw) ./ 255;

%-------------------------------------------------------------------------------------------------------------
% Part 1 - 2D FFT
%-------------------------------------------------------------------------------------------------------------

        mxPIV = size(imgPIV);
        %intRows = mxPIV(1);
        %intCols = mxPIV(2);
        [intRows,intCols]= size(imgPIV);

        imgPIVSpectrum = fftshift(FFT2(imgPIV));

%-------------------------------------------------------------------------------------------------------------
% a)       log magnitude and phase
%-------------------------------------------------------------------------------------------------------------

        imgPIVLogMag = log10(1+abs(imgPIVSpectrum));
        imgPIVPhase    = angle(imgPIVSpectrum);
```

```
%-------------------------------------------------------------------------------------------------------------
% b)       Inverse FFT
%-------------------------------------------------------------------------------------------------------------

        imgPIVInverseFFT = abs(IFFT2(imgPIVSpectrum));

%-------------------------------------------------------------------------------------------------------------
% c)       Plots
%-------------------------------------------------------------------------------------------------------------

        figure('Name', 'Part 1', 'NumberTitle', 'off', 'MenuBar', 'none');
        colormap('gray');
        subplot(2,2,1);
        imagesc(imgPIV);
        title('Original Image');
        subplot(2,2,2);
        imagesc(imgPIVLogMag);
        title('Log Maganitude of FFT');
        subplot(2,2,3);
        imagesc(imgPIVPhase);
        title('Phase of FFT');
        subplot(2,2,4);
        imagesc(imgPIVInverseFFT);
        title('Inverse FFT');

%=============================================================================
%    2D FIR Filter Design using FSM
%=============================================================================
          [f1,f2] = freqspace(1024,'meshgrid');
                r = sqrt(f1.^2 + f2.^2);
          Hd = ones(size(f1));
%-------------------------------------------------------------------------------------------------------------
         Bandpass = Hd;
         Highpass = Hd;
```

```
            Lowpass    = Hd;
%-------------------------------------------------------------------------------------------------------------

            Bandpass((r<0.3) | (r>0.8)) = 0;
            Lowpass(r > 0.8) = 0;
            Highpass(r < 0.2) = 0;

%-------------------------------------------------------------------------------------------------------------
%       Fsamp2 Filter Design    (fsamp2 means 2D FIR filter using frequency sampling)
%-------------------------------------------------------------------------------------------------------------

            BandpassFilter = fsamp2(Bandpass);
            LowpassFilter = fsamp2(Lowpass);
            HighpassFilter = fsamp2(Highpass);

            BandpassFilterSpectrum = fftshift(fft2(BandpassFilter, intRows, intCols));
            LowpassFilterSpectrum    = fftshift(fft2(LowpassFilter,    intRows, intCols));
            HighpassFilterSpectrum = fftshift(fft2(HighpassFilter, intRows, intCols));
            imagesc(abs(HighpassFilterSpectrum));

%-------------------------------------------------------------------------------------------------------------

          figure('Name', 'Highpass filter spectrum (Fsamp2)', 'NumberTitle', 'off', 'MenuBar',
                'none');
                colormap(gray);
                subplot(1,2,1);
                imagesc(log10(1+abs(HighpassFilterSpectrum)));
                title('Log Magnitude');
                subplot(1,2,2);
                imagesc(angle(HighpassFilterSpectrum));
                title('Phase');
```

```
%=========================================================================
%       Application of filters to image.
%=========================================================================
%       (c) HiPass Filter image.
%-------------------------------------------------------------------------------------------------------

                imgPIVHIFilteredSpectrum = imgPIVSpectrum .* HighpassFilterSpectrum;

                figure('Name', 'Highpass Filtered Image (Fsamp2)', 'NumberTitle', 'off',
                        'MenuBar', 'none');
                colormap(gray);
                subplot(2,2,1);
                imagesc(log10(1+abs(imgPIVHIFilteredSpectrum)));
                title('Log Magnitude');
                subplot(2,2,2);
                imagesc(angle(imgPIVHIFilteredSpectrum));
                title('Phase');
                subplot(2,2,3);
                imgPIVHIFiltered = abs(ifft2(imgPIVHIFilteredSpectrum));
                imgPIVHIFiltered = circshift(imgPIVHIFiltered,
                [-1.*floor(length(HighpassFilter)/2) -1.*floor(length(HighpassFilter)/2)]);
                imagesc(imgPIVHIFiltered);
                title('Inverse FFT');
%=========================================================================
%       Intensity transformation %---> Gamma correction
%=========================================================================
%       (a) Band Pass Filter image.
%-------------------------------------------------------------------------------------------------------
%               GamimgPIVBPFiltered = imadjust(imgPIVBPFiltered,[0.0;1.0],[0.0;1.0],0.3);
%               figure, imshow(GamimgPIVBPFiltered)
%-------------------------------------------------------------------------------------------------------
%       (b) Low Pass Filter image.
%-------------------------------------------------------------------------------------------------------
%               GamimgPIVLOFiltered = imadjust(imgPIVLOFiltered,[0.0;1.0],[0.0;1.0],0.3);
```

```
%               figure, imshow(GamimgPIVLOFiltered)

%-------------------------------------------------------------------------------------------------------------
%       (c) Hipass Filter image.
%-------------------------------------------------------------------------------------------------------------

%               GamimgPIVHIFiltered = imadjust(imgPIVHIFiltered,[0.0;1.0],[0.0;1.0],0.6);
%               figure, imshow(GamimgPIVHIFiltered)
%
%=============================================================================
%       Intensity transformation ---> Math enhancement of image
%=============================================================================
%       (a) Band Pass Filter image.
%-------------------------------------------------------------------------------------------------------------
%               MathimgPIVBPFiltered = imgPIVBPFiltered*10;
%               figure, imshow(MathimgPIVHIFiltered)
%-------------------------------------------------------------------------------------------------------------
%       (b) Low Pass Filter image.
%-------------------------------------------------------------------------------------------------------------
%               MathimgPIVLOFiltered = imgPIVLOFiltered*10;
%               figure, imshow(MathimgPIVLOFiltered)
%-------------------------------------------------------------------------------------------------------------
%       (c) Hi Pass Filter image.
%-------------------------------------------------------------------------------------------------------------
%               MathimgPIVHIFiltered = GamimgPIVHIFiltered*5;
%               MathimgPIVHIFiltered = imgPIVHIFiltered*5;
%               figure, imshow(MathimgPIVHIFiltered)
% writing image -------------------------------------------------------------------------------------------
%               imwrite(imgPIVBPFiltered,'testBP.bmp');
%               imwrite(imgPIVLOFiltered,'testLO.bmp');
%               imwrite(imgPIVHIFiltered,'D:¥*.bmp');
%               imwrite(MathimgPIVHIFiltered,'D:¥*.bmp');
```

REFERENCES

Adrian R.J (1991) Particle-imaging techniques for experimental fluid mechanics. Annual Review of Fluid Mechanics, 23, 261-304.

Adrian RJ, Yao CS (1985) Pulsed laser technique application to liquid and gaseous flows and the scattering power of seed materials. Applied Optics, 24, 44-52.

Baek SJ, Lee SJ (1996) A new two-frame particle tracking algorithm using match probability. Exp. Fluids, 22, 23–32.

Barker SLR, Ross D, Tarlov MJ, Gaitan M, Locascio LE (2000) Control of flow direction in microfluidic devices with polyelectrolyte multilayers. Anal Chem, 72, 5925–5929.

Beebe DJ, Moore JS, Bauer JM, Yu Q, Liu RH, Devadoss C, and Jo BH (2000) Functional hydrogel structures for autonomous flow control inside microfluidic channels. Nature, 404, 588-590.

Bayt RL, Breuer KS (2000) Fabrication and testing of micro-sized cold-gas thrusters in micropropulsion of small spacecraft. In: Micci M, Ketsdever A (eds), Progress in Astronautics and Aeronautics, vol 187. AIAA, Reston, VA, pp 381–398.

Beebe DJ, Mensing GA, Walker GM (2002) Physics and applications of microfluidics in biology. Ann Rev Biomed Eng, 4, 261–286.

Beskok A and Karniadakis GE, and Trimmer W (1996) Rarefaction and Compressibility. Journal of Fluids Engineering, 118, 448-456.

Biddiss E, Erickson D, Li D (2004) Heterogeneous surface charge enhanced micromixing for electrokinetic flows. Anal Chem, 76, 3208–3213.

Born M and Wolf E (1997) Principles of Optics. Pergamon Press.

Bourdon CJ, Olsen MG, Gorby AD (2004a) Validation of an analytical solution for depth of correlation in microscope particle image velocimetry. Meas Sci Technol, 15, 318–327.

Bourdon CJ, Olsen MG, Gorby AD (2004b) Power-filter technique for modifying depth of correlation in micro-PIV experiments. Exp. Fluids, 37, 263-271.

Bousse L, Cohen C, Nikiforov T, Chow A, Kopf-Sill AR, Dubrow R, Parce W (2000) Electrokinetically controlled microfluidic analysis systems. Ann Rev Biophys Biomol Struct, 29, 155–181.

Bown MR, MacInnes JM, Allen RWK (2005) Micro-PIV measurement and simulation in complex microchannel geometries. Meas. Sci. Technol, 1,619–626.

Bown MR, MacInnes JM, Allen RWK (2006) Three-dimensional, three-component velocity measurements using stereoscopic micro-PIV and PTV. Meas. Sci. Technol ,17:2175–2185.

Bown MR, MacInnes JM, Allen RWK (2007) Three-component micro-PIV using the continuity equation and a comparison of the performance with that of stereoscopic measurements. Exp. Fluids, 42:197–205.

Brody JP, Yager P, Goldstein RE, Austin RH (1996) Biotechnology at low Reynolds numbers. Biophys J, 71, 3430–3441.

Chung J, Grigoropoulos CP, Greif R (2003) Infrared thermal velocimetry for non-intrusive flow measurement in silicon microfluidic devices. Rev Scient Instrum, 74, 2911–2917.

Comtebellot G (1976) Hot-wire anemometry. Ann Rev Fluid Mech, 8, 209–231.

Cowen EA and Monismith SG (1997) A hybrid digital particle tracking velocimetry technique, Exp. Fluids, 22, 199-211.

Cummings EB (2000) An image processing and optimal nonlinear filtering technique for particle image velocimetry of microflows. Exp. Fluids Suppl, S42–S50.

Dahm WJA, Su LK, Southerland KB (1992) A scalar imaging velocimetry technique for fully resolved four-dimensional vector velocity field measurements in turbulent flows. Phys Fluids, 4, 2191–2206.

Danuser D, Kübler O (1995) Calibration procedure for light-optical and scanning electron stereo microscopy in micro- and nonorobotics. In: SPIE proceedings, 2412, three-dimensional microscopy: image acquisition and processing, 174–185.

Darabi J, Ohadi MM, DeVoe D (2001) An electrohydrodynamic polarization micropump for electronic cooling. J Microelectromech Syst, 10, 98–106.

Devasenathipathy S, Santiago JG, Wereley ST, Meinhart CD, and Takehara K (2002) Particle Tracking Techniques for Microfabricated Fluidic Systems. Exp. Fluids, 34, 504-514.

Devasenathipathy S, Santiago JG, Takehara K (2002) Particle tracking techniques for electrokinetic microchannel flows. Anal Chem, 74, 3704–3713.

Devansenathipathy S, Santiago JG, Wereley ST, Meinhart CD, Takehara K (2003) Particle imaging techniques for microfabricated fluidic systems. Exp. Fluids, 34, 504–514.

Edel JB, Hill EK, de Mello AJ (2001) Velocity measurement of particulate flow in microfluidic channels using single point confocal fluroescence detection. Analyst, 126, 1953–1957.

Erkan N, Shinohar K, Okamoto K et al (2008) Measurement of two overlapped velocity vector fields in microfluidic devices using time-resolved PIV. Journal of Visualization 11(1), 33-34.

Gendrich CP, Koochesfahani MM, Nocera DG (1997) Molecular tagging velocimetry and other novel applications of a new phosphorescent supramolecule. Exp. Fluids, 23, 361–372

Giardino J, Hertzberg J and Bradley E (2008) A calibration procedure for millimeter-scale stereomicroscopic particle image velocimetry. Exp. Fluids, 45, 1037-1045.

Gravesen P, Branebjerg J, Jensen OS (1993) Microfluidics—a review. J Microme ch Microeng, 3,168–182.

Guezennec YG, Brodkey RS, Trigui N, Kent JC (1994) Algorithms For Fully Automated 3-Dimensional Particle Tracking Velocimetry. Exp. Fluids, 17, 209-219.

Gui L, Wereley ST (2002) A correlation-based continuous windowshift technique to reduce the peak-locking effect in digial PIV image evaluation. Exp. Fluids, 32, 506–517.

Gui L, Wereley S.T, Lee S.Y (2002) Digital filters for reducing background noise in micro PIV measurement. Proceedings of the 11th international symposium on the application of laser techniques to fluid mechanics, Lisbon.

Gui L, Merzkirch W, Shu JZ (1997), Evaluation of low image density PIV recordings with the MQD method and application to the flow in a liquid bridge. J. Flow Vis. and Image Proc., 4, 4, 333-343.

Guilbault GG (1990) Practical fluorescence, 2nd edn. Marcel Dekker, New Orleans, LA.

Hagsäter S.M, Jensen T.G et al (2007) Acoustic resonances in microfluidic chips: full-image micro-PIV experiment and numerical simulation. Lap Chip, 7, 1336-1344.

Hecht E (2001) Optics, 4th edn. Addison-Wesley, New York.

Ho CM, Tai YC (1996) Review: MEMS and its applications for flow control. J. Fluids Eng, 188, 437–447.

Ho CM, Tai YC (1998) Micro-electro-mechanical-systems (MEMS) and fluid flows. Ann Rev Fluid Mech, 30, 579–612.

Hohreiter V, Wereley ST, Chung JN, Olsen MG (2001) "Cross-correlation analysis for temperature measurement," 4th International Symposium on Particle Image Velocimetry, Paper 1145,Göttingen, Germany, Sept. 2001.

Hove J, Köster R, Forouhar A, Acevedo-Bolton G, Fraser S, Gharib M (2003) Intracardiac fluid forces are an essential epigenetic factor for embryonic cardiogenesis. Nature, 421,172–177.

Huang X, Gordon MJ, Zare RN (1988) Current-monitoring method for measuring the electroosmotic flow rate in capillary zone electrophoresis. Anal Chem, 60, 1837–1938.

Inoué S and Spring KR (1997) Video Microscopy, Second Edition, Plenum Press.

Ismagilov RF, Stroock AD, Kenis PJA, Whitesides G (2000) Experimental and theoretical scaling laws for transverse diffusive broadening in two-phase laminar flows in microchannels. Appl Phys Lett, 76, 2376–2378.

Jacobson SC, Culbertson CT, Daler JE, Ramsey JM (1998) Microchip structures for submillisecond electrophoresis. Anal Chem, 70, 3476–3480.

Kataoka K, Miyazaki H, Bunya M, Okano T and Sakurai Y (1998) Totally Synthetic Polymer Gels Responding to External Glucose Concentration: Their Preparation and Application to On-Of Regulation of Insulin Release. J. Am. Chem. Soc., 120: 12694-5.

Keane RD and Adrian RJ (1992) Theory of cross-correlation analysis of PIV images. Applied Scientific Research, 49, 1-27.

Keane RD, Adrian RJ, Zhang Y (1995) Super-Resolution Particle Imaging Velocimetry. Measurement Science Technology, 6, 754-768.

Keane RD, Adrian RJ, Zhang Y (1995) Super resolution particle image velocimetry. Meas. Sci. Technol, 6,754–768.

Kim MJ, Beskok A, Kihm KD (2002) Electro-osmosis-driven micro-channel flows: a comparative study of microscopic particle image velocimetry measurements and numerical simulations. Exp. Fluids, 32, 170–180.

Kim S. and Lee S.J. (2007) Measurement of 3D laminar flow inside a micro tube using micro digital holographic particle tracking velocimetry, Journal of Micromechanics and Microengineering, 17, 2157-2162.

Kirby BJ, Hasselbrink Jr, EF (2004a) Zeta potential of microfluidic substrates: 1. Theory, experimental techniques, and effects on separations. Electrophoresis, 25, 187–202.

Kirby BJ, Hasselbrink Jr, EF (2004b) Zeta potential of microfluidic substrates: 2. Data for polymers. Electrophoresis, 25, 203–213.

Klank H, Goranovic G, Kutter JP, Gjelstrup H, Michelsen J, Westergaard CH (2002) PIV measurements in a microfluidic 3D-sheathing structure with three-dimensional flow behaviour. J Micromech Microeng, 12, 862–869.

Knight JB, Vishwanath A, Brody JP, Austin RH (1998) Hydrodynamic focusing on a silicon chip: mixing nanoliters in microseconds. Phys Rev Lett, 80, 3863–3866.

Koochesfanhani MM, Gendrich CP, Nocera DG (1993) A new technique for studying

the Lagrangian evolution of mixing interfaces in water flows. Bull Am Phys Soc, 38, 2287.

Koutsiaris AG, Mathioslakis DS and Tsangaris S (1999) Microscope PIV for velocity-field measurement of particle suspensions flowing inside class capillaries, Meas. Sci. Technol, 10, 1037-1046.

Lee H.J., Mitorida S. and Nishino K. (2009) Development of stereo micro PTV and its application to a rotating disk flow. 8th international symposium on particle image velocimetry, Melbourne, Victoria, Australia.

Lee JY, Ji HS, Lee SJ (2007) Micro-PIV measurements of blood flow in extraembryonic blood vessels of chicken embryos. Physiol Meas 28:1149–1162.

Lee SJ. and Kim S. (2009) Advanced particle-based velocimetry techniques for microscale flows, Microfluid Nanofluid, 6, 577-588.

Lee SJ, Kim GB (2003) X-ray particle image velocimetry for measuring quantitative flow information inside opaque objects. J. Appl. Phys, 94, 3620–3623.

Lee WY, Wong M, Zohar Y (2002) Microchannels in series connected via a contraction/expansion section. J. Fluid Mech, 459, 187–206.

Lempert WR, Jiang N, Sethuram S, Samimy M (2002) Molecular tagging velocimetry measurements in supersonic microjets. AIAA J, 40, 1065–1070.

Lempert WR, Magee K, Ronney P, Gee KR, Haugland RP (1995) Flow tagging velocimetry in incompressible flow using photoactivated nonintrusive tracking of molecular motion (PHANTOMM). Exp. Fluids, 18, 249–257.

Lim J.S (1990) Two-dimensional signal and image processing. Prentice hall, New Jersey.

Lindken R, Westerweel J and Wieneke B (2005) Development of a self-calibrating stereo-l-PIV system and its application to the three-dimensional flow in a T-shaped mixer. In: Proceedings of the 6th international symposium on PIV (Pasadena, USA) S06-5P045.

Lindken R, Rossi M et al (2009) Micro-particle image velocimetry-recent developments, applications, and guidelines. Lab chip, 9, 2551-2567.

Lindken R, Westerweel J, Wieneke B (2006) Stereoscopic micro particle image velocimetry. Exp Fluids 41:161–171.

Liu R, Yu Q, Bauer JM, Jo BH, Moore JS and Beebe DJ (2000) In-channel processing to create autonomous hydrogel microvalves. In: Micro Total Analysis Systems 2000, (ed. A. van denBerg et al.) pp. 45-48, Netherlands: Kluwer Academic.

Locke BR, Acton M, Gibbs SJ (2001) Electro-osmotic flow in porous media using magnetic resonance imaging. Langmuir, 17, 6771–6781.

Maynes D, Webb AR (2002) Velocity profile characterization in sub-millimeter diameter tubes using molecular tagging velocimetry. Exp Fluids, 32, 3–15.

McKnight TE, Culbertson CT, Jacobson SC, Ramsey JM (2001) Electroosmotically induced hydraulic pumping with integrated electrodes on microfluidic devices. Anal Chem, 73, 4045–4049.

Meinhart CD and Zhang HS (2000) The flow structure inside a microfabricated inkjet printhead. Journal of MEMS. 9(1) IEEE March 2000, pp. 67-75.

Meinhart CD, Wereley ST and Santiago JG (1999b) PIV Measurements of a Microchannel Flow. Exp. in Fluids, 27, 414-419.

Meinhart CD, Wereley ST, Santiago JG (2000), A PIV algorithm for estimating time-

averaged velocity fields, Journal of Fluids Engineering, 122, 285-289.

Meinhart CD, Wereley ST (2003) The theory of diffraction-limited resolution in microparticle image velocimetry. Meas. Sci. Technol, 14, 1047–1053.

Meinhart CD, Zhang H (2000) The flow structure inside a microfabricated inkjet printhead. J Microelectromech Syst, 9, 67–75.

Meinhart CD, Wereley ST, Gray MHB (2000a) Volume illumination for two-dimensional particle image velocimetry. Meas. Sci. Technol, 11, 809–814.

Meinhart CD, Wereley ST, Santiago JG (1998) Micron-resolution velocimetry techniques. In: Adrian RJ et al. (eds), Developments in laser technologies and applications to fluid mechanics. Springer, Berlin Heidelberg New York.

Meinhart CD, Wereley ST, Santiago JG (1999) PIV measurements of a microchannel flow. Exp. Fluids, 27, 414–419.

Meinhart CD, Wereley ST, Santiago JG (2000b) A PIV algorithm for estimating time-averaged velocity fields. J Fluids Eng, 122, 285–289.

Meinhart CD, Wang D, Turner K (2003) Measurement of AC electrokinetic flows. Biomed Microdevices, 5, 139–145.

Melin J. et al. (2004) A fast passive and planar liquid sample micromixer. Lab Chip, 4, 214-219.

Meng H, Pan G, Pu Y, Woodward SH (2004) Holographic particle image velocimetry: from film to digital recording. Meas. Sci. Tech 15:673–685.

Mosier BP, Molho JI, Santiago JG (2002) Photobleached-fluorescence imaging of microflows. Exp. Fluids, 33, 545–554.

Nguyen NT, Wereley ST (2002) Fundamentals and applications of microfluidics. Artech House, Norwood, MA.

Nishino K., Kasagi N. and Hirata M. (1989) Three-dimensional particle tracking velocimetry based on automated digital image processing. Journal of Fluids Engineering, 111, 384-391.

Olsen MG, Bauer JM, and Beebe DJ (2000) Particle imaging technique for measuring the deformation rate of hydrogel microstructures. Applied Physics Letters, 76, 3310-3312.

Olsen MG and Adrian RJ (2000a) Out-of-focus effects on particle image visibility and correlation in microscopic particle image velocimetry, Exp. Fluids, 29, S166-S174.

Olsen MG and Adrian RJ (2000b) Brownian motion and correlation in particle image velocimetry, Opt. Laser Technol., 32, 621-627.

Olsen MG, Bourdon CJ (2003) Out-of-plane motion effects in microscopic particle image velocimetry. J. Fluids Eng, 125, 895–901.

Ovryn B (2000) Three-dimensional forward scattering particle image velocimetry applied to a microscope field-of-view. Exp Fluids, S175–S184.

Park JS, Choi CK, Kihm KD (2004) Optically sliced micro-PIV using confocal laser scanning microscopy (CLSM). Exp. Fluids, 37, 105–119

Park J.S. and Kihm K.D. (2006) Three-dimensional micro-PTV using deconvolution microscopy. Exp. Fluids, 40, 491-499.

Pereira F, Gharib M (2002) Defocusing digital particle image velocimetry and the three-dimensional characterization of two phase flows. Meas. Sci. Technol, 13,683–694

Pernod P, Preobrazhensky V, Merlen A et al (2010) MEMS magneto-mechanical microvalves (MMMS) for aerodynamic active flow control. Journal of Magnetism and Magnetic Materials, 322,1642-1646.

Pittman JL, Gessner HJ, Frederick KA, Raby EM, Batts JB, Gilman SD (2003a) Experimental studies of electroosmotic flow dynamics during sample stacking for capillary electrophoresis. Anal Chem, 75, 3531–3538.

Pittman JL, Henry CS, Gilman SD (2003b) Experimental studies of electroosmotic flow dynamics in microfabricated devices during current monitoring experiments. Anal Chem, 75, 361–370.

Pittman JL, Schrum KF, Gilman SD (2001) On-line monitoring of electroosmotic flow for capillary electrophoretic separations. Analyst, 126, 1240–1247.

Prasad AK, Adrian RJ, Landreth CC, Offutt PW (1992) Effect of resolution on the speed and accuracy of particle image velocimetry interrogation. Exp. Fluids, 13, 105-116.

Raffel M, Willert C, Wereley S, Kompenhans J et al (2007) Particle image velocimetry: a practical guide (experimental fluid mechanics), 2nd edn. Springer, Auflage.

Revenco I and Proksch R (2000) Magnetic and acoustic tapping mode microscopy of liquid phase phospholipid bilayers and DNA molecules. J. App. Phys., 87: 526-533.

Reyes DR, Iossifidis D, Auroux P-A, Manz A (2002) Micro total analysis systems. 1. Introduction, theory, and technology. Anal Chem, 74, 2623–2636.

Ross D, Locascio LE (2002) Microfluidic temperature gradient focusing. Anal Chem, 74, 2556–2564.

Ross D, Locascio LE (2003) Effect of charged fluorescent dye on the electroosmotic mobility in microchannels. Anal Chem, 75, 1218–1220.

Ross D, Gaitan M, Locascio LE (2001a) Temperature measurement in microfluidic systems using a temperature-dependent fluorescent dye. Anal Chem, 73, 4119–4123.

Russ JC (1999) The image processing handbook, 3rd edn. CRC Press, Boca Raton, FL.

Saito, K. (inventor) (2001) Method and device for mixing liquid or solution. Japanese Patent Application No. 2001-299398, Publication No. 2003-103152 (published August 4, 2003).

Santiago JG (2001) Electroosmotic Flows in Microchannels with Finite Inertial and Pressure Forces, Anal. Chem. 73, pp. 2353-2365.

Santiago JG, Wereley ST, Meinhart CD, Beebe DJ and Adrian RJ (1998) A particle image velocimetry system for microfluidics. Exp. Fluids, 25,4,316-319.

Sato Y, Inaba S, Hishida K, Maeda M (2003a) Spatially averaged time-resolved particle-tracking velocimetry in microspace considering Brownian motion of submicron fluorescent particles. Exp. Fluids, 35, 167–177.

Sato Y, Irisawa G, Ishizuka M, Hishida K, Maeda M (2003b) Visualization of convective mixing in microchannel by fluorescence imaging. Meas. Sci. Technol, 14, 114–121.

Schnars U, Jüptner W (1994) Direct recording of holograms by a CCD target and numerical reconstruction. Appl Opt 33:179–181.

Stitou A and Riethmuller ML (2001) Extension of PIV to super resolution using PTV. Meas. Sci. Technol, 12, 1398-1403.

Schrum KF, Lancaster JM, III, Johnston SE, Gilman SD (2000) Monitoring electroosmotic flow by periodic photobleaching of a dilute, neutral fluorophore. Anal Chem, 72, 4317–4321.

Shchukin V.K (1980) Heat transfer and hydrodynamics of pipe flows in mass-force fields. 2nd revised and enlarged edition.

Sheen H.J, Hsu C.J, Wu T.H et al (2008) Unsteady flow behaviors in an obstacle-type valveless micropump by micro-PIV. Microfluidics and Nanofluidics, 4(4), 331-342.

Shevchuk I.V (2009) Convective heat and mass transfer in rotating disk systems.

Sheng J, Malkiel E, Katz J (2006) Digital holographic microscope for measuring three-dimensional particle distributions and motions. Appl Opt, 45, 3895–3901.

Sheng J, Malkiel E, Katz J (2008) Using digital holographic microscopy for simultaneous measurements of 3D near wall velocity and wall shear stress in a turbulent boundary layer. Exp. Fluids, 45, 1023–1035.

Shinohara K, Sugii Y, Aota A, Hibara A, Tokeshi M, Kitamori T, Okamoto K (2004) High-speed micro-PIV measurements of transient flow in microfluidic devices. Meas .Sci. Technol, 15,1965–1970

Sinton D, Erickson D, Li D (2002a) Photo-injection based sample design and electroosmotic transport in microchannels. J Micromech Microeng, 12, 898–904.

Sinton D, Erickson D, Li D (2003a) Micro-bubble lensing induced photobleaching (l-BLIP) with application to microflow visualization. Exp. Fluids, 35, 178–187.

Sinton D, Ren L, Xuan X, Li D (2003e) Effects of liquid conductivity differences on multi-component sample injection, pumping and stacking in microfluidic chips. Lab on a Chip, 3, 173–179.

Stier B, Koochesfahani MM (1999) Molecular tagging velocimetry (MTV) measurements in gas phase flows. Exp. Fluids, 26, 297–304

Stone HA, Kim S (2001) Microfluidics: basic issues, applications and challenges. AIChE J, 47, 1250–1254.

Stone SW, Meinhart CD, Wereley ST (2002) A microfluidic-based nanoscope. Exp Fluids, 33, 613–619.

Stone HA, Stroock AD, Ajdari A (2004) Engineering flows in small devices: microfluidics toward a lab-on-a-chip. Ann Rev Fluid Mech, 36, pp.381–411.

Stroock AD, Weck M, Chiu D, Huck WTS, Kenis PJA, Ismagilov RF, Whitesides GM (2000b) Erratum: patterning electro-osmotic flow with patterned surface charge. Phys Rev Lett, 84, 6050.

Sugii Y, Nishio S, Okamoto K (2002) In vivo PIV measurement of red blood cell velocity field in microvessels considering mesentery motion. Physiol Meas, 23, 403–416.

Takehara K, Adrian RJ, Etoh GT, Christensen KT (2000) A Kalman tracker for super-resolution PIV. Exp. Fluids ,29, S34-S41.

Tallarek U, Rapp E, Seidel-Morgenstern A, Van As H (2002) Electroosmotic flow phenomena in packed capillaries: from the interstitial velocities to intraparticle and boundary layer mass transfer. J Phys Chem B, 106, 12709–12721.

Tallarek U, Scheenen TWJ, de Jager PA, Van As H (2001) Using NMR displacement imaging to characterize electroosmotic flow in porous media. Magn Reson Imaging, 19, 453–456.

Taylor JA, Yeung ES (1993) Imaging of hydrodynamic and electrokinetic flow profiles in capillaries. Analyt Chem, 65, 2928–2932.

Tieu AK, Mackenzie MR, Li EB (1995) Measurements in microscopic flow with a

solid-state LDA. Exp. Fluids, 19, 293–294.

Tokumaru PT, Dimotakis PE (1995) Image correlation velocimetry. Exp. Fluids, 19, 1–15.

Tseng F-G, Yang I-D, Lin K-H, Ma K-T, Lu M-C, Tseng Y-T, Chieng C-C (2002) Fluid filling into micro-fabricated reservoirs. Sensors Actuators A, 97–98, 131–138.

Wereley ST, Gui LC, and Meinhart CD (2001) "Flow Measurement Techniques for the Microfrontier," Paper 2001-0243, American Institute of Aeronautics and Astronautics Annual Meeting, Reno, NV, Jan. 2001.

Wereley ST, Gui L, Meinhart CD (2002) Advanced algorithms for microscale particle image velocimetry. AIAA J 40:1047–1055.

Wereley ST and Meinhart CD (2001), Adaptive second-order accurate particle image velocimetry, Exp. Fluids, 31, 258-268.

Wereley ST, Santiago JG, Meinhart CD, and Adrian RJ 1998, Velocimetry for MEMS Applications. Proc. of ASME/DSC, Vol. 66, (Micro-fluidics Symposium, Nov. 1998, Anaheim, CA).

Wereley ST, Gui L, Meinhart CD (2002) Advanced algorithms for microscale particle image velocimetry. AIAA J, 40, 1047–1055.

Westin KJA, Choi CH, Breuer KS (2003) A novel system for measuring liquid flow rates with nanoliter per minute resolution. Exp. Fluids, 34, 635–642

Wong PK, Lee YK, Ho CM (2003) Deformation of DNA molecules by hydrodynamic focusing. J Fluid Mech, 497, 55–65.

Yoon JH, Lee SJ (2002) Direct comparison of 2D and 3D stereoscopic PIV

measurement. Meas Sci Tech, 13, 1631–1642.

Yoon SY, Kim KC (2006) 3D particle position and 3D velocity field measurement in a microvolume via the defocusing concept. Meas. Sci. Technol, 17, 2897–2905.

Yu CH, Yoon JH and Kim HB (2009) Development and validation of stereoscopic micro-PTV using match probability. Meas. Sci. Technol, 23, 845-855.

Yurechko VN, Ryazantsev YS (1991) Fluid motion investigation by the photochromic flow visualization technique. Exp. Thermal. Fluid. Sci, 4, 273–288.

Zettner CM, Yoda M (2003) Particle velocity field measurements in a near-wall flow using evanescent wave illumination. Exp. Fluids, 34, 115–121.